EVOLUTION OF FRICTIONAL BEHAVIOR OF PUNCHBOWL FAULT GOUGES SHEARED AT SEISMIC SLIP RATES AND MECHANICAL AND HYDRAULIC PROPERTIES OF NANKAI TROUGH ACCRETIONARY PRISM SEDIMENTS DEFORMED ALONG DIFFERENT LOADING PATHS

A Dissertation

by

HIROKO KITAJIMA

Submitted to the Office of Graduate Studies of
Texas A&M University
in partial fulfillment of the requirements for the degree of

DOCTOR OF PHILOSOPHY

December 2010

Major Subject: Geology

EVOLUTION OF FRICTIONAL BEHAVIOR OF PUNCHBOWL FAULT GOUGES SHEARED AT SEISMIC SLIP RATES AND MECHANICAL AND HYDRAULIC PROPERTIES OF NANKAI TROUGH ACCRETIONARY PRISM SEDIMENTS DEFORMED ALONG DIFFERENT LOADING PATHS

A Dissertation

by

HIROKO KITAJIMA

Submitted to the Office of Graduate Studies of
Texas A&M University
in partial fulfillment of the requirements for the degree of

DOCTOR OF PHILOSOPHY

Approved by:

Co-Chairs of Committee,	Frederick M. Chester
	Judith S. Chester
Committee Members,	Andreas Kronenberg
	Richard Carlson
	Giovanna Biscontin
Head of Department,	Andreas Kronenberg

December 2010

Major Subject: Geology

ABSTRACT

Evolution of Frictional Behavior of Punchbowl Fault Gouges Sheared at Seismic Slip Rates and Mechanical and Hydraulic Properties of Nankai Trough Accretionary Prism Sediments Deformed at Different Loading Paths. (December 2010)

Hiroko Kitajima, B. S., Kyoto University

Co-Chairs of Advisory Committee: Dr. Frederick M. Chester
Dr. Judith S. Chester

Frictional measurements were made on natural fault gouge at seismic slip rates using a high-speed rotary-shear apparatus to study effects of slip velocity, acceleration, displacement, normal stress, and water content. Thermal-, mechanical-, and fluid-flow-coupled FEM models and microstructure observations were implemented to analyze experimental results. Slightly sheared starting material (Unit 1) and a strongly sheared and foliated gouge (Unit 2) are produced when frictional heating is insignificant and the coefficient of sliding friction is 0.4 to 0.6. A random fabric gouge with rounded prophyroclasts (Unit 3) and an extremely-fine, microfoliated layer (Unit 4) develop when significant frictional heating occurs at greater velocity and normal stress, and the coefficient of sliding friction drops to approximately 0.2. The frictional behavior at coseismic slip can be explained by thermal pressurization and a temperature-dependent constitutive relation, in which the friction coefficient is proportional to 1/T and increases with temperature (temperature-strengthening) at low temperature conditions and

decreases with temperature (temperature-weakening) at higher temperature conditions. The friction coefficient, normal stress, pore pressure, and temperature within the gouge layer vary with position (radius) and time, and they depend largely on the frictional heating rate. The critical displacement for dynamic weakening is approximately 10 m or less, and can be understood as the displacement required to form a localized slip zone and achieve a steady-state temperature condition.

The temporal and spatial evolution of hydromechanical properties of recovered from the Nankai Trough (IODP NanTroSEIZE Stage 1 Expeditions) have been investigated along different stress paths, which simulate the natural conditions of loading during sedimentation, underthrusting, underplating, overthrusting, and exhumation in subduction systems. Porosity evolution is relatively independent of stress path, and the sediment porosity decreases as the yield surface expands. In contrast, permeability evolution depends on the stress path and the consolidation state, e.g., permeability reduction by shear-enhanced compaction occurs at a greater rate under triaxial-compression relative to uniaxial-strain and isotropic loading. In addition, experimental yielding of sediment is well described by Cam-Clay model of soil mechanics, which is useful to better estimate the in-situ stress, consolidation state, and strength of sediment in nature.

ACKNOWLEDGEMENTS

I would like to thank my committee co-chairs, Dr. Frederick M. Chester, and Dr. Judith S. Chester for their guidance over the past six years. I also thank my committee members, Dr. Andreas Kronenberg, Dr. Richard Carlson, and Dr. Giovanna Biscontin, for their suggestions and feedback throughout the course of this research.

I would like to thank Clayton Powell for his assistance in the laboratory. Thanks also go to my friends and colleagues and the department faculty and staff for making my time at Texas A&M University a great experience. I particularly appreciate Masako Tominaga for not only discussing science but also chatting private things almost everyday.

I also want to extend my gratitude to Dr. Toshihiko Shimamoto, who recommended me to study at Texas A&M, and allowed me to conduct the friction experiments using his high-speed rotary-shear apparatus at Kyoto University.

This research was funded by the National Science Foundation (grant EAR‐0510892), the Southern California Earthquake Center (based on NSF Cooperative Agreement EAR‐0529922 and USGS Cooperative Agreement 07HQAG0008), Schlanger Ocean Drilling Fellowship, which is part of the NSF-sponsored U.S. Science Support Program for IODP (USSSP-IODP) that is administered by Joint Oceanographic Institutions (now Consortium for Ocean Leadership). I also thank College of Geosciences and Conocophillips for providing financial support.

Finally, thanks to my mother, father, and brother for their encouragement and patience.

TABLE OF CONTENTS

Page

LIST OF FIGURES

Page

Page

LIST OF TABLES

1. INTRODUCTION

Devastating earthquakes regularly occur at plate boundaries. Despite considerable research, the mechanics of faulting and the physics of earthquake instability are still not well understood. Both brittle and ductile deformation associated with large earthquakes, slow slip events, and creep occur at different conditions of pressure, temperature, and strain rate, and are controlled by interactions of mechanical and chemical processes of crack growth, frictional slip, lithification, metamorphism, fluid-flow, dissolution, cementation, solute transport, and heat transfer. It is crucial to understand the mechanical, hydraulic, and frictional properties of fine-grained, granular geomaterials at conditions of pressure, temperature, and strain rate that are appropriate to each deformation and recovery processes. Here I study on (1) the frictional behavior of fault rocks at seismic slip rates to understand dynamic weakening during earthquake slip, and (2) the evolution of hydromechanical properties of sediments at different stress states and stress histories in order to understand seismogenesis in subduction zones.

In Sections 2 and 3, I study the frictional behaviors of fault rocks at seismic slip rates. I report high-speed rotary-shear gouge friction experiments on Punchbowl fault gouge at different conditions of slip velocity, acceleration, displacement, normal stress, and water contents. In the rotary-shear configuration, slip rates and displacement vary with radius. In addition, considerable heat generation can cause variation in temperature and normal stress, and thus in coefficient of friction. In Section 2, we make an assumption

---

This dissertation follows the style of *Journal of Geophysical Research.*

that normal stress is heterogeneous but coefficient of friction is homogeneous in samples. We employ thermal-mechanical coupled finite element (FEM) models to analyze mechanical data of high-speed rotary-shear experiments. We also study microstructures of radial-cut sections of friction experiments to understand the microprocesses during co-seismic slip. In Section 3, we develop temperature-dependent constitutive relations of friction from the experimental results presented in Section 2. We run coupled thermal, mechanical, and fluid-flow models to test the constitutive relations. The models can treat heterogeneous evolution of normal stress, temperature, coefficient of friction, and pore fluid pressure in the sample.

In Section 4, we study the evolution of hydromechanical properties of sediments at different stress states. We report triaxial deformation experiments along different stress paths on the sub-seafloor sediment samples from the Nankai Trough accretionary subduction zone. Different stress paths simulate the natural conditions of loading during sedimentation, underthrusting, underplating, overthrusting, and exhumation. Combining the experimental results and logging data, we constrain the in-situ stress states and strength.

2. HIGH-SPEED FRICTION OF FAULT ULTRACATACLASITE IN ROTARY SHEAR: CHARACTERIZATION OF FRICTIONAL HEATING, MECHANICAL BEHAVIOR, AND MICROSTRUCTURE EVOLUTION*

2.1. Introduction

Although great progress has been made in understanding the dynamics of earthquakes, an adequate understanding of the microscopic processes of faulting that influence the nucleation, propagation and arrest of earthquake rupture remains elusive [e.g., *Rice and Cocco*, 2006; *Mizoguchi et al.*, 2009]. For earthquake faulting, dramatic weakening at coseismic slip rates is responsible for some characteristics of rupture propagation and energy radiation, as well as for the apparent low strength of plate-boundary faults [*Kanamori and Heaton*, 2000; *Noda et al.*, 2009]. Several dynamic weakening mechanisms have been proposed, including flash heating [*Rice*, 1999; 2006], thermal pressurization of pore fluid [*Sibson*, 1973; *Lachenbruch*, 1980; *Mase and Smith*, 1987], shear melting [*Spray*, 1993; *Tsutsumi and Shimamoto*, 1997; *Hirose and Shimamoto*, 2005; *Di Toro et al.*, 2006], silica gel formation [*Goldsby and Tullis*, 2002; *Di Toro et al.*, 2004], normal interface vibration [*Brune et al.*, 1993], elastohydrodynamic lubrication [*Brodsky and Kanamori*, 2001], and decomposition weakening [*Han et al.*, 2007]. Determining which of these mechanisms are important in

*Reprinted with permission from "High-speed friction of fault ultracataclasite in rotary shear: Characterization of frictional heating, mechanical behavior, and microstructure evolution" by Hiroko Kitajima, Judith S. Chester, Frederick M. Chester, and Toshihiko Shimamoto, 2010. *Journal of Geophysical Research*, *115*, B08408, doi:10.1029/2009JB007038, Copyright 2010 by the American Geophysical Union.

natural faulting and developing constitutive relations to describe the relevant physics are important tasks in earthquake mechanics.

Experimental studies of rock friction at low slip velocity, i.e. using conventional laboratory displacement rates of 1 μm/s to 1 mm/s, have made great strides in establishing rate and state constitutive relations for friction [e.g., *Marone*, 1998] that have been successfully used in modeling nucleation and growth of earthquake ruptures [*Dieterich*, 1992; *Lapusta and Rice*, 2003]. More recently, rock friction experiments at intermediate (1-100 mm/s) and high (> 0.1 m/s) slip velocities have begun to elucidate the behavior at rates appropriate to coseismic slip where dynamic weakening mechanisms can be important [e.g., *Tsutsumi and Shimamoto*, 1997; *Di Toro et al.*, 2004]. Experiments at the intermediate and high slip rates often employ rotary shear configurations so as to allow large total displacements. In most high slip-velocity tests, the samples are not sealed and a confining pressure is not applied; thus the normal stress across the slipping zone is moderate (5-40 MPa) or low (<5 MPa). These high speed experiments generally have focused on two types of systems, sliding between bare rock surfaces along which frictional melting is favored [e.g., *Tsutsumi and Shimamoto*, 1997], or shear within thin layers of simulated or natural gouge [e.g., *Mizoguchi et al.*, 2009]. A common finding from high-speed experiments is that friction is reduced to extremely low values (coefficient of friction $\mu \approx 0.2$) in gouge at coseismic slip rates even when frictional melting and melt lubrication are not operative. In most cases, weakening is attributed to activation of one of several possible thermal weakening processes associated with frictional heating.

Recently several high-speed, rotary shear experiments have been conducted on natural and simulated, clay-bearing, quartzo-feldspathic gouge at low normal stress levels [*Brantut et al.*, 2008; *Mizoguchi et al.*, 2007, 2009; *Boutareaud et al.*, 2008]. All these works report dynamic weakening associated with frictional heating, and infer weakening mechanisms associated with dehydration reactions [*Brantut et al.*, 2008], vaporization of water [*Boutareaud et al.*, 2008, 2010], silica gel lubrication, flash heating, or moisture-draining [*Mizoguchi et al.*, 2009]. The experiments use solid cylindrical blocks of rock to shear the thin layers of gouge, and employ Teflon sleeves pressed around the blocks to retain the gouge at high-speeds. This configuration produces a variation in slip rate along the gouge layer, from zero at the rotational axis to maximum values at the periphery of the gouge layer. Thermal modeling of the experiments show that the temperature in the gouge layer is spatially variable and a function of time (or cumulative slip). To date, however, determination of frictional strength from the measured data has assumed homogeneous stress and a uniform coefficient of friction in the gouge layer. In addition, microscale studies have not attempted to characterize the spatial heterogeneity or temporal evolution of structure. These observations are important to the analysis of mechanical properties.

The purpose of this paper is to present a suite of high speed rotary shear experiments on thin layers of clay-bearing, quartzo-feldspathic gouge, that utilize sequential displacement tests over a range of slip velocity and normal stress conditions. Microstructural observations and finite element method (FEM) modeling are used to define the spatial variation in conditions and deformation response within the samples as

a function of cumulative displacement, and provide a basis to constrain the mechanical behavior and elucidate the processes responsible for dynamic weakening. The present work is on experiments that are similar to those in recent studies reported in *Mizoguchi et al.* [2009], *Brantut et al*. [2008], and *Boutareaud et al.* [2008].

2.2. Methods

2.2.1. Experimental procedure

The clay-bearing, quartzo-feldspathic material used in the experiments is derived from the dark yellowish-brown ultracataclasite taken from surface exposures of the Punchbowl fault (location DP4), a large displacement exhumed fault of the San Andreas system, in the Devil's Punchbowl Los Angeles County Park, California [*Chester and Logan*, 1987]. The ultracataclasite primarily consists of sub-micron size particles of quartz (47%) and feldspar (19%) produced by comminution, and a smaller amount of syn- and post-faulting alteration products including smectite (22%), clinoptillolite (7%), and chlorite (5%), with trace amounts of calcite and analcime [*Chester and Logan*, 1986; *Chester and Chester*, 1998; *Chester et al.*, 2005].

The ultracataclasite was disaggregated to a particle size less than 106 μm in diameter using a mortar and pestle. One gram of the disaggregated sample was placed between two cylindrical host blocks (25 mm diameter) of gabbro or granite to form a gouge layer approximately 1 mm thick (Figure 2.1a). "Water-dampened" gouge layers were wetted with 0.3 g of distilled water prior to sliding and "room-dry" gouge layers were equilibrated at room humidity conditions without added water. The end surfaces of the

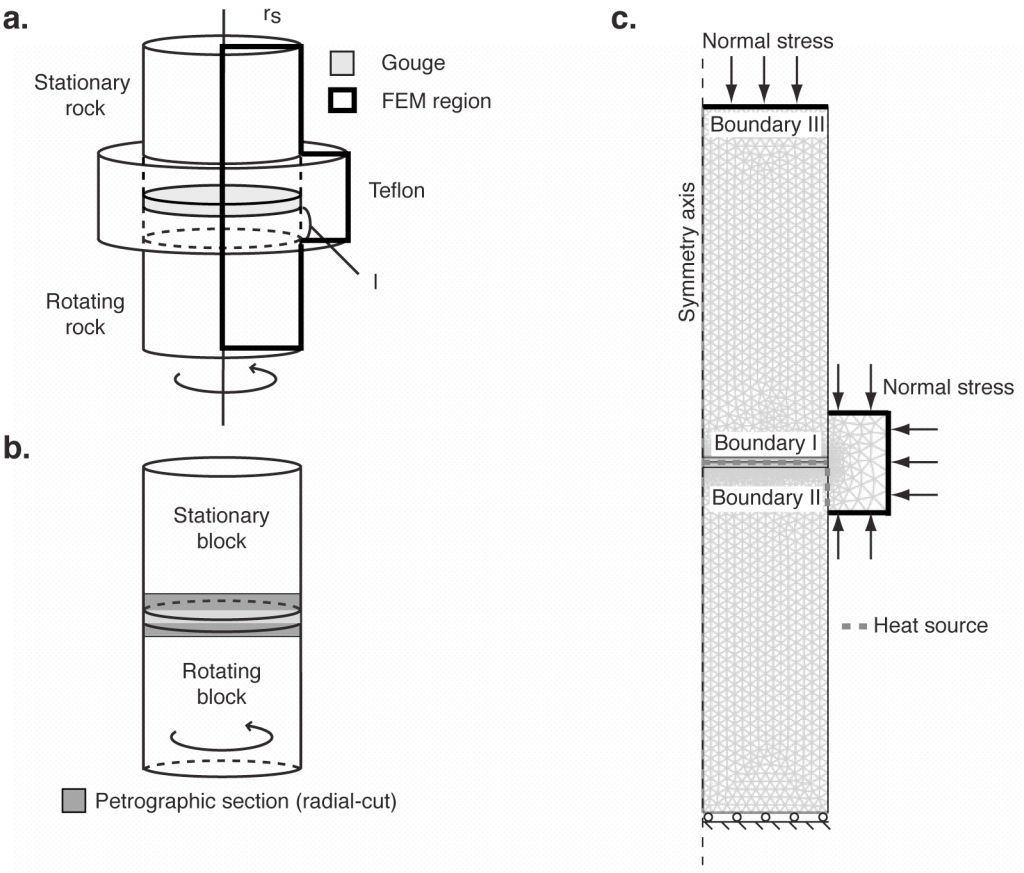

Figure 2.1. Diagrams of sample assembly, radial-cut section, and FEM model. (a) Diagram of sample assembly showing sample radius, r_s = 12.5 mm, length of Teflon sleeve in contact with rotating block, l = 5 mm, and portion of the assembly modeled using FEM (outlined in thick black line). (b) Location of the petrographic section cut through the rotation axis and perpendicular to the gouge layer, i.e., a radial cut. (c) Mesh and boundary conditions for the FEM model. Dashed gray lines show the locations of frictional heat sources and black lines show the boundaries subjected to a normal stress. Axial displacement is constrained to zero at the end of the rotating block.

cylindrical host blocks in contact with the gouge were ground with coarse (#80) SiC to roughen the surfaces and promote slip inside the gouge layer rather than along the gouge-host-block interface. A Teflon sleeve was pressed around each sample to cover the gouge layer and prevent the loss of gouge during assembly and subsequent shearing (Figure 2.1a).

Experiments were conducted in the high-speed rotary-shear apparatus described by *Shimamoto and Tsutsumi* [1994], *Hirose and Shimamoto* [2005], and *Mizoguchi et al.* [2009]. In the apparatus, an air actuator applies the axial load (normal force) at the stationary end of the sample and an electric motor drives rotation at the opposite end. Normal force, torque, axial shortening, and rotation speed were recorded at 20-200 Hz depending on experiment duration.

Samples were sheared at constant rotation rate of 100, 200, 400, 800, or 1500 revolutions per minute (rpm) to a total of 29 to 1600 revolutions and an axial force of 0.1, 0.15, 0.29 and 0.59 kN. Once the axial force is established, rotation of the sample is initiated using a clutch to engage the motor drive train. The target rotation rate is achieved within 1 s. The clutch also is used to disengage the motor at the end of each experiment which allows the rotation rate to be reduced to 0 rpm within a few to tens of seconds depending on the target speed.

2.2.2. Analysis of mechanical data

The measured torque, $\overline{M}$, includes the torque resulting from friction inside the gouge layer, $\overline{M_s}$, and the torque from friction between the Teflon sleeve and the differentially rotating host rock blocks, $\overline{M_t}$

$$\overline{M} = \overline{M}_s + \overline{M}_t . \tag{2.1}$$

From this relation and appropriate approximations, the coefficient of friction of the layer as a function of time (or slip at constant slip velocity) is determined. In cylindrical coordinates, $\overline{M_s}(t)$ may be expressed as

$$\overline{M}_s(t) = \int_0^{2\pi}\int_0^{r_s} \tau_s(r,\theta,t)\cdot r\, dr\, d\theta \cdot r\,, \tag{2.2}$$

where τ_s is the shear stress on the layer as a function of position (r, θ) and time t, and r_s is the sample radius. Relation (2.2) can be simplified to

$$\overline{M}_s(t) = 2\pi \int_0^{r_s} \tau_s(r,t)\cdot r^2 dr\,, \tag{2.3}$$

assuming that the shear stress within the sample is axisymmetric. The coefficient of friction of the gouge layer can be determined from the measured data using relation (2.3) and the definition of the coefficient of sliding friction,

$$\tau_s(r,t) = \sigma_n(r,t)\cdot \mu_s(r,t), \tag{2.4}$$

where σ_n is the normal stress on the gouge layer and μ_s is the coefficient of friction in the gouge layer.

Many analyses of rotary shear experiments reported to date assume that σ_n and μ_s do not vary with position in the gouge layer. Thus, σ_n was determined directly from the

area of the gouge surface and the measurements of the axial force, and μ_s was derived from $\overline{M_s}$ by substituting (2.4) into (2.3), $\mu_s = 3\overline{M_s}(t)/2\pi r_s^3\sigma_n$ [e.g., *Tsutsumi and Shimamoto*, 1997; *Hirose and Shimamoto*, 2005; *Mizoguchi et al.*, 2009]. In addition, by assuming that the shear stress on the layer is uniform, i.e., the normal stress and coefficient of friction are independent of position, the rate of frictional work can be expressed by

$$W' = \int_0^{2\pi}\int_0^{r_s} \tau_s \cdot r dr d\theta \cdot 2\pi\omega r = \frac{4\pi^2\tau_s r_s^3\omega}{3}, \tag{2.5}$$

where ω is the angular velocity. The work rate may be expressed as $\tau_s \cdot \pi r_s^2 \cdot V_{eq}$, by defining an equivalent slip velocity, V_{eq}, where

$$V_{eq} = \frac{4\pi\omega r_s}{3} = 2\pi\omega \cdot \left(\frac{2}{3}r_s\right), \tag{2.6}$$

i.e., the velocity at two thirds of sample radius, r_s. Equivalent displacement is defined as the local displacement at the same position, and is given by, $d_{eq} = v_{eq} \cdot t = \frac{4\pi\omega r_s t}{3} = 2\pi R \cdot \left(\frac{2}{3}r_s\right)$ where R is revolution. The assumption of uniform shear stress is not made in the analysis herein so the concept of an equivalent velocity and displacement is no longer valid; however, we describe the general conditions of the experiments in terms of the velocity, displacement, and temperature at 2/3 r_s, treating these as representative value for each experiment (Table 2.1). For the rotation rates used, the representative slip velocities are 0.1, 0.2, 0.35, 0.7, and 1.3 m/s. Representative displacements range between 1.3 m and 84 m. The axial loads applied in the experiments were chosen to achieve average normal stresses of 0.2, 0.3, 0.6, and 1.3 MPa.

Table 2.1. Summary of the experiment conditions, the mechanical results, and the microstructure observations. σ_n: average normal stress, V_{eq}: representative slip rate, d_{eq}: representative displacement, μ_{peak}: peak friction coefficient, μ_{10m}: friction coefficient at d_{eq} of 10m, T_{eq}: representative temperature, E_{total}: total energy from frictional work, E_{heat}: energy for heat, E_{vapor}: energy for vaporization, and E_{dehy}: energy for dehydration of smectite.

	σ_n (MPa)	V_{eq} (m/s)	Total d_{eq} (m)	μ_{peak}	μ_{10m}	MaxT_{eq} (°C)	E_{total} ($\times10^6$J/m^2)	E_{heat} ($\times10^6$J/m^2)	E_{vapor} ($\times10^6$J/m^2)	E_{dehy} ($\times10^6$J/m^2)	Observed microstructure units
HVR885gb	0.3	0.1	15	0.73	0.68	74	3.2	0.20	-	-	2
HVR515gr	0.6	0.1	1.3	0.53	-	58	0.36	0.12	-	-	1a and 2
HVR513gr	0.6	0.1	2.6	0.76	-	60	0.43	0.13	-	-	-
HVR518gr	0.6	0.1	3.9	0.61	-	88	1.2	0.23	-	-	-
HVR490gr	0.6	0.1	12	0.65	0.39	100	3.2	0.31	-	-	1a and 2
HVR484gr	0.6	0.1	25	0.50	0.48	112	7.0	0.37	-	-	1b and 2
HVR877gb	1.3	0.1	3.2	0.29	-	63	0.90	0.13	-	-	1b and 2
HVR876gb	0.6	0.2	10	0.55	0.27	95	2.3	0.25	-	-	1b, 2, and 4
HVR884gb	0.3	0.35	19	0.69	0.60	146	3.5	0.45	0.49	-	1b, 2, 3, and 4
HVR809gb	0.6	0.35	19	0.60	0.41	192	5.2	0.58	0.64	0.029	2, 3, and 4
HVR821gb	1.3	0.35	12	0.45	0.23	167	4.2	0.48	-	-	2, 3, and 4
HVR898gb	0.3	0.7	18	1.0	0.45	166	3.1	0.46	0.31	0.0040	1b, 2, 3, and 4
HVR899gb	0.6	0.7	1.6	0.88	-	123	0.79	0.26	-	-	1b, and 2
HVR896gb	0.6	0.7	4.4	0.30	-	84	0.58	0.18	-	-	1b, and 2
HVR897gb	0.6	0.7	9.2	0.69	-	142	2.1	0.37	0.13	-	1b, and 2
HVR530gr	0.6	0.7	29	0.96	0.23	222	4.5	0.82	0.91	0.059	1b, 2, 3, and 4
HVR895gb	1.3	0.7	18	0.35	0.10	150	3.3	0.48	-	-	1b, 2, 3, and 4
HVR519gr	0.2	1.3	37	0.71	0.25	271	4.6	0.82	1.3	0.29	1b, 2, 3, and 4
HVR509gr	0.6	1.3	2.5	0.63	-	169	1.2	0.35	0.23	0.0032	1a, 1b, 2, 3, and 4
HVR504gr	0.6	1.3	4.0	0.79	-	159	1.3	0.35	0.16	0.00050	1b, 2, 3, and 4
HVR494gr	0.6	1.3	3.2	0.75	-	174	1.6	0.42	0.34	0.0053	-
HVR486gr	0.6	1.3	15	0.56	0.16	263	3.2	0.69	0.73	0.19	2, 3, and 4
HVR795gb	0.6	1.3	18	0.47	0.12	187	1.7	0.63	0.43	0.026	-
HVR794gb	0.6	1.3	24	0.67	0.13	200	3.1	0.61	0.56	0.028	2, 3, and 4
HVR796gb	0.6	1.3	25	0.85	0.14	246	4.7	0.72	0.79	0.10	1b, 2, 3, and 4
HVR802gb[1]	0.6	1.3	35	1.1	0.21	277	4.6	0.44	-	-	-
HVR482gr	0.6	1.3	83	0.49	0.18	555	13	2.1	1.3	0.45	3 and 4
HVR475gr[1]	0.6	1.3	84	0.86	0.20	584	16	0.88	-	-	-
HVR514gr	1.3	1.3	36	0.60	0.23	430	7.6	1.4	1.2	0.32	-

[1] Room-dry experiments.

The torque supported by the Teflon sleeve, $\overline{M_t}$, is estimated from the Punchbowl gouge experiments and from dedicated experiments on Teflon gouge. For all rotary shear experiments on the Punchbowl gouge layers, the total torque, $\overline{M}$, observed for both initial (peak) and final (steady-state) conditions, shows an increase in magnitude with an increase in axial load, as would be expected for friction in the gouge layer (Figure 2.2a). The dependence of total torque on axial load is attributed entirely to the gouge layer because the sliding interface between the Teflon sleeve and host blocks is not under a direct axial load. Extrapolation of best-fit linear relations to measurements of peak and steady-state torque versus axial load indicates that $\overline{M_t}$ at zero axial load is approximately 1.8 N·m for peak conditions and 0.70 N·m for steady-state conditions (Figure 2.2a).

Teflon gouge experiments are used to better define $\overline{M_t}$ as a function of displacement and rate of rotation. A sample containing a layer of Teflon gouge was sheared at an average normal stress of 0.6 MPa and rotation rates to achieve representative velocities between 0.1m/s and 1.3m/s (Figure 2.2b). When the Teflon gouge was sheared at 1.3m/s, the torque rapidly increased to a maximum value initially, then decreased significantly with subsequent displacement. When the same sample was sheared again at 0.1, 0.35, 0.7, and 1.3m/s, it displayed a low magnitude initial peak friction, little subsequent weakening with slip, and only a small dependence of torque on rotation rate (Figure 2.2b). The strength of samples with Teflon sleeves sheared at zero axial load by N. Brantut (written communication, 2006) displayed a similar change in behavior in the

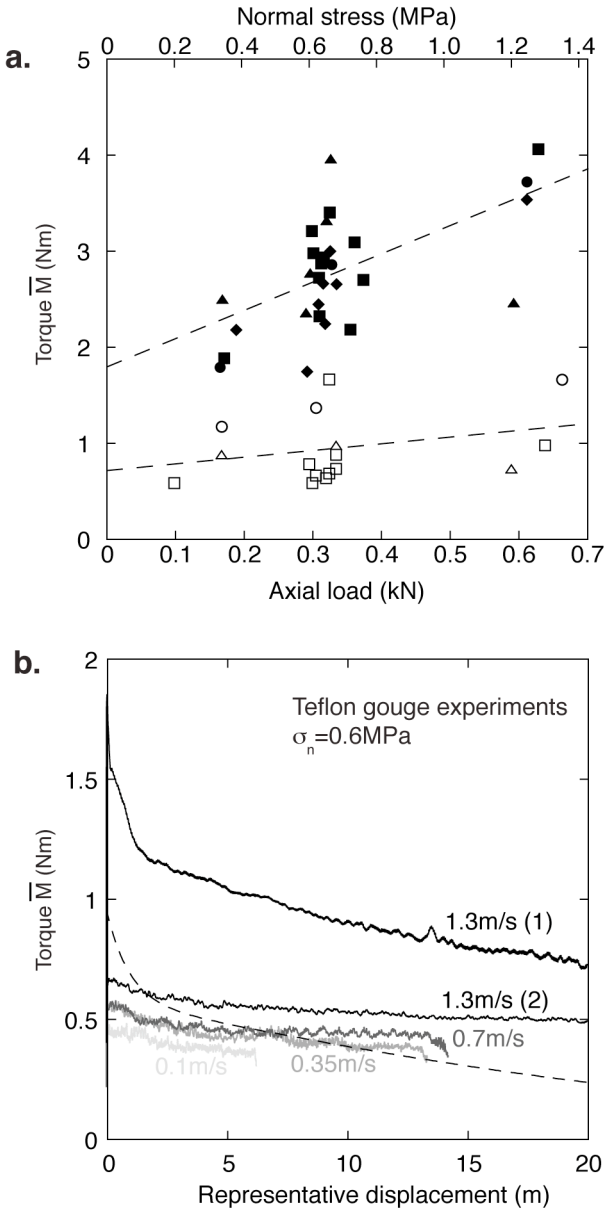

Figure 2.2. Data used to determine the strength of the Teflon sleeve. (a) Total torque as a function of axial load or normal stress for initial peak strength (solid symbols) and steady-state strength (open symbols) of the samples. Symbols indicate the representative slip velocities: 0.1 m/s, diamond; 0.35 m/s, circle; 0.7 m/s, triangle; 1.3 m/s, square. The best-fit lines to peak and steady-state strength can be used to estimate torque at zero axial load, which is assumed to equate with the strength of the Teflon sleeve. (b) Total torque versus representative displacement records for a rotary shear experiment on pure Teflon gouge. Gouge was consecutively sheared at the representative slip velocities of 1.3 m/s (1), 0.1 m/s, 0.35 m/s, 0.7 m/s, and 1.3 m/s (2). The difference between the first test at 1.3 m/s (1) and the second test at 1.3 m/s (2) is used to estimate the strength of the Teflon sleeve as a function of displacement.

first run, decreasing to essentially zero after an initial stage of shear, and also much smaller strength in the second run. The overall strength of Teflon sleeves, and especially the peak strength when initially sheared, is largely dependent on tightness, and the significant strength reduction in the second run is induced by loosening of the Teflon sleeve in contact with the host block during the first run. Accordingly, we assume that the total torque measured in an experiment initially reflects the sum of the torque resulting from the Teflon gouge and that of the Teflon sleeve. When the same samples are sheared again, the total torque only reflects the torque from the Teflon gouge, to a first order approximation. Thus, the difference between the torque at the initiation of shear at 1.3m/s and the torque measured when the same Teflon gouge is sheared again at 1.3m/s gives an estimate of the torque of the Teflon sleeve, and the friction of Teflon gouge ranges from 0.15-0.27. Our successive runs at different slip rates and the transient reduction during each run suggest that the frictional behavior of Teflon should be velocity strengthening and temperature weakening. These results are consistent with a previous study of Teflon friction at similar slip velocity [*McLaren and Tabor*, 1963]. Teflon sleeve torque is adequately expressed as a function of the representative displacement, d_{eq},

$$\overline{M_t} = 0.14 + 0.49\exp(-0.073 \cdot d_{eq}) + 0.33\exp(-1.5 \cdot d_{eq}). \qquad (2.7)$$

The $\overline{M_t}$ described by this relation is consistent with the peak and steady-state torques for the Teflon sleeves estimated from the natural gouge experiments, although the absolute values are slightly lower in magnitude. It should be noted that a new Teflon sleeve was used for each experiment of disaggregated Punchwbowl ultracataclasite and

some variation of initial torque is caused by the uncertain tightness and possibly by gouge intrusion between the Teflon sleeve and the rotating host block during shear (Figure 2.2a). Equation (2.7) is used to calculate $\overline{M_s}$ from $\overline{M}$ for all experiments assuming that $\overline{M_t}$ is independent of velocity and normal stress. The shear stress between the Teflon sleeve in contact with the rotating block, $\tau_t(t)$, can be related to $\overline{M_t}$ by

$$\overline{M}_t(t) = \tau_t(t) \cdot A \cdot r_s = 2\pi\tau_t(t) r_s^2 l, \tag{2.8}$$

where $A = 2\pi r_s l$, and l is the length of the Teflon sleeve in contact with rotating block, i.e. 5 mm (Figure 2.1a).

2.2.3. Microstructure analysis

At the end of an experiment, the sample is epoxied under a vacuum and cut through the axis of the cylinder to produce a thin section that is perpendicular to the slip-direction (i.e., a radial-cut section; Figure 2.1b). Radial thin sections display the structures that develop over the range of slip-rates and slip-magnitudes achieved in an individual experiment, from zero slip and slip-rate at the center of the cylinder to the maximum magnitude of slip and slip-rate at the outer surface of the cylinder. Radial thin-sections allow an investigation of the evolution of microstructures with slip-rate and slip-magnitude within one sample, providing information that is complementary to that acquired by study of multiple samples sheared to different displacements.

Microstructures visible under plane-polarized and cross-polarized light were mapped on photomicrograph mosaics. The distribution and areal extent of distinct microstructural units in each gouge layer were quantified by point-counts along a

traverse with a 70 μm-spacing along the radial direction and a 35 μm-spacing parallel to the specimen axis. The spacing of the point count traverse was chosen to sufficiently characterize the thickness and lateral extent of each structural unit.

2.3. Thermomechanical Model of the Rotary Shear Experiment

2.3.1 Model description

Frictional heating can produce high temperatures in high-speed rotary shear experiments, particularly along the outer annulus of the sample where the velocity of slip is the greatest [e.g., *Mizoguchi et al.*, 2009]. The heterogeneous temperature distribution in the cylindrical host blocks that results from the variation in slip velocity can produce a differential thermal expansion that may result in a significant variation in normal stress on the gouge layer. The heterogeneous normal stress condition can then contribute to radial variation in the rate of frictional heating within the gouge layer. It follows that the coefficient of friction also varies in the radial direction, reflecting the differences in slip-velocity, slip-magnitude, temperature, and normal stress. Thus, the typical assumptions of uniform normal stress and uniform coefficient of friction in the gouge layer are poor approximations.

In order to better define the temperature and normal stress conditions in the sheared gouge layers, we have developed a coupled thermal-mechanical FEM model of the experiments using COMSOL Multiphysics software. The model is designed to treat the coupled, time-dependent frictional heating of the gouge layer, heat conduction in the sample, and the thermal-elastic response of the sample that affects loading of the gouge

layer and thus the rate of frictional heating. The model takes advantage of the axial symmetry of the sample under rotary shear (Figures 2.1a and 2.1c) and is constrained by the thermal and elastic properties of the rock and Teflon, and by the axial load, rate of rotation, and torque for each experiment. For the initial modeling, we assume the coefficient of friction is spatially uniform, but let the normal stress vary with radius, and solve for the temperature and normal stress within the sample as a function of time. We use the model to determine the coefficient of friction of the gouge layer as a function of representative displacement (time) for each experiment. The model can treat the more general case where friction coefficient varies with position, but this is left for later work.

It is assumed that all frictional work is converted to heat. Heat is generated within the gouge layer (boundary I) and between the Teflon sleeve and the host block (boundary II). The frictional heating in the gouge is modeled with a planar source located in the center of the layer (boundary I, Figure 2.1c). The frictional sliding between the Teflon sleeve and host blocks most often occurs along the interface with the rotating side, but sometimes occurs along the stationary block interface or along both interfaces. The location of slip along the Teflon sleeve is not recorded, so for the model we assume slip occurs entirely along the interface with the rotating block (boundary II, Figure 2.1c) to maximize the asymmetry in temperature across the gouge layer and to provide upper and lower bounds on temperature and stress in the two host blocks. All other boundaries are assumed adiabatic.

The heat generation rate per unit area, q_s, on boundary I can be expressed as

$$q_s(r,t) = \tau_s(r,t)v(r) = \mu_s(t)\sigma_n(r,t)v(r), \tag{2.9}$$

using equation (2.4). From equation (2.8), the heat generation rate on boundary II, q_t is given by

$$q_t(t) = \tau_t(t) v_s = \frac{\overline{M_t}(t)}{2\pi r_s^2 l} \cdot 2\pi r_s \omega = \frac{\overline{M_t}(t)\omega}{r_s l}. \tag{2.10}$$

The rock and Teflon components of the sample assembly are treated as homogeneous and isotropic, and linear elasticity is assumed; the thermal and mechanical properties of the components are summarized in Table 2.2 [Schön, 1996; Turcotte and Schubert, 2001]. The normal stress boundary condition at the end of the stationary host bock (boundary III, Figure 2.1c) is specified by the axial load measured during the experiment and the assumption of homogeneous stress at this boundary. The displacement in the axial direction at the end of the rotating block is zero. The stress distribution in the sample is homogeneous before shear is initiated, but frictional heating and thermal expansion during rotation produce heterogeneous stress within the sample. Assuming that the coefficient of friction of the gouge layer does not vary with position, equations (2.3) and (2.4) may be combined to give

$$\overline{M_s}(t) = 2\pi \mu_s(t) \int_0^{r_s} \sigma_n(r,t) \cdot r^2 \, dr, \tag{2.11}$$

and rearranged to solve for the coefficient of friction of the gouge layer,

$$\mu_s(t) = \frac{\overline{M_s}(t)}{2\pi \int_0^{r_s} \sigma_n(r,t) \cdot r^2 \, dr}, \tag{2.12}$$

because the model determines the normal stress distribution and $\overline{M_s}$ is known. It is worth noting that torque is not treated explicitly in the mechanics of the model, but it is

Table 2.2. Thermal and mechanical properties of each component in the FEM model.

	Gouge layer	Host blocks		Teflon
		Granite	Gabbro	
Young's modulus (GPa)	0.01	60	80	0.05
Poisson's ratio	0	0.25	0.18	0.25
Density (g/cm^3)	2.0	2.6	2.95	2.2
Thermal expansion coefficient (K^{-1})	2.4×10^{-5}	2.4×10^{-5}	1.6×10^{-5}	2.4×10^{-5}
Thermal conductivity (W/m·K)	1.5	2.0	3.0	0.24
Heat capacity (J/g·K)	1.0	0.8	1.0	1.05
Maximum mesh size (mm)	0.1	1.0	1.0	2.0

used to calculate the friction coefficient and heat generation rate. In addition, the sample holders of the experimental apparatus are not included in the model so that the local stresses in the host blocks near the sample holders and heat conduction into the sample holders are not considered. As noted above, thermal and elastic properties of gouge layer, host blocks, and Teflon are taken into account in the model. Because the models are fully elastic, the weak gouge layer is modeled with a small Young's modulus, and with a Poisson's ratio of zero, to prevent local interference with the Teflon sleeve. In addition, the contacts between the Teflon sleeve, the gouge layer, and the host blocks are treated as welded in the model, and shear tractions at these boundaries is minimized by applying a normal stress to the Teflon sleeve equivalent to the axial normal stress on the host blocks.

In addition to the temperature and stress distribution in the samples, the model determines the axial displacement of boundary III resulting from thermal expansion of the host blocks and of the gouge layer. The displacement from thermal expansion can be subtracted from the measured axial displacement to determine the change in thickness of the gouge layer from consolidation, dilation, gouge loss or rearrangement, or other processes.

2.3.2 Model validation

The success of the finite element model is illustrated by analyzing a high-speed rotary shear experiment reported by *Mizoguchi et al.* [2009] on the Nojima fault gouge that was sheared at an average normal stress of 0.6 MPa and a representative velocity of

1.0 m/s. The sample assembly and procedure are similar to the experiments described in this paper except that four thermocouples were placed inside the stationary host block to record the temperature during shear (Figure 2.3a). *Mizoguchi et al.* [2009] presented a numerical model of the time-dependent heat generation and conduction for this experiment that is constrained by the experiment data, rock properties, and the assumption that all frictional work in the gouge layer is converted to heat. Their thermal model reproduces the general increase in temperature measured directly by the thermocouples, but the model result does not reproduce the temperature near the gouge layer or predict a good match for the temperature early in the shearing history when there is a rapid change in temperature.

Using the same experiment data and rock properties reported by *Mizoguchi et al.* [2009], we determined the temperature distribution in the experiment using the thermomechanical model. The model shows that the greatest temperature increase occurs at large radii in the gouge layer and also along the slipping interface between the host block and the Teflon sleeve (Figure 2.3a and 2.3d). The model-determined evolution of temperature for the thermocouple locations compares well with the thermocouple measurements, particularly in the early stages of the experiment (Figure 2.3c). We take these results to indicate that thermal expansion and heterogeneous loading of the gouge need to be taken into account, and that the thermomechanical model provides a better analysis of the experiment conditions when compared to models that treat only thermal processes. In addition, the axial displacement measured by *Mizoguchi et al.* [2009], when corrected using the model-determined thermo-elastic expansion of the sample,

Figure 2.3. Results of the thermomechanical FEM model applied to a high-speed rotary shear experiment by Mizoguchi et al. (2009) in which temperature was measured directly by four thermocouples. (a) Spatial distribution of temperature in the vicinity of the gouge at a representative displacement of 10 m. The black dots (CA1-CA4) show locations of the four thermocouples. Temperature is contoured (white lines) at 20 ºC intervals. (b) Variation in axial stress resulting from thermoelastic expansion at an representative displacement of 10 m. (c) Predicted temperature compared to the measured temperature as a function of representative displacement. Solid lines show the calculated temperature assuming that frictional heating occurs between the Teflon sleeve and the rotating host block (as shown in Figures 1c and 3a) and dashed lines show the calculated temperatures assuming heating occurs between the Teflon sleeve and the stationary host block. (d) Temperature and (e) normalized normal stress at the center of the gouge layer (boundary I) as a function of radius for increasing representative displacements from 0 to 40 m. Normal stress is normalized by the average normal stress, i.e., the total axial force applied to gouge layer divided by the area of the gouge layer. (f) Dilation (axial displacement) versus representative displacement measured directly during the experiment (red line) compared to that from thermal expansion as calculated by model (green line). The displacement of gouge layer (blue line) is determined by subtracting the model-determined thermal dilation from the measured dilation. Note that dilation is positive and shortening is negative. The large contraction and dilation observed after 20 m displacement are likely related to slip readjustment within the layer and loss of gouge past the Teflon sleeve.

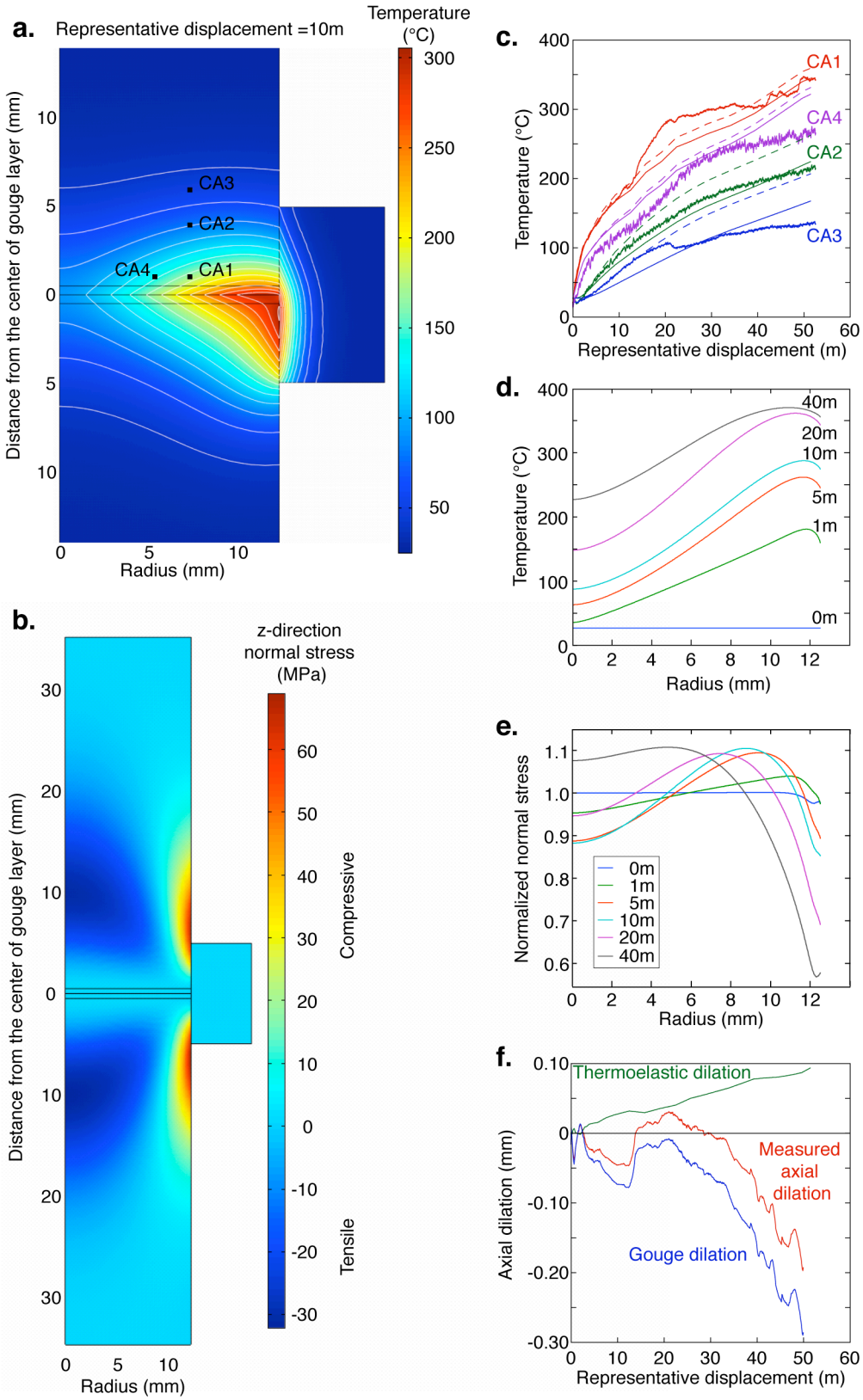
a.
Representative displacement =10m
Temperature (°C)
300
250
200
150
100
50
CA3
CA2
CA4
CA1
Distance from the center of gouge layer (mm)
Radius (mm)
b.
z-direction normal stress (MPa)
Compressive
Tensile
Distance from the center of gouge layer (mm)
Radius (mm)
c.
Temperature (°C)
Representative displacement (m)
CA1
CA4
CA2
CA3
d.
Temperature (°C)
Radius (mm)
40m
20m
10m
5m
1m
0m
e.
Normalized normal stress
Radius (mm)
0m
1m
5m
10m
20m
40m
f.
Axial dilation (mm)
Representative displacement (m)
Thermoelastic dilation
Measured axial dilation
Gouge dilation

indicates that the gouge layer compacts more than implied by the measurement (Figure 2.3f).

Model simulations illustrate that the stress state within the host blocks varies significantly as a result of differential heating and thermal expansion (Figure 2.3b). Axial stress is strongly compressive in the outer portion of the host blocks and tensile in the central region of the cylinder. Furthermore, the range of stress magnitude is greatest in the rotating host block heated by friction at the Teflon sleeve interface. As a result, the normal (axial) stress distribution in the gouge layer evolves with increasing representative displacement in response to the changing temperature conditions in the host blocks (Figure 2.3d and 2.3e). Specifically, the normal stress on the gouge layer is nearly homogeneous at the initiation of slip, but increases in magnitude significantly near the outer surface of the sample after small slip. With increased slip, the maximum normal stress progressively shifts inward towards the cylinder axis while the normal stress is reduced near the periphery.

2.4. Mechanical Results

2.4.1. Analysis of mechanical data by numerical modeling

The numerical model is used to determine the coefficient of friction, temperature, and thickness changes of each gouge layer as a function of representative displacement (Figure 2.4). For example, experiment HVR514gr was sheared at an average normal stress of 1.3 MPa and a representative velocity of 1.3 m/s. The axial load in this experiment varies by about 10% from the target value during shearing, and the total

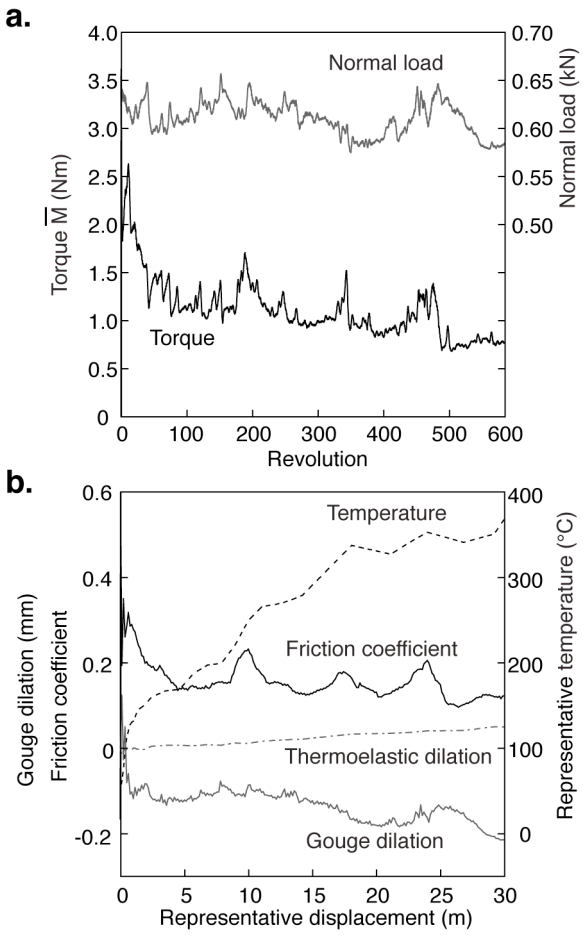

Figure 2.4. Example of high-speed rotary shear data measured during experiments and the conditions in the gouge layer determined from application of the FEM model to that data. (a) The measured torque and normal load as a function of revolution for HVR514gr, which was sheared at a representative velocity of 1.3 m/s and an average normal stress of 1.3 MPa. (b) The model-determined coefficient of friction (solid-black line), representative temperature (dashed-black line), thermoelastic dilation for the entire sample (dashed-gray line), and dilation of gouge layer (solid-gray line).

torque, and thus the coefficient of friction, vary by a factor of about three (Figure 2.4a). The model determined parameters show variations with displacement that are typical for high-speed tests; the temperature increases with displacement, and the friction coefficient and dilation attain peak values just after the initiation of shearing but then decrease with continued displacement (Figure 2.4b).

2.4.2. Mechanical results at different normal stresses and slip velocities

The dependence of friction and temperature on the first 20 m of displacement, over the range of normal stress and slip rates tested, is illustrated by a representative subset of experiments (Figure 2.5; Table 2.1). At the lowest slip rate of 0.1 m/s, the friction coefficient tends to increase to values between 0.4 and 0.6 within the first few m of displacement. No dramatic weakening is observed with larger displacement, and the representative temperature gradually increases to approximately 100 ˚C (Figure 2.5a). At a slip rate of 0.35 m/s, the friction coefficient peaks between 0.4 and 0.7 at several m representative displacement, followed by significant weakening (Figure 2.5b). At this rate, the representative temperature rises above 150 ˚C. At 0.7 and 1.3 m/s slip rates, the maximum friction coefficient of 0.4 to 0.8 is achieved within a couple meters of displacement, and subsequent displacement leads to a dramatic reduction in friction to values as low as 0.4 to 0.1. At these rates, the friction coefficient remains fairly constant (i.e. achieves steady-state) at displacements greater than about 10 m and the representative temperature rapidly increases with displacement, exceeding 200 ˚C.

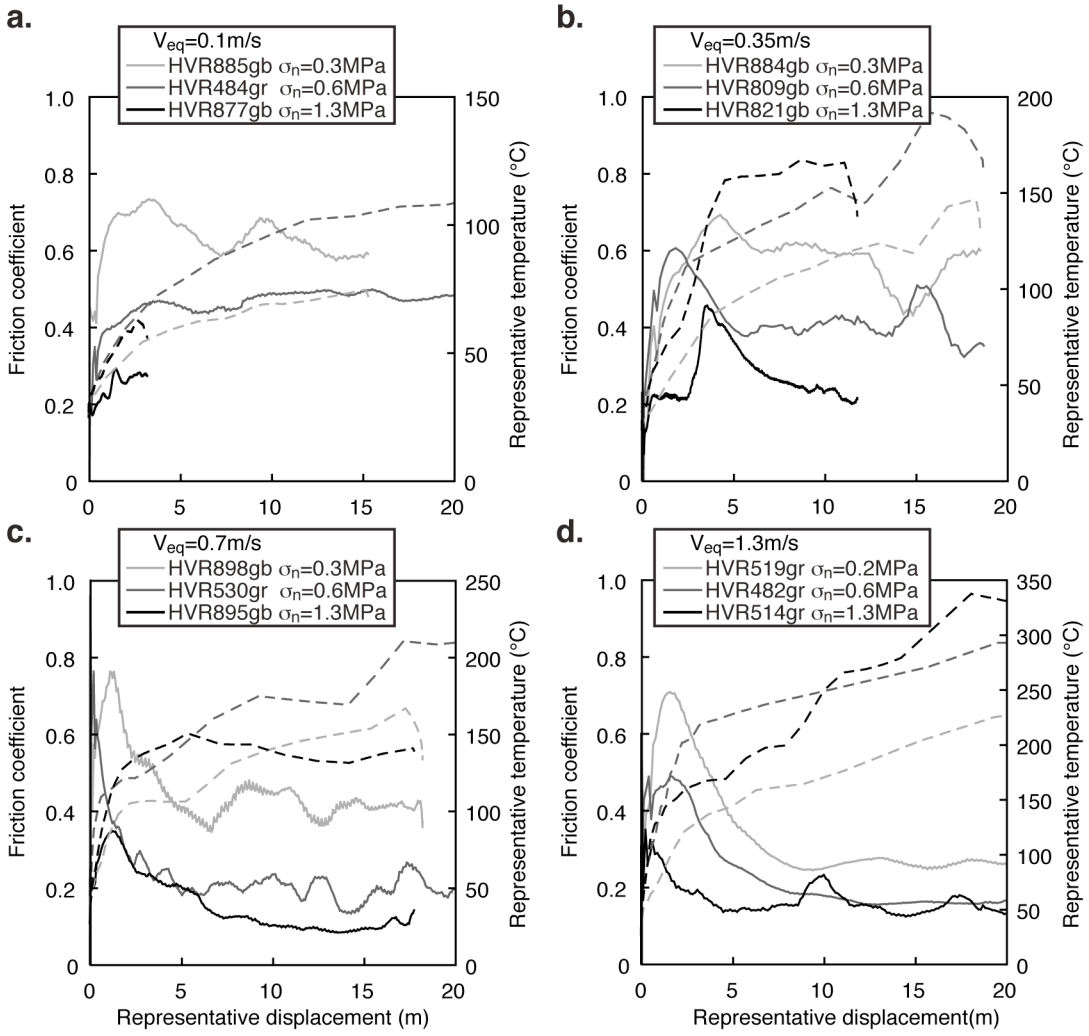

Figure 2.5. Representative results of experiments as determined from the thermomechanical FEM model. Friction coefficient (solid line) and representative temperature (dashed line) as a function of representative displacement for gouge sheared at different normal stresses and slip velocities. The representative slip velocity is (a) 0.1 m/s, (b) 0.35 m/s, (c) 0.7 m/s, and (d) 1.3 m/s. Normal stress is 0.2-0.3 MPa (light-gray), 0.6 MPa (dark-gray), and 1.3 MPa (black), respectively.

For all slip rates, an increase in normal stress produces a decrease in the coefficient of friction (Figure 2.5). In addition, the peak friction coefficient and the magnitude of displacement to achieve approximately steady-state friction decrease with an increase in normal stress. At the same velocity, the representative temperature typically increases with an increase in normal stress; however, the magnitude of the temperature increase also depends on type of rock used for the host blocks. Therefore, the dependencies of friction and temperature on velocity, normal stress and displacement are best illustrated by comparing the series of experiments using gabbro sample assemblies that were sheared at a representative velocity of 0.35 m/s (Figure 2.5b), or comparing a series of experiments that used granite blocks that were sheared at a representative velocity of 1.3 m/s (Figure 2.5d).

2.4.3. Effects of water and host block

The addition of water leads to weakening and dilation as illustrated by the comparison of two room-dry samples sheared at a slip rate of 1.3 m/s and normal stress of 0.6 MPa to similar water-dampened experiments. The coefficient of friction of the room-dry samples is slightly greater than the water-dampened samples at the initial stages of shear (Figure 2.6a). The room-dry samples achieve peak strength at somewhat smaller displacements (Figure 2.6a) and show somewhat less dilation overall (Figure 2.6c). The water-dampened and room-dry samples with granite host blocks achieve greater temperatures in the gouge layers (Figure 2.6b) and greater dilation (Figure 2.6c) than the otherwise similar experiments with gabbro host blocks. These differences reflect

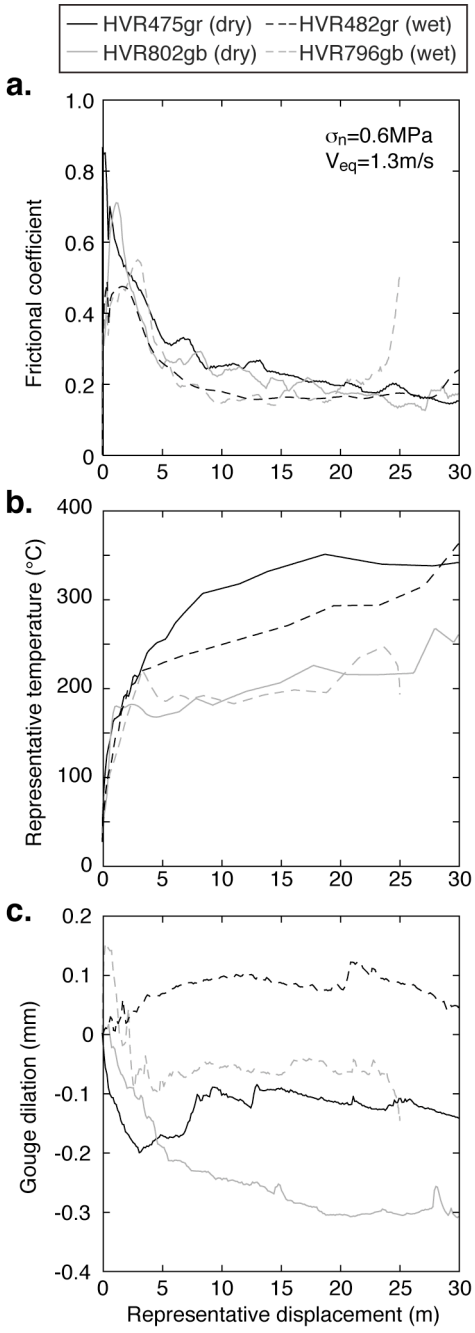

Figure 2.6. The influence of water and type of rock used (granite, gr, or gabbro, gb) in the sample assembly on gouge behavior. Solid lines represent the room-dry samples, and dashed lines represent water-dampened samples. (a) Frictional coefficient, (b) representative temperature, and (c) gouge dilation as a function of representative displacement.

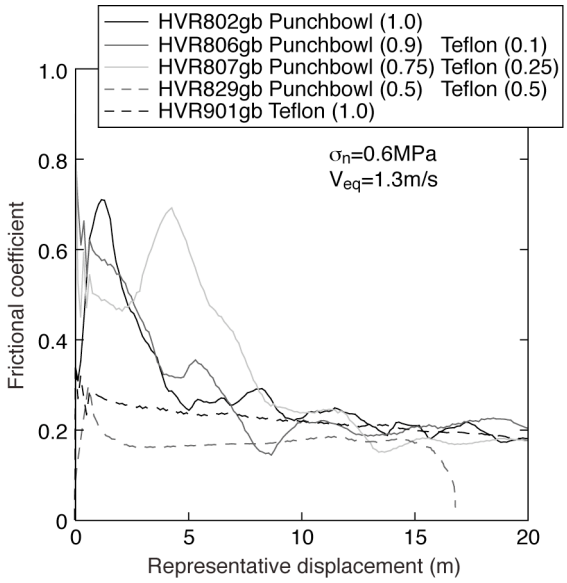

Figure 2.7. Results of rotary shear experiments designed to evaluate the influence of small amounts of Teflon contamination on the mechanical response of the natural gouge. Friction coefficient versus representative displacement for natural gouge mixed with different proportions of Teflon particles. The number in the parentheses indicates the weight in grams of each component.

the lower thermal diffusivity of granite, that leads to greater representative temperatures within and adjacent to the gouge layer when granite is used in the sample assembly.

2.4.4. Effect of Teflon contamination

Early in this study we noted that small flakes of Teflon had been added to the outer portion of the gouge layer. To determine the influence of the Teflon on gouge behavior, Teflon flakes, less than 106 μm in diameter, were mixed with ground ultracataclasite in proportions of 10, 25, 50, and 100% by weight. The mixtures were sheared at a normal stress of 0.6 MPa and a representative slip velocity of 1.3 m/s at room-dry conditions. Gouge mixtures containing less than 50% by weight Teflon behave the same as the pure ultracataclasite gouge (Figure 2.7). Gouge containing more than 50% Teflon by weight displays a reduction of the coefficient of friction and a smaller weakening distance. Microstructure observations indicate that the volume of Teflon present in our early experiments is significantly less than 10%, and therefore we include these data in our analysis.

2.5. Microstructure of Sheared Gouge Layers

2.5.1. Definition of distinct microstructural units in the gouge

Four distinct microstructural units have been identified based on the maximum grain size, grain shape, fabric, clay foliation, and presence of localized slip surfaces (Figure 2.8). Unit 1 is the least deformed and Unit 4 is the most deformed. The geometry and

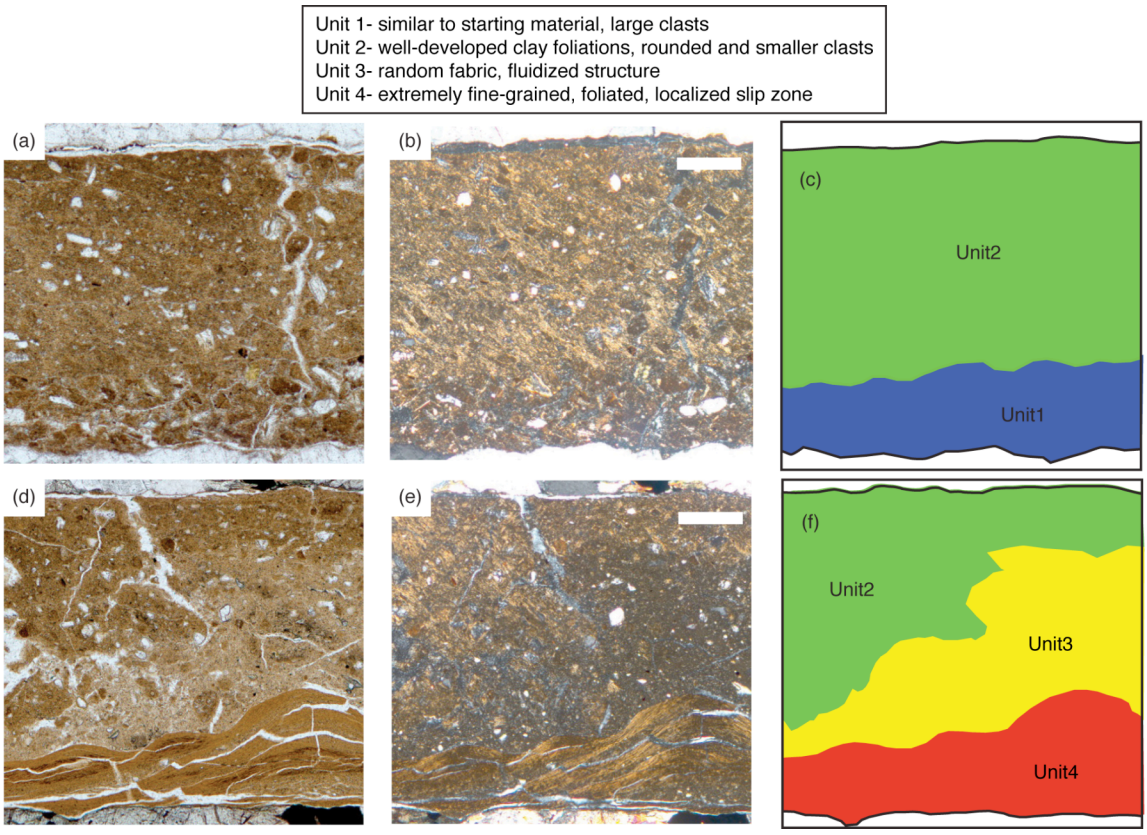

Figure 2.8. Photomicrographs of representative microstructures in the four units of the sheared gouge layer. (a-c) Portion of experiment HVR490gr in (a) plane-polarized light, (b) crossed polarized light, and (c) a schematic map. (d-f) Portion of experiment HVR794gb in (d) plane-polarized light, (e) crossed polarized light, and (f) a schematic map. All images are at the same magnification; white scale bars in (b) and (e) are 200 µm.

Figure 2.9. The four distinct gouge units mapped in radial-cut sections from three experiments sheared to approximately 25 m representative displacement at an average normal stress of 0.6 MPa. R, V, and D denote radius, local velocity, and local displacement within the gouge layer. (a) HVR484gr sheared at 0.1 m/s. (b) HVR530gr sheared at 0.7 m/s. (c) HVR794gb sheared at 1.3 m/s.

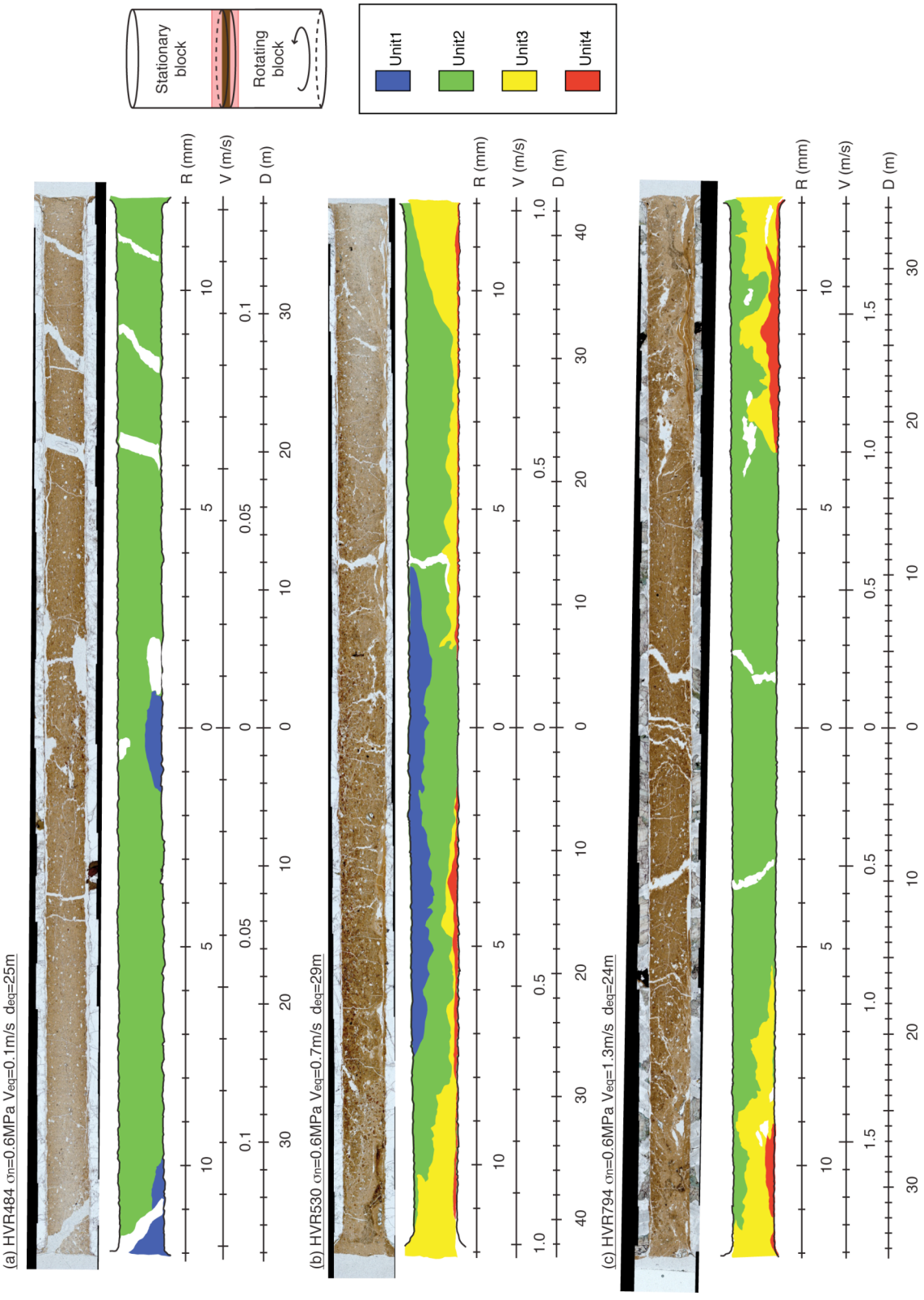
Stationary block
Rotating block
Unit1
Unit2
Unit3
Unit4
(a) HVR484 σn=0.6MPa Veq=0.1m/s deq=25m
(b) HVR530 σn=0.6MPa Veq=0.7m/s deq=29m
(c) HVR794 σn=0.6MPa Veq=1.3m/s deq=24m
R (mm)
V (m/s)
D (m)

distribution of the four units are consistent with the axial symmetry expected for rotary shear (Figure 2.9).

Unit 1 resembles the starting material, is present in lower velocity experiments, and is subdivided into two units. Both subunits tend to occur in the central portion of the gouge layer where the slip velocity and shear displacement are small (Figure 2.8). In a few cases, very small regions of Unit 1 also are present at the outermost edge of the gouge layer (Figure 2.9). Unit 1a primarily is observed in the samples sheared at 0.1 m/s. This unit has a granular texture, reflecting the starting material, being composed of angular clasts of Punchbowl ultracataclsite, as well as clasts of mono- and polycrystalline quartz, calcite, and laumontite. Although Unit 1a is somewhat compacted, it does not display flattened grains, a clay foliation, reduced particle sizes, or particle rounding.

Unit 1b appears in regions sheared at slightly higher slip rates and is similar to Unit 1a except it is more compacted, the clasts are a little more rounded and smaller, and a faint clay-foliation is present. The boundary of Unit 1b with Unit 1a and Unit 2 is gradational and not always distinct. Unit 1a tends to form a fairly sharp boundary with Unit 2, and contacts between Unit 1 and Unit 4 are not observed.

Unit 2 is distinguished by a well-developed clay foliation (Figure 2.8). Overall the foliation displays a preferred orientation that is approximately parallel to the plane of the layer, although locally the foliation may be inclined at low angles to the plane. Thin clay-lined microscale shears are part of this foliation. These often occur in two sets, symmetrically disposed about the plane of the gouge layer. Clasts of the original ultracataclasite are present, but they are more rounded, fewer in number, and smaller in

size, when compared to Unit 1. Unit 2 forms contacts with all other units, but for the most part is located between Unit 1 and either Units 3 or 4.

Units 3 and 4 form at higher velocity and greater displacement conditions, being best developed at large radii. Unit 3 is distinguished by a less compacted texture, light color, and random fabric. It has a very fine-grained matrix and large, dispersed clasts of Units 1 and 2, and in a few cases, ripped-up fragments of Unit 4 (Figure 2.8). In most cases the clasts are well-rounded; a few of these were noted to be very well-rounded clay-coated clasts, similar to the clay-clast aggregates (CCA) described by *Boutareaud et al.* [2008, 2010] and *Boullier et al*. [2009]. When present, typically Unit 3 is located in the outermost region of the circular gouge layer and is thickest at the perimeter, tapering inward (Figure 2.9); it is not present in the central portion of the gouge layer where the slip velocity and displacement are minimal. In most cases, Unit 3 is located between Units 2 and 4. The contact between Units 2 and 3 is irregular and displays narrow regions of localized mixing and interpenetration. Unit 3 correlates to the "non-foliated gouge" unit of *Boutareaud et al.* [2008].

Unit 4 is rusty orange to dark brown under plane-polarized light (Figure 2.8), forming thin layers along the boundary with the host blocks, defining regions of highly localized slip (Figure 2.9). This unit is composed of extremely fine particles, and displays a strong clay foliation and a distinct banded character. The foliation and banding are parallel to the layer except where Unit 4 is locally disrupted and thickened by offset on oblique imbricating shears or by folding. In most cases, Units 3 and 4 occur together where the slip velocity and displacement are large. The contact between Units 3 and 4 displays

irregular and straight segments. Unit 4 correlates to the "main slipping zone" of *Brantut et al*. [2008], the "foliated gouge" unit of *Boutareaud et al.* [2008], and the "deformation zone" of *Mizoguchi et al.* [2009].

2.5.2. Microstructural evolution as a function of shearing conditions

The relative thicknesses of the different microstructural units derived from the point-count data are shown graphically as a function of slip-velocity and shear-displacement (Figure 2.10). Comparing plots for all experiments illustrates that Unit 1 constitutes a significant fraction of the total gouge layer thickness only at the lowest velocity and smallest displacement conditions. In contrast, Unit 2 is present in significant proportions over a wide range of velocities and displacement magnitudes. Unit 3 is a significant fraction of the gouge layer thickness only for the very highest velocity and displacement conditions achieved. Volumetrically, Unit 4 is much less significant as it rarely constitutes more than a few percent of the total gouge layer thickness.

Histograms displaying the point count data characterize the thickness of each microstructural unit as a function of the radial position to demonstrate the kinematics of deformation in the gouge at the different experimental conditions (Figure 2.11). Histogram plots for experiments at representative velocities between 0.1 to 1.3 m/s were selected to show the stages of structural development with shearing for representative displacements between 1.3 and 29 m. At the lowest representative velocity tested, 0.1 m/s, Units 1 and 2 are the only units present; Units 3 and 4 are not produced at these conditions even after a representative displacement of 25 m (Figure 2.11a). With increasing

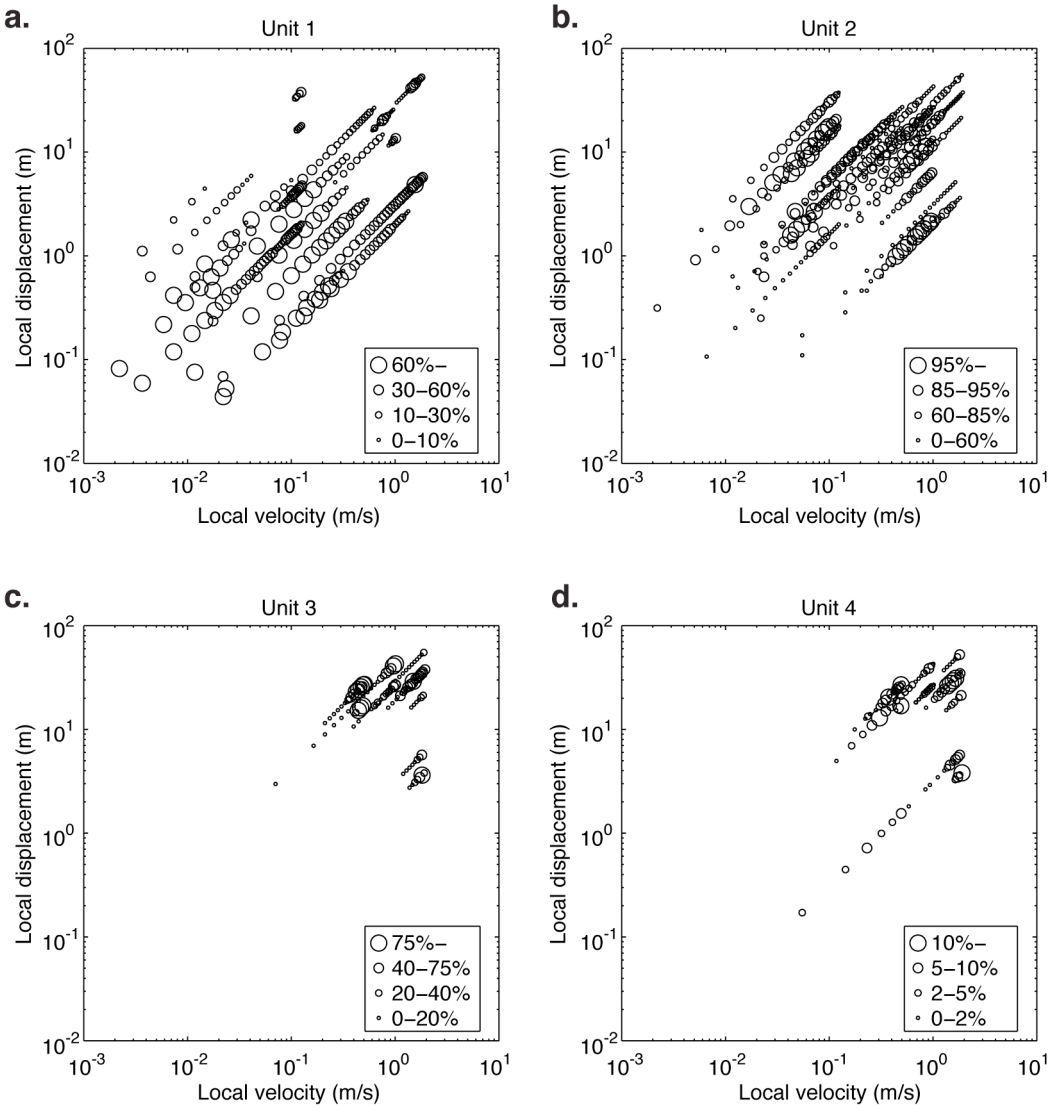

Figure 2.10. Relative volume fraction of each gouge unit from all experiments as a function of local slip velocity and local displacement over the range of possible radii. (a) Unit 1; (b) Unit 2; (c) Unit 3; (d) Unit 4. Note that the scale of symbol size to volume fraction varies between plots.

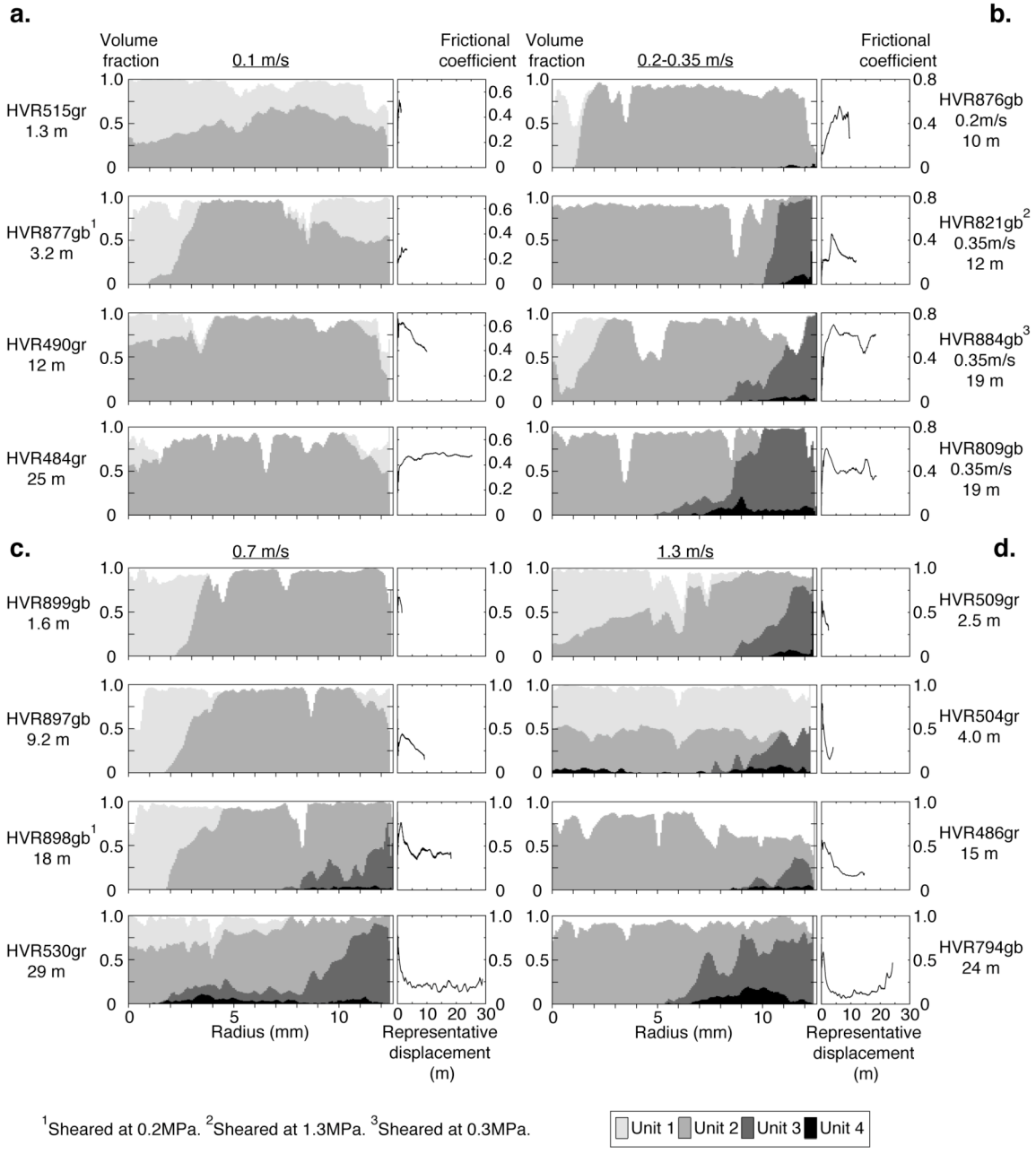

Figure 2.11. Histograms showing stages of development of gouge units for representative displacements up to approximately 25 m. Plots show the average volume fraction of each unit as a function of radius as determined by point-counting. The experiment number and the total representative displacement are indicated beside each plot, and the coefficient of friction versus representative displacement is shown to the right of each histogram. All experiments were sheared at 0.6 MPa normal stress unless noted otherwise. Test series conducted at slip velocities of (a) 0.1 m/s, (b) 0.2-0.35 m/s, (c) 0.7 m/s, and (d) 1.3 m/s.

displacement, the thickness of Unit 2 increases at the expense of Unit 1, and after 10-15 m of displacement, Unit 1 is present only in small regions at the cylinder axis and in some cases at the perimeter of the circular gouge layer. The data suggest that the rate that Unit 1 is consumed to form Unit 2 is high initially and then decreases with greater shear displacements.

Units 3 and 4 appear at less than 25 m of displacement at the higher representative slip velocities of 0.35, 0.7 and 1.3 m/s; forming at progressively smaller displacements as the slip velocity increases. For example, Units 3 and 4 first appear after about 10 m of displacement for shearing at 0.35 and 0.7 m/s (Figure 2.11b and 2.11c), but they are already present by 2.5 m of displacement for shearing at 1.3 m/s (Figure 2.11d). The two units typically occur together, both temporally and spatially, though in one case Unit 4 is produced without a record of Unit 3 (Table 2.1). At the higher velocities the microstructure and spatial distribution of both units are established when they form; the units grow inward and Unit 4 sometimes thickens by accumulation with displacement, but neither unit changes character significantly. The data suggest that the rate that Units 3 and 4 increase in volume is high when they form initially, and then decreases with increasing displacement.

2.6. Discussion

2.6.1. Correlation between weakening, slip velocity, temperature and gouge structure

Previous studies of high-speed friction on clay-bearing, quartzo-feldspathic gouge using the same rotary shear configuration as in the present study have concluded that the dramatic weakening observed at high slip velocity is due to the elevated temperature produced by frictional heating [e.g., *Mizoguchi et al.*, 2009; *Brantut et al.*, 2008; *Boutareaud et al.*, 2008]. The experiments reported herein are consistent with the above studies, showing systematic weakening during high velocity slip, but our experiments also show systematic weakening with increased normal stress, which is qualitatively consistent with the premise of thermal weakening from frictional heating. Direct measurements of temperature [e.g., *Mizoguchi et al.*, 2009] and our thermomechanical models indicate that the temperature increases significantly within gouge layers during shear at greater than 0.1 m/s at a normal stress on the order of 1 MPa; these conditions correlate to the slip velocities for dynamic weakening.

The structure of the sheared ultracataclasite gouge displays a distinct correlation with slip velocity and the onset of dynamic weakening. The fact that Units 1 and 2 are best developed in the lower speed experiments that correlate with a higher coefficient of friction and little apparent weakening with displacement, suggests that the processes that produce these microstructures are not responsible for the low coefficient of friction. In contrast, Units 3 and 4 are best developed in the higher velocity experiments and are present in all experiments that display pronounced weakening to a low coefficient of

friction. The correlation between microstructure and frictional strength suggests that the processes that produce Units 3 and 4 are responsible for the low coefficient of friction and are activated by an elevation of temperature.

The four gouge units identified here were not all noted in the experiments by *Brantut et al.* [2008], *Boutareaud et al.* [2008, 2010], and *Mizoguchi et al*. [2009], and a correlation between the formation of distinct gouge microstructures and the onset of dynamic weakening was not made. The previous studies focused on shearing at high velocity to large displacements where dynamic weakening is observed. These studies did not describe the microstructures in radial sections, and they did not conduct sequential displacement tests over a range of velocity and normal stress conditions that allow the correlation of specific behavior with specific microstructures. The previous studies all sheared clay-bearing, quartzo-feldspathic gouge, but *Boutareaud et al.* [2008, 2010] were the only ones to describe microstructures similar to those in Unit 3. In contrast, all previous studies reported the development of a localized slip zone similar to Unit 4. Taken together, the observations suggest that Unit 3 only forms under dynamic weakening conditions, but Unit 4 is the only unit that is observed in all cases of dynamic weakening during the rotary shear experiments. Based on the observations to date, we suggest that the formation of Unit 4 reflects the process that ultimately results in sustained dynamic weakening.

2.6.2. Gouge microstructure evolution and relation to weakening

2.6.2.1. Units 1 and 2

The formation of Unit 2 from Unit 1, and the distribution of all four units as a function of displacement, are consistent with a displacement and normal stress dependence for the formation of Unit 2. This unit begins to form at or near one boundary of the gouge layer and then expands with displacement at the expense of Unit 1. The expansion of Unit 2 inward and preservation of Unit 1 near the rotation axis would be expected if formation of Unit 2 requires a finite displacement or shear strain. In contrast, preservation of Unit 1 at the periphery of the gouge layer where the greatest cumulative displacement occurs, is not consistent with the above relations. The thermomechanical model, however, demonstrates that the gouge layer is less confined at large radii because of the variation in elastic loading. It is possible that the conversion of Unit 1 to Unit 2, by consolidation and comminution, is delayed by the reduction in normal stress at the periphery.

The distributed shear recorded by a clay foliation, reduction in particle size, and consolidation noted in Unit 2 are characteristics shared by many low velocity friction experiments on quartzo-feldspathic gouge at elevated pressures [*Moore et al.*, 1989; *Beeler et al.*, 1996; *Rutter et al.*, 1986]. These experiments also often display Riedel shears, which were noted in slip-parallel sections made from low velocity rotary shear experiments of *Mizoguchi et al.* [2009]. Reidel shears are not apparent in our experiments, but their existence would be less obvious because of the orientation of our thin sections.

Gouge experiments run at low slip velocities typically display coefficients of friction on order of 0.4 to 0.8, depending on the mineralogy, where the lower coefficients often are associated with the presence of clays and water-wet conditions [*Logan and Rauenzahn*, 1987; *Morrow et al.*, 2000; *Ikari et al.*, 2009]. Shear of polymineralic gouge layers containing clay or quartzo-feldspathic minerals demonstrate low-magnitude strengthening and weakening with changes in temperature [*Logan et al.*, 1981; *Moore et al.*, 1989]. For our experiments, temperature increases on the order of 100 ˚C from frictional heating with the associated formation of Units 1 and 2; these tests do not show pronounced weakening and thus are consistent with prior results of low velocity friction experiments on similar materials.

2.6.2.2. Units 3 and 4

The paired occurrence of Units 3 and 4 displayed in sequential displacement samples, the presence of fragments of Unit 4 in Unit 3 and of Unit 3 in Unit 4, and the spatial arrangement of these units suggest that the formation of Units 3 and 4 is contemporaneous, at least initially, and occurs after the formation of Unit 2. The pronounced particle size reduction of Unit 4 and the typical location of the unit at the gouge layer boundary are similar to the characteristics of localized shear zones observed in many prior experiments on gouge layers at low and intermediate slip velocities [*Logan et al.*, 1979; *Beeler et al.*, 1996]. The majority of displacement occurs within the localized zone, as is inferred here for Unit 4. The initial formation of Units 3 and 4 along a zone of concentrated shear at the boundary of the gouge layer is consistent with the wedge shape geometry of Unit 3 and the location of the interior vertex of the wedge

against the boundary of the gouge layer where Unit 4 is located. The structural evolution seen in sequential displacement tests further indicates that the wedge of Unit 3 grows inward with displacement by the propagation of the vertex along the boundary, and by the expansion of the wedge by incorporation and conversion of Unit 2 into Unit 3 (Figures 2.11b, 2.11c, and 2.11d).

The characteristics of Unit 3, such as the random fabric, massive texture, reduced particle size, and rounded clasts near the periphery of the layer, suggest granular deformation during a dynamic, fluidized flow rather than during frictional shearing flow. Fluidized behavior in a collection of particles is characterized by particle movement along a free path between collisions with other particles. Deformation of a fluidized material may result in a random fabric, although depending on the fluidization regime (frictional, macroviscous or grain-inertia), some grain size segregation or other layered flow-fabric may develop [*Otsuki et al.*, 2003; *Monzawa and Otsuki*, 2003; *Ujiie et al.*, 2007]. On the basis of observed microstructures, particularly of the spherical CCA, *Boutareaud et al.* [2008, 2010] conclude that the deformation of Unit 3 reflects vaporization of liquid water in the gouge during frictional heating. The transformation produces a significant decrease in water density which, depending on rate that the water vapor escapes through the gouge and past the Teflon sleeve, could produce a vapor pressure equivalent to the normal load [*Boutareaud et al.*, 2008, 2010]. *Boutareaud et al.* [2008, 2010] argue that the vaporization process causes the gouge to dilate and fluidize, and as a consequence, fine clay particles can aggregate and adhere to the core of the

CCA. In contrast, *Mizoguchi et al.* [2009] conclude that the escape of any water vapor produced during shear is sufficiently fast that pressurization should be minimal.

As shown by the thermal model of *Mizoguchi et al.* [2009] and the thermomechanical model herein, the rate that the temperature increases in the gouge from frictional heating is greatest at the periphery of the layer. Thus, the critical temperature for the liquid-vapor transition of water is achieved first in the outer portion of the circular gouge layer. The liquid-vapor transformation front should then migrate toward the center of the sample as temperature increases with shearing. The inward-tapered, wedge geometry of Unit 3 along the actively shearing boundary of the layer (recorded by Unit 4), and the inward expansion of the wedge with displacement are consistent with vaporization of water along the heated, slipping boundary, and with outward flow and escape of the vapor past the Teflon sleeve. Clearly, pressurized gas streaming outward could facilitate suspension of particles and fluidization of the gouge when the rate of vapor production is high.

Our observations support the conclusions that Unit 4 is produced at the expense of the other units, it is active throughout shearing, and it is the locus of shear at the larger displacements. *Brantut et al.* [2008] use transmission electron microscopy to document partial amorphization and dramatic grain size reduction (down to the nanometer scale) within the localized slip zone of Unit 4 to infer thermal dehydration of the clays due to shearing. The more pronounced chemical changes in Unit 4 likely reflect higher temperatures as would be expected if the majority of displacement is accommodated by slipping within Unit 4 at the boundary of the gouge layer.

2.6.3. Vaporization of water

The conclusion of *Boutareaud et al.* [2008, 2010], that Unit 3 results from the vaporization of pore water, can be tested using our sequential displacement experiments that explore a range of slip velocities, normal stress conditions and host-block type. The range of heating rates in these experiments and the temperature changes that can be determined from the thermomechanical model, give the pressure and temperature conditions during the development of Unit 3. Assuming that the vapor pressure equals the normal stress, these data suggest that the liquid-vapor transition should occur at temperatures of 120 to 192 ˚C for normal stresses from 0.2 to 1.3 MPa [*Lide*, 2006].

The experiments displaced at a representative velocity of 0.1 m/s do not achieve temperatures sufficient to vaporize water, and those run at the highest rate of 1.3 m/s achieve the liquid-vapor transition temperature at very small displacement. The experiment sheared to the largest displacement (HVR484gr), at a representative velocity of 0.1 m/s, reaches a representative temperature of 112 ˚C and does not display Unit 3, consistent with the conditions for the liquid-vapor transition (Figure 2.12a). At a representative velocity of 0.7 and 1.3 m/s, the smallest displacement experiments that display Unit 3 achieve representative temperature of 192 and 169 ˚C; these observations also are consistent with the conditions for the liquid-vapor transition (Figure 2.12b and 2.12c).

Two plots summarizing the occurrence of Unit 3 with respect to normal stress, displacement, velocity, and temperature show that Unit 3 forms at about 150 ˚C, regardless of the normal stress, displacement, and velocity (Figure 2.13). In detail, the

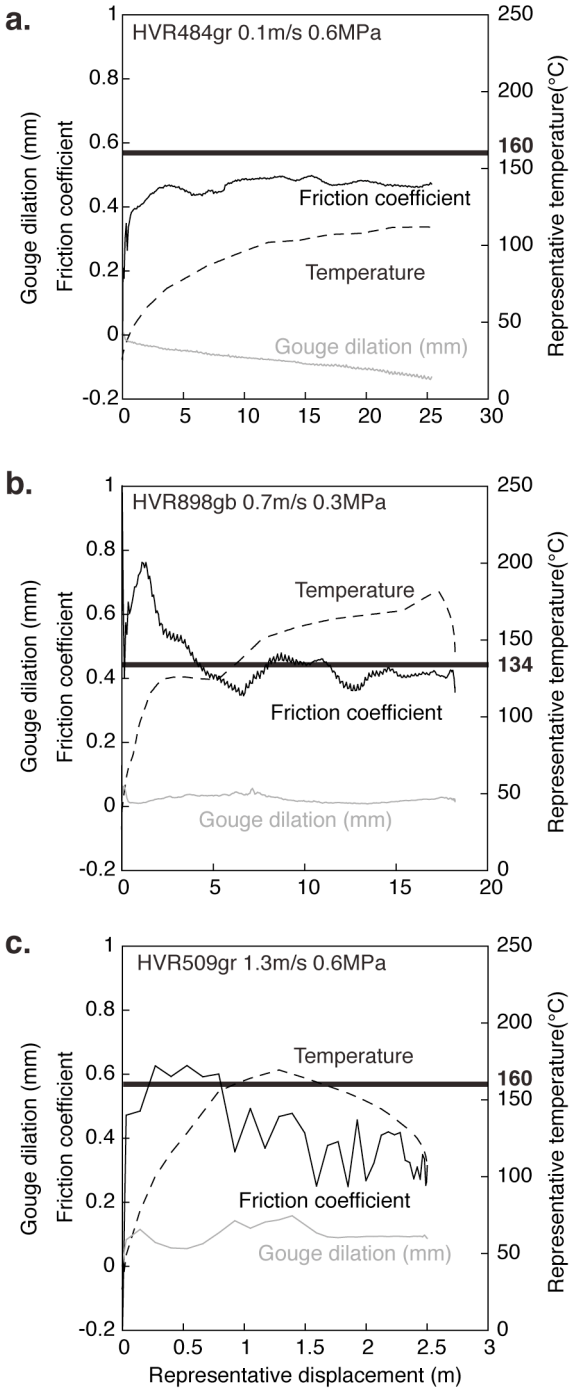

Figure 2.12. Results from three selected experiments to illustrate experimental constraint on the temperature at which Unit 3 is formed in the gouge layers. Friction coefficient (solid-black), representative temperature (dashed-black), and gouge dilation (solid-gray) versus representative displacement for shearing at normal stress of 0.6 MPa and representative slip velocity of (a) 0.1 m/s, (b) 0.7 m/s, and (c) 1.3 m/s. The bold lines and numbers represent the critical temperature for water vaporization assuming that the vapor pressure is equal to the average normal stress.

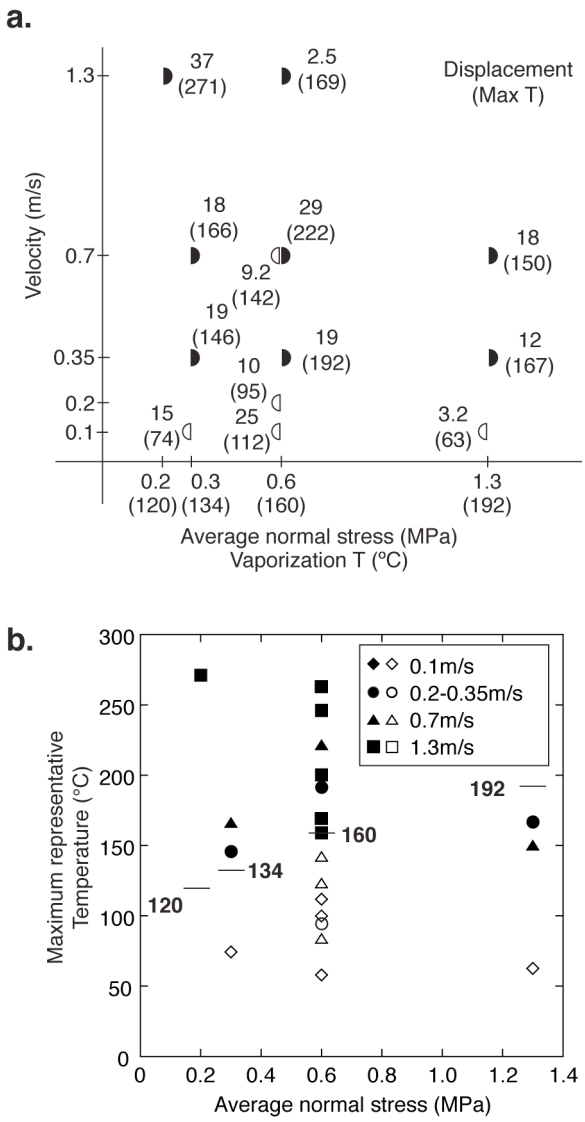

Figure 2.13. Summary plots showing the development of Unit 3 in sheared gouge as a function of normal stress, representative slip velocity, and maximum representative temperature. (a) Plot showing conditions at which Unit 3 was formed (solid symbols) or not formed (open symbols) as a function of velocity and normal stress. The numbers next to symbols indicate the final representative displacement and the maximum representative temperature (in parentheses) achieved in each experiment. The temperature of vaporization at each normal stress is shown in parentheses below the horizontal axis. (b) Plot showing the temperature and normal stress conditions for which Unit 3 was observed (solid symbols) or not observed (open symbols). The lines with numbers represent the critical temperatures for water vaporization at each normal stress assuming vapor pressure is equal to the normal stress.

lowest temperature at which Unit 3 is observed is 146 ˚C, and the greatest temperature at which Unit 3 is not observed is 142 ˚C (Figure 2.13a). In all cases where Unit 3 is observed, the calculated representative temperature is greater than the critical temperature for the liquid-vapor transition, assuming a vapor pressure equivalent to the normal stress (Figure 2.13b). In two cases sheared at the average normal stress of 1.3 MPa, however, the maximum representative temperature achieved in experiments displaying Unit 3 is less than the critical temperature for the liquid-vapor transition, again assuming a vapor pressure equivalent to the normal stress. This finding could indicate that the vapor pressure did not increase to the magnitude of the normal stress, i.e., the vapor escaped the gouge layer at a rate nearly equal to its formation, consistent with the calculations of *Mizoguchi et al.* [2009].

The thermomechanical model may overestimate the temperatures achieved for cases where Unit 3 is formed because the model assumes heat transfer by conduction, and does not consider dehydration of clay minerals, the liquid to vapor transition of water, or the transfer of heat by escape of the vapor from the gouge layer. The latent heat associated with dehydration of clay minerals and the liquid-vapor transition of water, and the transfer of hot vapor out of the layer could limit the temperature increase from frictional heating. To estimate the possible effect of these processes on the temperature calculations, the total energy from friction in the gouge layer (E_{total}), the energy for heating (E_{heat}), the energy for vaporization (E_{vapor}) of water, and the energy for dehydration of smectite (E_{dehy}) are calculated. E_{total} and E_{heat} are given by,

$$E_{total} = \int_0^t \int_0^{2\pi} \int_0^{r_s} \tau(r,t) \cdot r \, dr \, d\theta \cdot v(r,t) dt$$

$$= 2\pi \int_0^t \int_0^{r_s} r \cdot \mu(t) \cdot \sigma(r,t) \cdot (2\pi\omega r) \, dr \, dt \tag{2.13}$$

and

$$E_{heat} = \int_0^h \int_0^{2\pi} \int_0^{r_s} c\rho \Delta T(r,z) r \, dr \, d\theta dz$$

$$= 2\pi c\rho \int_0^h \int_0^{r_s} \Delta T(r,z) r \, dr \, dz \,, \tag{2.14}$$

where h is the thickness of gouge layer, c is heat capacity, ρ is density, and ΔT is temperature change. We use heat capacities of 1.0 (J/g·K) for the gouge and 4.184 (J/g·K) for water, and densities of 2.0 (g/cm^3) for the gouge and 1.0 (g/cm^3) for water, respectively. E_{vapor} is determined as the vaporization energy of water in the area where the temperature exceeds the vaporization temperature, assuming vapor pressure equals the normal stress for each experiment. The enthalpy of vaporization of water is 2.2-1.97 kJ/g at 120-190 °C [*Lide*, 2006], and the total content of water in the gouge layer is assumed to equal the water added at the beginning of the experiment. Similarly, E_{dehy} is calculated as the dehydration energy of smectite in the area where the temperature exceeds the critical temperature for dehydration. *Koster van Groos and Guggenheim* [1986] found that the first and second dehydration reactions at pressure occurred at about 50 °C and 100 °C above the liquid-vapor transition, and determined the enthalpy of the dehydration for each reaction were approximately 46 kJ/mol and 60 kJ/mol, respectively.

Total energy per unit area results in 0.4-13×10^6 (J/m^2), depending on slip velocity and displacement, and E_{heat}, E_{vapor}, and E_{dehy} make up 5-37%, 6-28%, and 0.04-6% of total energy, respectively (Table 2.1). Thus, the amount of energy that could be transferred out of the gouge layer during periods of vaporization is significant. In fact, the temperatures achieved in the gouge layer as a whole may be limited to the liquid-vapor transition temperature as long as liquid water is present in the layer. This conclusion means that the temperature is held at the vaporization temperature as displacement increases in experiments sheared at the lower rates.

2.6.4. Temperature dependence of friction in localized slip zone

The conditions favoring the development of Units 3 and 4, i.e., the conditions at which the temperature in the gouge layer rises above 150 ˚C, correlate well with the onset of dynamic weakening (Figure 2.13). Thus the deformation processes operating in the units are good candidates for dynamic weakening mechanisms. The unique microstructure of Unit 3 and the possibility that Unit 3 reflects a vapor pressure increase that approaches the normal load during shearing, support the hypothesis that the low dynamic strength could, in part, reflect thermal pressurization and shearing under a fluidized state in Unit 3. Yet the fact that Unit 4 is present in all experiments that display dynamic weakening and that it appears to accommodate the majority of displacement, suggests that Unit 4 provides the least resistance to shearing.

A few high-velocity rotary slip-hold-slip experiments on gouge layers demonstrate that original strength is recovered after short (tens of seconds) hold times and that

subsequent sliding displays an evolution of friction to a dynamic weakened state similar to that for initial loading [*Mizoguchi et al.*, 2009; *Kitajima et al.*, 2006]. This strength recovery suggests that the presence of Units 3 and 4 is not sufficient for dynamic weakening. Rather, Units 3 and 4 are dynamically weakened only if temperature is increased sufficiently high through frictional heating.

2.6.5. Critical displacement for weakening

The results of previous rotary shear experiments on split cylinders of rock, with and without gouge layers, have been used to guide modeling of the breakdown in strength and the critical slip distance for weakening for earthquake rupture [e.g., *Hirose and Shimamoto*, 2005; *Mizoguchi et al.*, 2007]. One outcome of the rotary shear experiments is that the critical slip distance is decreased and the magnitude of weakening is increased with an increase in normal stress. Such a dependence on normal stress is consistent with expectations for thermal weakening processes because the heating rate for frictional slip is directly dependent on normal stress. The relatively large critical slip distances observed in the rotary shear experiments at low normal stress appear compatible with slip weakening distances for earthquakes, if one accounts for the increased heating rate associated with high normal stress in the seismogenic regime [*Mizoguchi et al.*, 2007]. Such analyses, however, remain problematic given the heterogeneous nature of deformation in rotary shear experiments.

In the present experiments, dynamic weakening appears to require not only the establishment of Units 3 and 4 but also a slip velocity sufficient to elevate temperature

along the surface through frictional heating. On the basis of microstructural observations and thermomechanical modeling, it is clear that the required conditions for dynamic weakening are achieved initially in a restricted region at the periphery of the gouge layer. Simultaneously, in the central portion of the sample where Units 1 and 2 form and the heating rates are much lower, the gouge layer remains relatively strong. As a result, the dynamic weakening observed at high effective slip velocity reflects the progressive inward expansion of the hot, weaker Units 3 and 4 at the expense of the interior region of the gouge where shearing is within the stronger Units 1 and 2. It must be concluded that the critical slip distance determined directly is a bulk response of the sample, and that to a certain extent the magnitude of the critical slip distance reflects the heterogeneous velocity and stress conditions imposed in the rotary configuration. As such, it is misleading to attempt to determine a unique critical slip distance from a rotary shear experiment without accounting for the heterogeneous conditions. Similarly, the measured torque also must be regarded as a bulk response, and the calculation of a coefficient of friction for the gouge layer assuming friction is uniform is misleading.

The use of the thermomechanical model, which allows for variable normal stress from thermoelastic deformation of the sample assemblies, to determine friction from experimental data is an improvement over previous methods that are based on the assumption of uniform shear stress in the gouge layer. Nonetheless, the assumption of uniform friction in the modeling also must be relaxed in order to adequately account for the heterogeneous conditions and in order to extract meaningful friction constitutive parameters.

2.7. Conclusions

1) The microstructural observations of the sheared gouge, and analysis of experimental data using thermomechanical models of the sample assembly, indicate that heterogeneous conditions of stress, temperature, and frictional-slip processes occur within the high-speed rotary shear experiments. The heterogeneity must be characterized to understand friction behavior and the underlying microscopic slip processes.

2) Dynamic weakening is observed in experiments conducted at slip rates greater than about 0.3 m/s where frictional heating rates are sufficient to elevate the temperature of the gouge layer; dynamic weakening is facilitated by increases in normal stress, shear displacement and water, consistent with a temperature-dependent weakening process. Host block composition also can indirectly affect dynamic weakening; samples with granite blocks result in higher temperature and larger dilation than those with gabbro blocks because of the lower thermal diffusivity of granite.

3) On the basis of the maximum particle size, particle shape, development of clay foliation, and degree of localization of shear, four distinct microstructural units are identified within the sheared gouge layers. Unit 1 is similar to the disaggregated starting material but slightly compacted due to shear, whereas Unit 2 displays a clay foliation resulting from the comminution and distributed shear of Unit 1. Unit 3 displays a random clay fabric and reduced particle size that records fluidized flow. Unit 4 occurs within a thin zone of concentrated shear, displays extreme grain size reduction and a strong foliation, and is often located along the contact of the gouge and host block.

4) Units 1 and 2 generally occur in regions subjected to lower slip velocity and smaller shear displacements, and are associated with higher coefficients of friction. Units 3 and 4 occur together and are formed in the samples sheared at higher slip rates to larger displacements, the same conditions where dynamic weakening of the gouge layer is observed.

5) Formation of the fluidized structure in Unit 3 occurs at the critical temperature for vaporization of water. The vapor pressurization and streaming flow of vapor through the gouge layer likely facilitates fluidized behavior in Unit 3.

6) The observed dynamic weakening appears to require both the establishment of the localized slip surface recorded by Unit 4, and a slip velocity sufficient to elevate temperature along the surface through frictional heating. Marked weakening of the gouge occurs at temperatures above the vaporization temperature of water, however, formation of pressurized water vapor may not be directly responsible for the pronounced weakening.

7) Given the heterogeneous stress, temperature, and friction in the gouge layers, the determination of friction constitutive behavior from the rotary shear experiments requires advanced thermomechanical modeling in which traditional assumptions of data analysis are relaxed to allow treatment of spatially variable normal stress and coefficient of friction.

3. DYNAMIC WEAKENING OF GOUGE LAYERS BY THERMAL PRESSURIZATION AND TEMPERATURE-DEPENDENT FRICTION IN HIGH-SPEED SHEAR EXPERIMENTS

3.1. Introduction

Over the last decade, frictional behavior of rock at slip rates greater than 0.1 m/s have been investigated, and both rock-on-rock and gouge-layer experiments show significant weakening at these rates [e.g., *Tsutsumi and Shimamoto*, 1997; *Golsby and Tullis*, 2002; *Hirose and Shimamoto*, 2005; *Mizguchi et al.*, 2009]. Several dynamic weakening mechanisms have been proposed, including flash heating [*Rice*, 1999, 2006; *Beeler et al.*, 2008], thermal pressurization of pore fluid [*Sibson*, 1973; *Lachenbruch*, 1980; *Mase and Smith*, 1987], shear melting [*Spray*, 1993; *Tsutsumi and Shimamoto*, 1997; *Hirose and Shimamoto*, 2005; *Di Toro et al.*, 2006], silica gel formation [*Goldsby and Tullis*, 2002; *Di Toro et al.*, 2004], normal interface vibration [*Brune et al.*, 1993], elastohydrodynamic lubrication [*Brodsky and Kanamori*, 2001], and transformation weakening [*Han et al.*, 2007]. Significant progress has been made in understanding some of the mechanisms, but more work is required to determine which mechanisms are significant to natural faulting and to develop appropriate constitutive descriptions.

Friction behavior determined at slip rates smaller than 1 mm/s is well described by rate- and state-dependent constitutive laws largely based on micromechanical models of time-dependent processes at areas of contact [*Dieterich*, 1979; *Ruina*, 1983]. Because rate dependence, specifically velocity weakening, can explain the nucleation of slip instabilities, rate and state friction laws have been used in mechanical models of faults to

investigate slip instability and earthquake occurrence [e.g., *Tse and Rice*, 1986; *Rice*, 1993; *Lapusta et al.*, 2000]. In contrast, constitutive relations capable of describing the frictional behavior observed in high-speed friction experiments are poorly developed. The general frictional response seen at slip-rates greater than 0.1 m/s consists of a slip-weakening behavior characterized by an initial-peak friction coefficient, μ_{peak}, an evolution to a steady-state friction coefficient, μ_{ss}, over a characteristic slip-weakening distance, d_c, and a reduction in μ_{ss} with increase in slip rate [e.g., *Tsutsumi and Shimamoto*, 1997; *Hirose and Shimamoto*, 2005; *Brantut et al.*, 2008; *Mizoguchi et al.*, 2009]. In some cases the weakening has been attributed to the flash heating mechanism, which describes thermal weakening of asperity contacts from a local temperature increase that depends on contact size, slip rate, and thermal properties [*Rice*, 1999, 2006; *Beeler et al.*, 2008]. *Sone and Shimamoto* [2009] describe the evolution of friction strength, including the three stages of strengthening, weakening, and recovery that are observed during changing-velocity rotary-shear experiments, by assuming a velocity-dependent steady-state friction coefficient and a displacement-dependent, initial-peak friction coefficient. Although it is well recognized that frictional heating is important at high slip rates, and many of the proposed mechanisms for dynamic weakening are thermally activated processes, there has been little effort to apply constitutive relations with temperature dependence to the results of high-speed friction experiments.

The purpose of this paper is to use thermal-, mechanical-, and fluid-flow-coupled finite element (FEM) models of high-speed, rotary-shear experiments on thin layers of gouge comprised of disaggregated ultracataclasite from the Punchbowl fault to (1) assess

the efficacy of state-variable, temperature dependent constitutive relations in describing the frictional response, (2) evaluate the contribution of flash heating and thermal pressurization to dynamic weakening, and (3) better describe heterogeneous evolution of the friction coefficient, normal stress, pore pressure, temperature, and microstructure during rotary shear. The FEM modeling extends the work of *Kitajima et al.* [2010] in analyzing high-speed rotary-shear experiments, and treats both the original tests employing constant velocity loading, and new tests incorporating constant acceleration, changing velocity loading.

3.2. Temperature-dependence of Friction in High Slip-rate Experiments

3.2.1. Experiment methods and FEM-based analysis

High-speed rotary-shear experiments were conducted on 1-mm-thick layers of gouge between two cylindrical host blocks of granite or gabbro (25 mm diameter) confined but not sealed by a Teflon sleeve (Figure 3.1a). The gouge consists of gently disaggregated Punchbowl fault ultracataclasite [*Kitajima et al.*, 2010]. 'Water-dampened' and 'room-dry' samples were prepared with or without adding 0.3 g of distilled water, respectively. All experiments were conducted at room temperature and humidity conditions. Normal load was applied and kept constant at the end of the stationary host block, and rotation of the rotating host block was driven by an electric motor. A clutch was used to quickly reach the target rate for constant velocity experiments while the velocity and acceleration was manually controlled for constant acceleration experiments. Normal load, total torque, rotation speed, and axial displacement were measured during

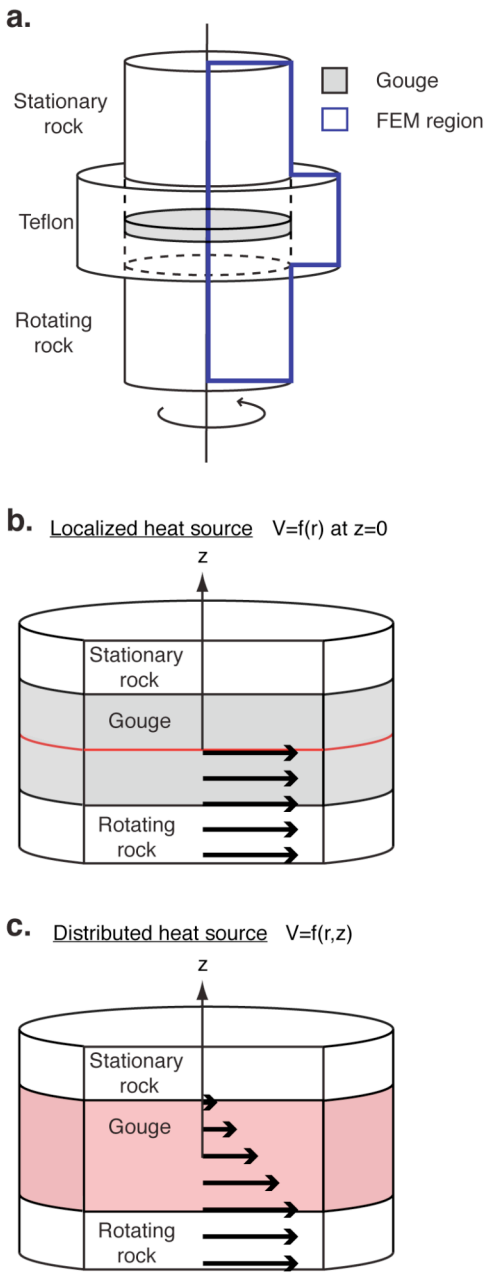

Figure 3.1. Diagrams of the sample assembly and heat source distributions. (a) Diagram of the sample assembly showing the position of the gouge layer, host blocks, and Teflon sleeve. The region outlined in blue indicates the portion of the axial-symmetric assembly modeled using FEM. Cut-away view showing the velocity distributions in the gouge layer for the (b) localized slip and (c) distributed shear cases. The bold arrows indicate the magnitude of local velocity relative to the stationary host block at a given radius. For the localized case, frictional slip and the associated heat generation are assumed to occur at the midplane of the gouge layer. For the distributed shear case, heat generation rate increases with radius but is constant with z in the gouge layer.

experiments. The measurement of the total torque was reduced by the torque supported by the friction between the Teflon sleeve and host blocks before analysis of gouge friction. In the rotary shear configuration, slip velocity and displacement vary with radius r, from zero at $r = 0$ to the maximum values at $r = r_s$. For reference, the velocity, temperature and displacement at $r = 2r_s / 3$ are used to describe general conditions of each experiment as a representative slip velocity V_{eq}, a representative temperature T_{eq}, and a representative displacement d_{eq}. After experiments, the samples were cut through the axis of host block cylinder to produce radial cut thin sections oriented perpendicular to the slip direction. The radial cut sections were used to characterize the evolution of deformed microstructures as a function of radius, velocity, and displacement [*Kitajima et al*., 2010].

Numerous constant velocity experiments were conducted for a parametric study of slip rate, normal stress, total displacement, water content, and host block type [*Kitajima et al*., 2010]. Normal stresses of 0.2-1.3 MPa, slip velocities of 0.1-1.3 m/s, and the total displacement of 1.3-84 m were achieved. Among tens of experiments, the results of four representative experiments sheared at normal stress of 0.6 MPa and different slip rates are analyzed in this study (Table 3.1). In addition to the constant velocity experiments reported by *Kitajima et al*. [2010], constant acceleration experiments were conducted for a parametric study of loading path, acceleration rate, and water content. Slip velocities were manually increased and decreased between 0 and 1.3m/s with constant accelerations of 0.05 or 0.1 m/s^2 (Table 3.1). These experiments are similar to "changing-velocity experiments" reported by *Sone and Shimamoto* [2009] and *Sawai et*

Table 3.1. Summary of high-speed experiments. gr and gb after the experiment number represent host rock type of granite and gabbro. σ_n: average normal stress, V_{eq}: representative slip rate, a_{eq}: representative acceleration rate, d_{eq}: representative displacement.

	σ_n (MPa)	V_{eq} (m/s)	a_{eq} (m/s^2)	d_{eq} (m)	dry or wet
Constant velocity experiment					
HVR484gr	0.6	0.1	-	25	wet
HVR809gb	0.6	0.35	-	19	wet
HVR530gr	0.6	0.7	-	29	wet
HVR482gr	0.6	1.3	-	83	wet
HVR475gr	0.6	1.3	-	84	dry
Constant acceleration experiment					
HVR952gb[1]	0.6	0-1.3	0.1	19/19	wet
HVR955gb	0.6	0-1.3	0.05	32	wet
HVR956gb	0.6	0-1.3	0.05	32	dry

[1] Includes two consecutive runs.

al. [2009], however, our acceleration rates are much lower than those of the changing-velocity experiments. As summarized in Table 3.1, room-dry gouge was used in an experiment (HVR955gb) and water-damped gouge was used in other experiments (HVR952gb and HVR956gb). The experiment HVR952gb includes two successive runs, HVR952gb-1 and HVR952gb-2, and the sample was held stationary with normal load maintained for 20 minutes between the runs.

In the previous study of *Kitajima et al.* [2010], mechanical data from each experiment was analyzed using a coupled thermo-mechanical FEM model, which can treat frictional heating, heat transfer, and thermal expansion, to determine the spatial and temporal variation in normal stress and temperature within the samples and the magnitude of gouge dilation by subtracting the calculated thermal expansion from the measured axial displacement. It should be emphasized that the previous analysis of high-speed friction experiments using the FEM model was based on the assumption of a uniform coefficient of friction in the layer. With this assumption, and that the local normal stress on the layer is given by the FEM model, the coefficient of friction could be determined directly from the measured torque corrected for Teflon friction. All the details of the method, thermal-mechanical FEM model, mechanical results, and microstructure analysis of constant velocity experiments are described in *Kitajima et al.* [2010].

3.2.2 Evidence that dynamic weakening reflects temperature dependent friction

Comparison of frictional strength and temperature in constant velocity experiments shows that dynamic weakening occurs at slip rates larger than 0.35 m/s where frictional

heating rates are sufficient to elevate the temperature of the gouge layer, and no dramatic weakening is observed at the lowest slip rate of 0.1 m/s where temperature changes are minimal [*Kitajima et al.*, 2010]. The series of experiments suggest that the weakening process is strongly temperature-dependent, because it is facilitated by increases in normal stress and velocity. Dynamic weakening is achieved with elevation of temperature regardless of the combination of velocity, displacement, normal stress, and host-rock thermal conductivity to produce the increase of temperature. Layer microstructure changes at the critical temperature for weakening, consistent with the activation of a distinct high-temperature slip process responsible for dynamic weakening.

In the constant-acceleration experiments, the evolution of frictional strength is similar for different acceleration, but is significantly different for room-dry and water-dampened samples [*Kitajima et al.*, 2007]. For the experiment on the room-dry sample, the coefficient of friction gradually increases to 1.2 when slip velocity reaches at approximately 0.2 m/s, followed by weakening with increasing velocity. For the experiments on water-dampened samples, on the other hand, coefficient of friction largely decreases after the initial peak, followed by slight increase and another decrease during acceleration. Both room-dry and water-dampened samples show partial recovery of frictional coefficient during deceleration. Although abrupt dynamic weakening is not observed in constant-velocity experiments on gouge of disaggregated Punchbowl ultracataclasite, it is observed in high-speed, constant-velocity experiments on some other water-dampened clay-rich gouge [e.g., *Kitajima et al.*, 2006; *Faulkner et al.*, 2009;

Togo et al., 2009]. Abrupt weakening could reflect thermal pressurization in water-dampened samples at high-speed, even though the Teflon sleeve used to contain the gouge is not expected to seal fluids (Figure 3.1a).

The relationship between evolving temperature and friction in the various experiments is illustrated in Figure 3.2. For room-dry samples, friction coefficient in both the constant-velocity experiment (HVR475gr) and the constant-acceleration experiment (HVR956gb) initially increases and then decreases as temperature rises over the course of the experiment (Figure 3.2a). Similar though not as quite pronounced behavior of strengthening then weakening is observed in the constant-velocity experiments on wet samples (Figure 3.2b). Differences in the relationships between evolving temperature and friction for room-dry and wet samples suggest other thermal- and water-related process is operative, such as thermal pressurization of pore fluid. The data shown in Figure 3.2 are determined by FEM modeling assuming the friction coefficient is spatially uniform, but observations described above indicate the velocity, temperature, normal stress and friction coefficient vary with position in the samples. Thus the relationships in Figure 3.2 represent an average, bulk response of the samples and likely do not indicate the exact relationship between temperature and friction. Nonetheless, the existence of a temperature-strengthening regime at lower temperatures (low-T regime) and a temperature-weakening regime at higher temperatures (high-T regime) is certain.

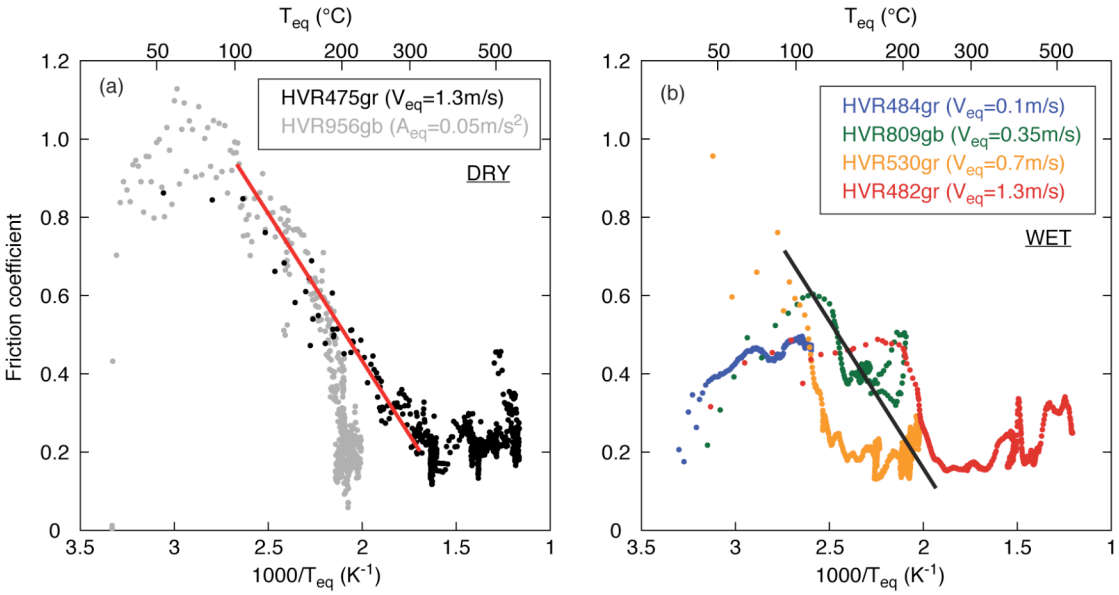

Figure 3.2. Plots of friction coefficient versus representative temperature for selected constant velocity and constant acceleration experiments. Red and black lines indicate the inferred temperature-weakening relationship in the high temperature regime for a) room-dry and b) wet gouge. Plotted values were determined from analysis of experiments using the FEM model of *Kitajima et al.* [2010] assuming the coefficient of friction in the gouge is independent of position (see text). The representative temperature, T_{eq}, is a determined at r=2/3r_s. (a) Room-dry gouge experiments of HVR475gr sheared at a constant representative velocity of 1.3 m/s and HVR956gb sheared at a constant representative acceleration of 0.05 m/s^2. (b) Wet gouge experiments of HVR484gr, HVR809gb, HVR530gr, and HVR482gb sheared at constant representative velocities of 0.1, 0.35, 0.7, and 1.3 m/s, respectively.

3.2.3. Temperature-dependent constitutive friction relations

Chester [1994] extended a rate and state friction constitutive relation to account for the effect of temperature on the basis of the assumption that the micromechanisms of friction are thermally activated and follow an Arrhenius relationship. The rate-, state-, and temperature-dependent friction constitutive law (the slip law) is expressed by

$$\mu = \mu^* + A\left[\ln\left(\frac{V}{V^*}\right) + \frac{Q_A}{R}\left(\frac{1}{T} - \frac{1}{T^*}\right)\right] + B\Theta, \tag{3.1}$$

and

$$\frac{d\Theta}{dt} = -\frac{V}{D_c}\left[\Theta + \ln\left(\frac{V}{V^*}\right) + \frac{Q_B}{R}\left(\frac{1}{T} - \frac{1}{T^*}\right)\right], \tag{3.2}$$

where V, T, and Θ are slip velocity, temperature, and state variable. A, B, and D_c are constitutive parameters. R is the gas constant; Q_A and Q_B are the activation energy for the direct and evolution effects, respectively. At steady state, $\mu_{ss} = \mu^*$ for $V = V^*$ and $T = T^*$. From Eqs (3.1) and (3.2), the steady state friction coefficient is given by

$$\mu_{ss} = \mu^* + (A - B)\ln\left(\frac{V}{V^*}\right) + C\left(\frac{1}{T} - \frac{1}{T^*}\right), \tag{3.3}$$

where $C = \frac{(AQ_A - BQ_B)}{R}$, and $C = \frac{(A - B)Q}{R}$ for $Q = Q_A = Q_B$.

Velocity and temperature dependence is expressed as

$$\left(\frac{\partial \mu_{ss}}{\partial(\ln V)}\right)_{T=const.} = A - B, \tag{3.4}$$

and

$$\left(\frac{\partial \mu_{ss}}{\partial(1/T)}\right)_{V=const.} = C, \tag{3.5}$$

respectively.

The parameter of temperature dependence described by (3.5) should be determined in experiments when velocity is constant, or if velocity dependence given by (3.4) is known. Unfortunately, using velocity stepping tests to directly measure velocity dependence was not attempted in the rotary shear apparatus. However, the range of velocities tested (0.1 to 1.3 m/s) is small relative to the changes in temperature, so the changes in friction resulting from velocity change is likely smaller than the changes in friction due to changes in temperature that take place at the high slip rates. They are also likely small relative to the variation in base-level friction, μ^*, typically observed in friction tests. Accordingly we can ignore velocity dependence and infer the magnitude and sign of the temperature dependence directly from the slopes of the friction versus the reciprocal of temperature plot of room-dry experiments (Figure 3.2). Together with the assumption that friction during constant-velocity, high-speed tests is close to steady state conditions, at least to first-order approximation, we can characterize temperature dependence in (3.5) as C=-2000 K for the low-T, temperature-strengthening regime and as C=750 K for the high-T, temperature-weakening regime.

3.3. Thermo-mechanical and Fluid Flow FEM Model

For the present analysis, the thermomechanical FEM model of *Kitajima et al.* [2010] is extended to treat spatial and temporal variation of the coefficient of friction and pore

fluid pressure resulting from thermomechanical effects and fluid flow in the porous media. The results of forward models based on the experimental parameters, assumed material properties, and temperature-dependent friction constitutive relations, are compared to the measurements of torque in the experiments to evaluate the veracity of the friction constitutive relations, as well as to evaluate the character of frictional shear and the associated heat source, and constrain some physical properties such as gouge permeability.

The torque carried by the sheared layer $\overline{M_s}$ is computed at $z = 0$ by

$$\overline{M_s}(t) = 2\pi \int_0^r \mu_s(r,t) \cdot \left(\sigma_n(r,t) - p(r,t)\right) \cdot r^2 dr, \tag{3.6}$$

where μ_s is coefficient of friction of gouge layer, and σ_n and p are normal stress and pore pressure. In detail, the friction coefficient is a function of temperature, which is allowed to vary with position and time, i.e., $\mu_s(r,z,t) = \mu_s(T)$ and $T = T(r,z,t)$. Note that the approach herein contrasts with that taken in *Kitajima et al.* [2010] in which pore pressure is ignored and the coefficient of friction can vary with time but not with position.

We solve the conservation equations of heat and fluid mass to predict the evolution of temperature and pore pressure during shear. The conservation equation of heat within the gouge is

$$\rho c \frac{\partial T}{\partial t} - \nabla \cdot \left(K \nabla T\right) = \tau \dot{\gamma} \tag{3.7}$$

,

where ρ is density, c is heat capacity, K is thermal conductivity, and $\tau\dot{\gamma}$ is the heat generation rate per unit area . The conservation equation of fluid mass within the gouge layer is

$$\rho_f \beta \frac{\partial p}{\partial t} - \nabla \cdot \left(\alpha_{hy} \nabla T \right) = \rho_f \phi \left(\lambda_f - \lambda_n \right) \frac{\partial T}{\partial t} \tag{3.8}$$

where p is pore pressure, ρ_f is fluid viscosity, β is the volumetric pore fluid storage coefficient, α_{hy} is hydraulic diffusivity, ϕ is porosity, λ_f is fluid thermal expansivity, and λ_n is pore space thermal expansivity. β and α_{hy} are expressed by $\beta = \phi\left(\beta_f + \beta_n\right)$ and $\alpha_{hy} = k/(\eta_f \beta)$, respectively, where β_f is fluid compressibility, β_n is pore space pressure expansivity, k is permeability, and η_f is fluid viscosity [e.g., *Rice*, 2006].

Assuming that all frictional work is converted to heat, we consider the two cases of either a localized or distributed heat source within the gouge layer as would be expected for localized or distributed shear, respectively. For the localized shear and heat source, it is assumed that all slip occurs at the mid-plane of the layer (Figure 3.1b). For the distributed shear and heat source, it is assumed that shear strain rate is independent with z in the gouge layer (Figure 3.1c). In addition to the heat source in the gouge, the heat generation at the boundary between Teflon sleeve and the rotating host block also is treated [*Kitajima et al.*, 2010].

To best model the starting condition of the experiments, the gouge is saturated with water, the stress in the layer is isotropic with magnitude σ_n, and the pore fluid pressure is zero at t = 0. The temporal evolution of porosity is expressed by $\phi(t) = \phi_0 + \Delta(t)$,

where ϕ_0 is initial porosity and Δ is volumetric strain computed by the thermomechanical FEM model. Permeability of the granite and gabbro host-blocks are set to 10^{-17} m^2 and 10^{-18} m^2, respectively [*Zhang et al.*, 2001; *Hirose and Hayman*, 2008]. We assume high permeability of 10^{-13} m^2 for the Teflon sleeve to simulate the relatively poor seal between the sleeve and the host block.

The most uncertain parameter is the permeability of gouge layer during shear at high slip rates. In general, gouge permeability decreases with increasing effective stress and decreasing porosity [e.g., *Wibberley*, 2002]. Permeability measurements on clay-rich gouge during friction experiments at slow strain rates show that permeability decreases with shear strain [*Takahashi et al.*, 2007; *Crawford et al.*, 2008; *Ikari et al.*, 2009]. In contrast, no measurement of permeability has been conducted during experiments sheared at high slip rates. *Tanikawa et al.* [2010] measured permeability before and after rock-on-rock rotary shear at slip rates of 10^{-4} to 1.3 m/s on Berea sandstone, Indian sandstone, and Aji granite. For the relatively impermeable rocks, permeability is increased significantly due to thermal cracking when slip rates exceed 0.1 m/s. However, the samples tested by *Tanikawa et al.* [2010] are not similar to the present case of weak gouge layer between the host blocks.

In addition to assuming constant permeability of the gouge layer, we test two cases assuming that permeability is a function of (1) effective normal stress, and (2) porosity. There are several proposed relationships between permeability and effective normal stress, e.g., a log-linear relationship [e.g., *Rice*, 1992] and a cubic law [*Gangi*, 1978; *Kwon et al.*, 2004]. Since the pressure range in this study is as small as 0.6 MPa, we

Table 3.2. Thermal, mechanical, and hydraulic properties of each component in the FEM model.

	Gouge layer	Host blocks		Teflon
		Granite	Gabbro	
Young's modulus (GPa)	0.01	60	80	0.05
Poisson's ratio	0	0.25	0.18	0.25
Density (g/cm^3)	2.0	2.6	2.95	2.2
Thermal expansion coefficient (K^{-1})	2.4×10^{-5}	2.4×10^{-5}	1.6×10^{-5}	2.4×10^{-5}
Thermal conductivity (W/m·K)	1.5	2.0	3.0	0.24
Heat capacity (J/g·K)	1.0	0.8	1.0	1.05
Porosity (%)	0.25	0.05	0.05	0
Permeability (m^2)	$k(\sigma_n')$ $k(\phi)$	10^{-17}	10^{-18}	10^{-13}

simply use a log-linear relationship [*Rice*, 1992], $k = k_{\sigma_0} \exp\left(-(\sigma_n - p)/\sigma^*\right)$ for case (1), where k_{σ_0} is the permeability at zero effective stress (10^{-15} m^2), σ_n is normal stress, and σ^* is a reference pressure of 0.1 MPa. For case (2) a log-linear relationship between permeability and porosity is used [*Bryant*, 1975; *Neuzil*, 1994; *Saffer and Bekins*, 1998; *Gamage and Screaton*, 2006], given by $k = k_{n_0} \cdot 10^{5.25n}$ where k_{n_0} is the reference permeability (10^{-19} m^2) when porosity n is zero.

Thermal, elastic, and hydraulic properties of the gouge layer, host blocks, and Teflon sleeve are summarized in Table 3.2. The thermal and elastic properties are same as those used in *Kitajima et al.* [2010]. We consider the change in physical properties of water with pressure and temperature, however, neither two-phase flow of water and vapor, nor the thermodynamics of vaporization, is considered here. In addition, the thermal-expansion coefficient of water is included in the fluid mass conservation equation, but not in thermal stress calculation. The same conditions and parameters, including the temperature-dependent constitutive relationship for friction, are used in all model simulations of the experiments.

3.4. Results

3.4.1. Constitutive model of friction for high-speed friction experiments

Using the inferred temperature dependency of friction in the low-T, temperature-strengthening regime and the high-T, temperature-weakening regime, and iteratively adjusting friction parameters during forward modeling to match friction behavior

displayed in the experiments, we are able to reproduce adequately the frictional behavior observed in all the tests using a two-mechanism friction-constitutive model. The model is constructed similar to other multi-mechanism friction-constitutive models [e.g., *Chester*, 1988, 1995]. From (3), and by ignoring velocity dependence, the friction behavior under dry conditions may be expressed as

$$\mu = \mu^* + C\left(\frac{1}{T} - \frac{1}{T^*}\right) \tag{3.9}$$

where μ^* =1.0, T^* =353 K, and with C = -2000 K for the low-T mechanism (temperature-strengthening regime) and C = 750 K for the high-T mechanism (temperature-weakening regime) (Figure 3.3). The two friction mechanisms are treated as independent, i.e., operating parallel-concurrent such that the mechanism with the lowest friction coefficient dominates the combined behavior [e.g., *Chester*, 1988, 1995]. The experiment results indicate that under wet conditions the friction is reduced in the high-T regime, and thus for wet conditions the behavior is best described by (3.9) where μ^* = 0.82 and T^* =345 K, but with the same values of C for the low-T and high-T mechanisms (Figure 3.3).

Although the two-mechanism model adequately treats the behavior throughout the majority of each experiment, it does not treat friction at low temperature at the very beginning of tests, particularly at low velocity as occurs at low radius inside the gouge layer. This likely reflects a problem with ignoring velocity dependence at low temperatures where the constitutive description for the low-T mechanism gives very small friction coefficients and the fact that friction is certainly far from steady-state at the

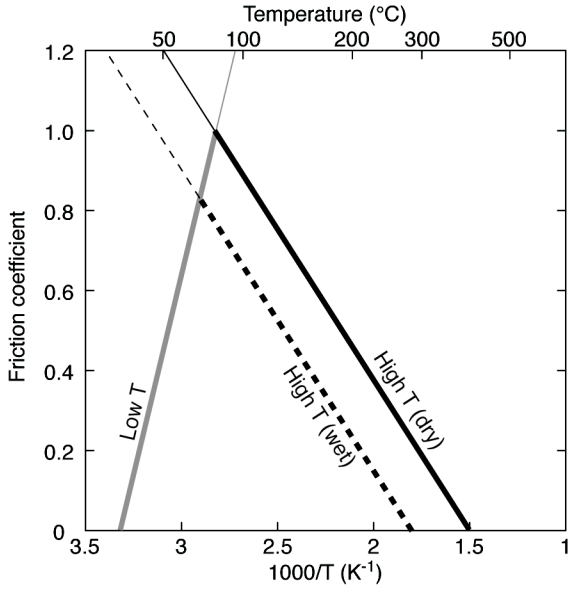

Figure 3.3. Graphical representation of the temperature-dependent friction constitutive relations used in the FEM model for the low- and high-temperature regimes. The same relationship is used for both dry and wet samples in the temperature-strengthening, low temperature regime (gray line). For the temperature-weakening, high-temperature regime, relationships with the same temperature dependence, C, but different base-level of friction, μ^*, are used for dry gouge (solid black line) and wet gouge (dashed black line).

initiation of sliding [e.g., *Dieterich*, 1981]. Accordingly we employ the velocity- and temperature-dependent friction relation determined by *Chester* [1995] for wet quartz at higher velocities as a lower bound to the friction coefficient, given by

$$\mu_{ss} = \mu^* + 0.002 \cdot \ln\left(\frac{V}{1\ [\mu\text{m/s}]}\right) + 21.4\left(\frac{1}{T} - \frac{1}{573\ [\text{K}]}\right). \tag{3.10}$$

However, clay-bearing fault gouge generally displays a smaller friction coefficient than pure quartz gouge, so μ^* is set at 0.44 (0.2 less than for quartz). In detail, use of this particular relation for simulating the high-speed friction results is not critical; adequate behavior is achieved simply by assuming a lower bound to friction at low temperatures set to 0.45. Assuming a lower bound to low-T friction is essentially treating the friction relations given by (3.10) and the low-T mechanism as operating as series-sequential mechanisms.

The formal treatment of thermal pressurization within the sheared gouge layers appears necessary to account for some aspects of the frictional behavior of samples. In particular, the abrupt weakening early in the constant acceleration experiments is produced in the FEM models when thermal pressurization is included. Similarly, in constant velocity experiments, the delay in achieving peak strength in samples sheared at higher slip rates may be explained by thermal pressurization that slows heating and reduces frictional strength.

3.4.2. Localization of slip and heating in the gouge layer

FEM models assuming frictional heating is distributed throughout the gouge layer or concentrated along a surface in the layer were compared for all experiments. Models using a localized heat source produce somewhat smaller torque than models with a distributed heat source, in all cases (Figure 3.4a). It should be noted that microstructural observations indicate the localized slip zones are generally, though not always, located at the boundary between the gouge layer and rotating host block, whereas it is assumed centrally located in the FEM models. In addition, localization generally develops only at larger radii, and may develop early or late in experiments. Thus assuming a localized or distributed heat source is only meant as a first order approximation; however, regardless of the assumption of heat source the FEM models reproduce the general evolution of friction observed in the experiments. All models reported hereafter assume a localized heat source.

3.4.3. Permeability and pore fluid pressurization in the gouge layers

FEM models of the experiments indicate that different assumptions regarding permeability evolution of both gouge layer and host blocks largely impact both constant-velocity experiments and constant-acceleration experiments. The differences are illustrated at a constant V_{eq} of 0.35 m/s or at a constant acceleration of 0.05 m/s^2 (Figure 3.4). The strengthening and weakening observed at constant velocity are best captured when permeability of gabbro is set at 10^{-17} m^2 (Figure 3.4a); however, an assumption of

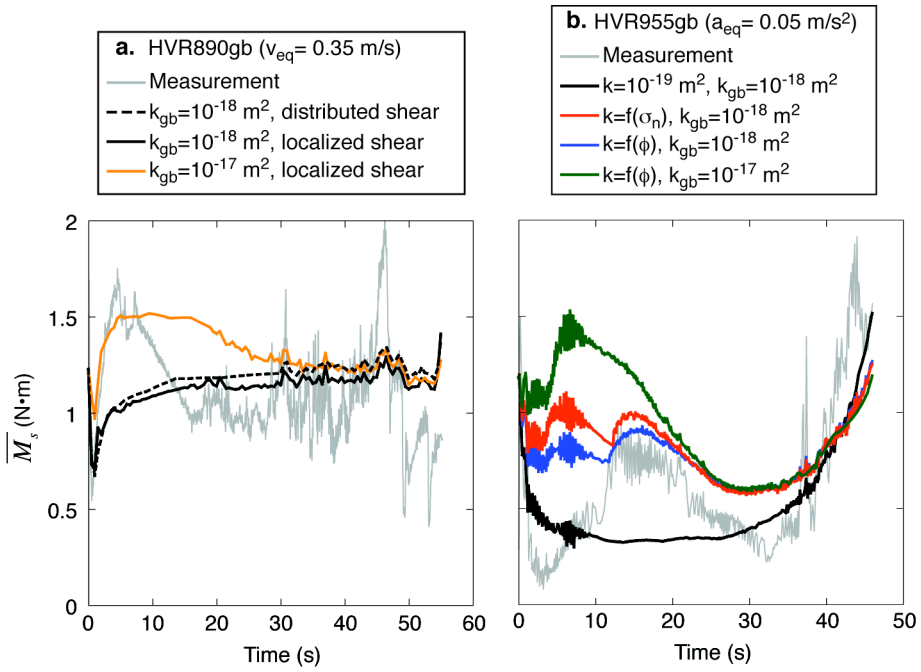

Figure 3.4. Effect of different assumptions for heat source distribution and permeability relationships of gouge and host rock in FEM model simulations. Comparison of measured and model-calculated torque for representative experiments using a) constant velocity loading (HVR809gb, 0.35 m/s) and b) constant acceleration loading (HVR955gb, 0.05 m/s^2). The gray curves indicate the measured torque. k and k_{gb} are permeability of gouge layer and gabbro host rock, respectively. Both a localized heat source and distributed heat source with different values of host block permeability were tested in models of experiment HVR809gb. The models of experiment HVR955gb assumed a localized heat source, but different values of host-block permeability and different assumptions for gouge permeability were tested. Heat generation rate in the gouge is $\tau\dot{\gamma}$ for distributed shear and τV at z=0 for localized shear.

lower permeability of 10^{-18} m^2 for gabbro better simulates the significant weakening in the constant acceleration experiment (Figure 3.4b).

In addition to host block permeability, gouge permeability also affects the results. The general evolution of friction is poorly predicted by the assumption of constant permeability during experiments (Figure 3.4b). In contrast, the assumptions of permeability varying with porosity or normal stress lead to better agreement between models and experiment observation. The findings indicate that permeability somewhat increases with displacement during shear, especially at higher slip rates, such that the abrupt weakening and subsequent increase in torque early in the constant-acceleration tests is successfully reproduced. Overall the observations of all tests are best matched by the assumptions that gouge permeability is dependent on normal stress, gabbro permeability is 10^{-18} m^2, and granite permeability is 10^{-17} m^2; these assumptions are applied in all FEM models presented in the next section.

3.4.4. Spatial and temporal variation of stress, temperature and friction in the gouge layers

The modeling results for all the experiments, which explore different conditions of slip rate, acceleration rate, and water content, are summarized in Figures 3.5-3.8. Model values of gouge torque, coefficient of friction, normal stress, pore pressure, and temperature were calculated at the center of the gouge layer based on the assumptions of a localized heat source and that gouge permeability depends on normal stress. The development of locally elevated pore pressure is expressed by λ, which is the ratio of

Figure 3.5. Results of thermal-, mechanical-, and fluid flow-coupled FEM models for five constant velocity experiments. HVR484gr, HVR809gb, HVR530gr, and HVR482gr are shear experiments on water-dampened gouge at 0.1, 0.35, 0.7, and 1.3 m/s, respectively. HVR475gr is shear experiment on room-dry gouge at 1.3 m/s. (a)-(e) Gouge torque as a function of time. Black and gray lines represent the model-calculated torque and the measured torque, respectively. (f)-(w) Radial distribution of physical properties along the midplane of the gouge layer. Colored lines show conditions at times identified by the arrows with the same colors in figure (a)-(e) and specified in the corresponding legends. (f)-(j) Friction coefficient, μ, (k)-(n) effective friction coefficient, μ', (o)-(r) the ratio of pore pressure to normal stress, λ, and (s)-(w) temperature.

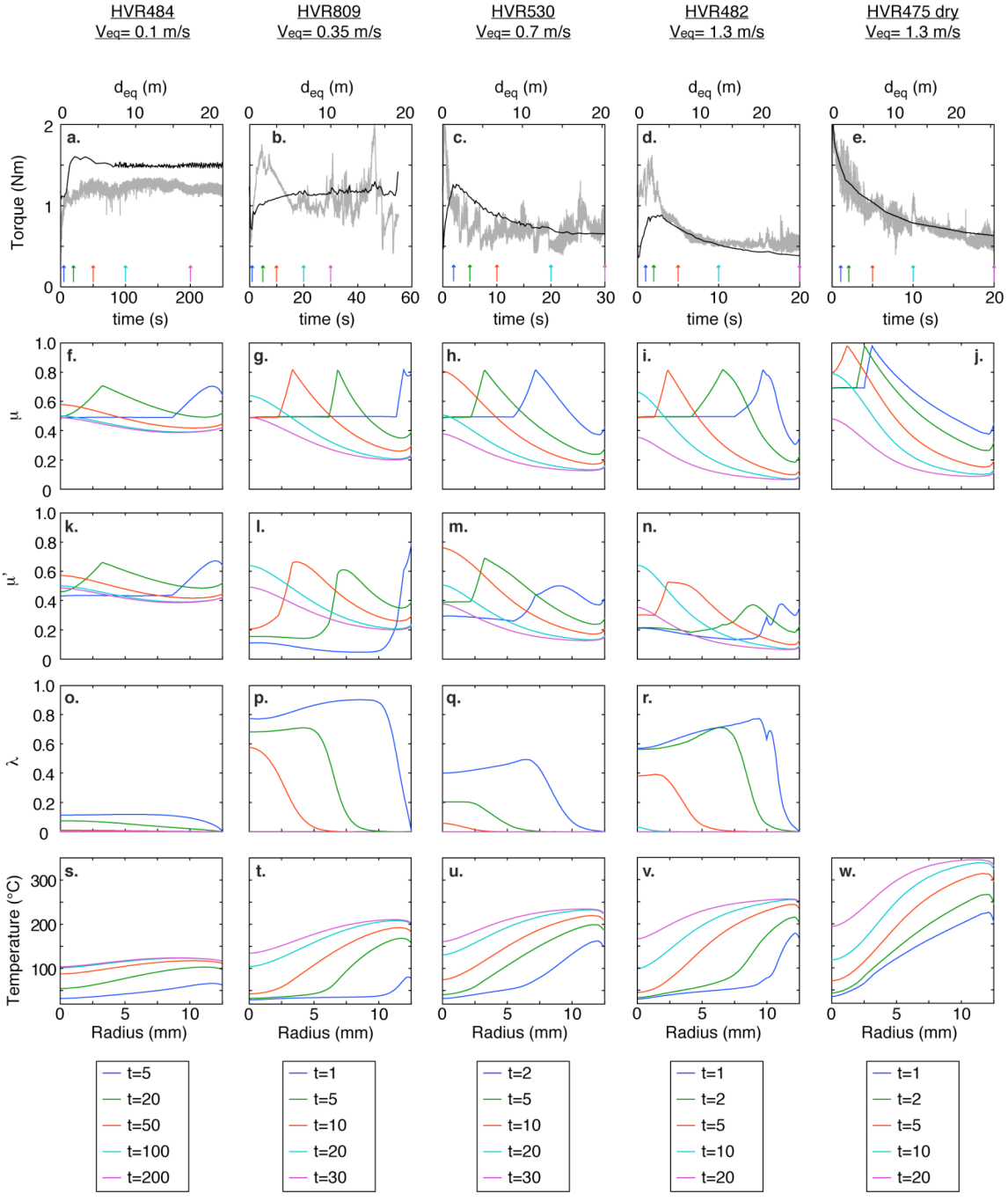
HVR484
Veq= 0.1 m/s
HVR809
Veq= 0.35 m/s
HVR530
Veq= 0.7 m/s
HVR482
Veq= 1.3 m/s
HVR475 dry
Veq= 1.3 m/s
deq (m)
Torque (Nm)
time (s)
μ
μ'
λ
Temperature (°C)
Radius (mm)
t=5
t=20
t=50
t=100
t=200
t=1
t=5
t=10
t=20
t=30
t=2
t=5
t=10
t=20
t=30
t=1
t=2
t=5
t=10
t=20
t=1
t=2
t=5
t=10
t=20

Figure 3.6. Results of thermal-, mechanical-, and fluid flow-coupled FEM models for four constant acceleration experiments. HVR952gb-1 and HVR952gb-2 are two consecutive experiments on the same sample containing water-dampened gouge sheared at a constant acceleration of 0.1 m/s^2. HVR955gb and HVR956gb are shear experiments on water dampened gouge and room-dry gouge, respectively, at a constant acceleration of 0.05 m/s^2. (a)-(d) Torque and equivalent velocity as a function of time. Black and gray solid lines represent the model-calculated torque and the measured torque, respectively. The dashed black lines represent the equivalent velocity. (e)-(r) Radial distribution of physical properties at the center of the gouge layer. Colored lines show conditions at times identified by the arrows with the same colors in figure (a)-(d) and specified in the corresponding legends. (e)-(h) Friction coefficient, μ, (i)-(k) effective friction coefficient, μ', (l)-(n) the ratio of pore pressure to normal stress, λ, and (o)-(r) temperature.

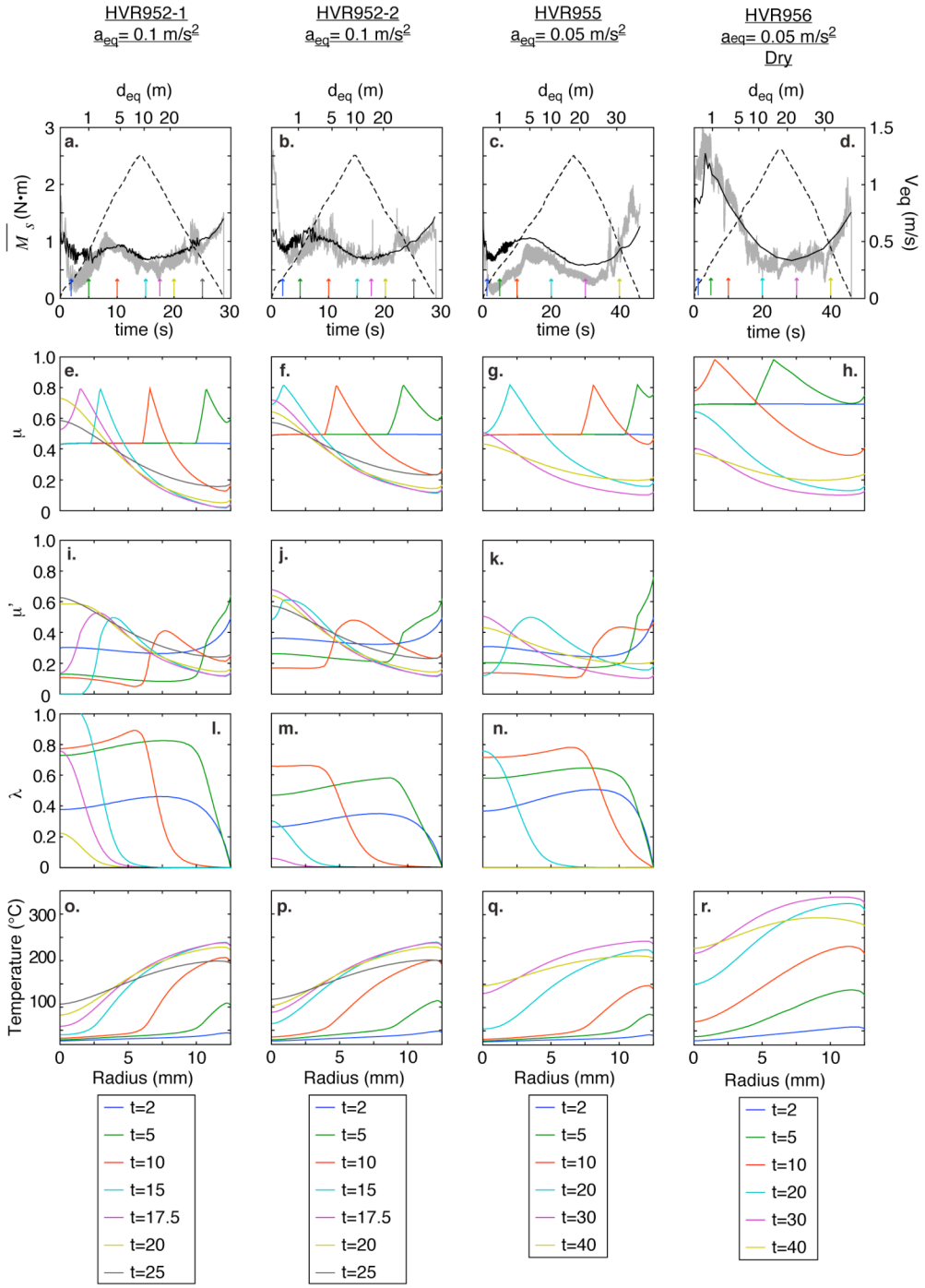
HVR952-1
aeq= 0.1 m/s2
HVR952-2
aeq= 0.1 m/s2
HVR955
aeq= 0.05 m/s2
HVR956
aeq= 0.05 m/s2
Dry
deq (m)
time (s)
Veq (m/s)
μ
μ'
λ
Temperature (°C)
Radius (mm)
t=2
t=5
t=10
t=15
t=17.5
t=20
t=25
t=30
t=40

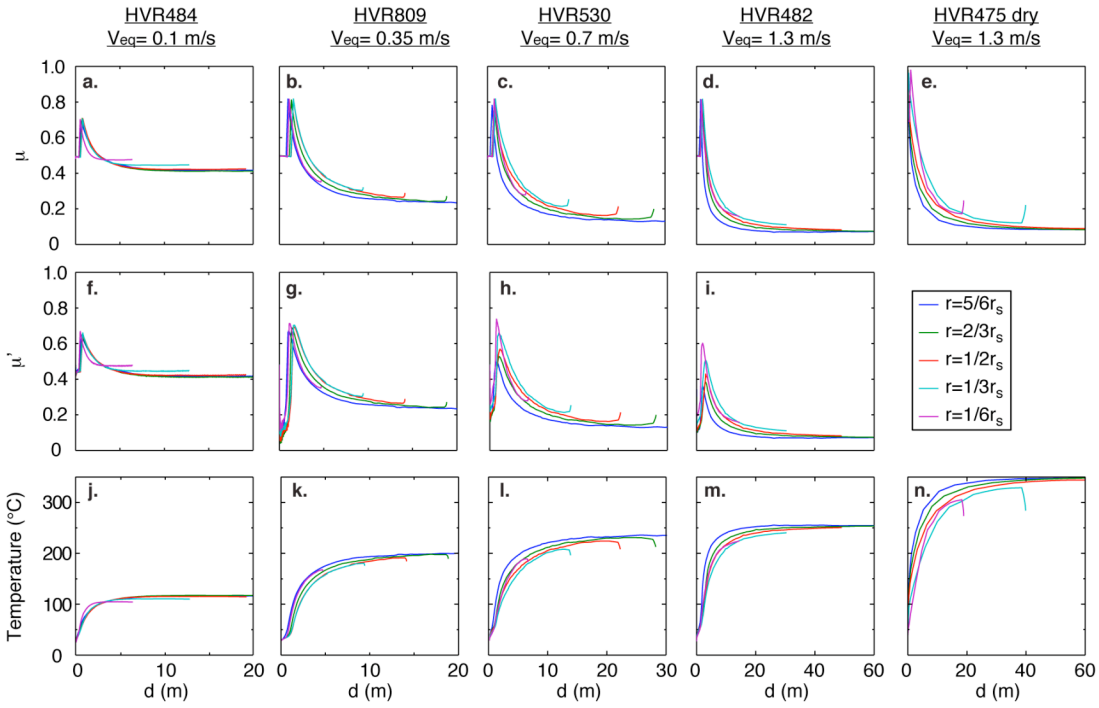

Figure 3.7. Local evolution of (a)-(e) friction coefficient, μ, (f)-(i) effective friction coefficient, μ', and (j)-(n) temperature as a function of local displacement for the constant velocity experiments in Figure 3.5. Colored lines represent conditions at different radii as indicated in the legend.

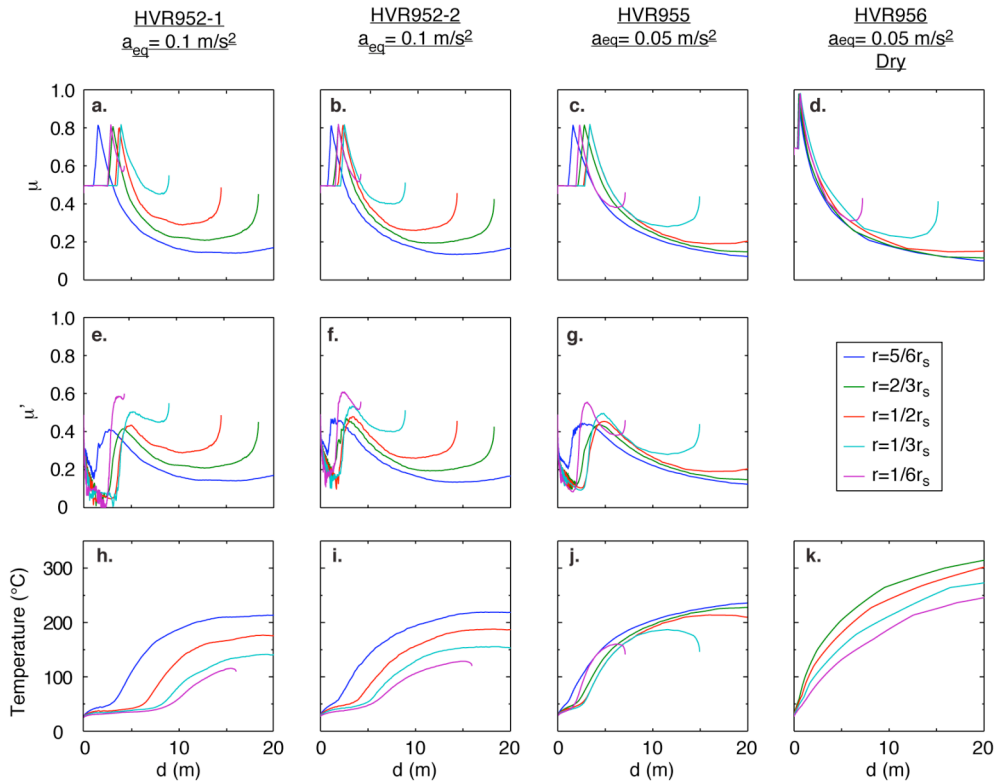

Figure 3.8. Local evolution of (a)-(d) friction coefficient, μ, (e)-(g) effective friction coefficient, μ', and (h)-(k) temperature as a function of local displacement for the constant acceleration experiments in Figure 3.6. Colored lines represent conditions at different radii as indicated in the legend.

pore pressure p to normal stress σ_n, i.e. $\lambda = p/\sigma_n$ [*Hubbert and Ruby*, 1959]. Accordingly, effective coefficient of friction is expressed as $\mu' = (1-\lambda)\mu$.

The model calculated torque shows great agreement with the measurement for all experiments (Figures 3.5a-3.5e and Figures 3.6a-3.6d). Friction coefficient, pore pressure, and temperature in the gouge layer vary with position and time (Figures 3.5f-3.5w and Figures 3.6e-3.6r). In the experiment at the lowest slip rate (HVR484gr), the friction coefficient ranges 0.4-0.7, and there is little development of pore pressure, limited increase in temperature, and no significant weakening (Figures 3.5a, 3.5f, 3.5k, 3.5o, and 3.5s). As slip rates increases, dynamic weakening is enhanced by a combination of temperature-dependent weakening of the friction coefficient and thermal pressurization of pore water. The temperature-dependent friction behavior leads to strengthening followed by weakening as temperature increases with slip. The slip-rate distribution in the sample causes a prominent peak in friction coefficient to form at the perimeter of the gouge layer and migrate inward with time. The peak in friction coefficient is not mimicked by the effective friction coefficient due to locally elevated pore pressure induced by the heterogeneous heating rate (Figures 3.5f-3.5n). The development of pore pressure delays the temperature increase and thus causes a reduction of peak strength (Figures 3.5k-3.5w). Pore water pressure is drained after approximately 10 s, and thermal pressurization is less pronounced in the center of the specimens. Thus after shear to greater slip, the temperature distribution is more homogeneous and a relatively high effective friction coefficient is maintained at the center portion of sample.

The effect of thermal pressurization is most obvious in the constant-acceleration experiments because the heating rate is greater than in the constant, low slip-rate experiments but lower than that in the constant, high slip-rate experiments. In experiment HVR952gb-1 sheared at 0.1 m/s^2, the thermal pressurization rate is much greater than the diffusion rate, thus pore pressure locally exceeds normal stress (Figure 3.6l). For the second run of HVR952gb (HVR952gb-2), the assumption that fluid source is 50 % as much as that of the first run (HVR952gb-1) results in reasonable match between the measured torque and the calculated torque, which suggests that after the first run the sample is partially wet.

An interesting characteristic of the constant velocity tests is that the increase in local temperature with local slip is nearly the same at all radii (Figure 3.7). Accordingly, the evolution of friction coefficient with local slip also is similar at all radii. Although the friction versus displacement curves have the character of slip-dependent weakening, the model analysis indicates that the samples rapidly achieve a relatively steady-state temperature and friction condition as a result of the feedback between frictional heating and temperature-weakening friction (Figure 3.7). In contrast, for the constant-acceleration experiments, the evolution of local temperature with local displacement varies with radius, and the friction versus local slip curves are dissimilar (Figure 3.8).

3.5. Discussion

3.5.1. Temperature-dependent friction constitutive relations and thermal pressurization

The FEM models treat the processes operative in the experiments simply, and several aspects are not treated formally, such as plastic deformation, velocity dependence of friction, and the thermal pressurization of vapor and associated two-phase fluid flow of liquid water and vapor. However, the critical fluid pressure and temperature condition for vaporization is tracked, and the magnitude of thermal fluid pressurization is diminished at the critical condition for the phase change as a means to account for vaporization and the likely rapid escape of vapor from the sample. There are other poorly constrained physical properties, such as the ability of the Teflon sleeve to confine pore pressure, and the evolution of permeability of both gouge layer and host rocks with slip. We believe the gouge permeability is the most important, unknown factor of the FEM models. In spite of the uncertainties, it appears that the range of behavior displayed by the experiments is captured by the FEM model, which is based primarily on 1) a simple temperature-dependent friction constitutive relation and 2) ability to treat fluid pressurization, fluid flow, and the change at the critical conditions for vaporization. Although the FEM model is not a unique explanation for the behavior, the fact that the response of the samples to very different load paths can be simulated with the model gives credence to the friction constitutive relationship. In addition, the need to include fluid pressure and fluid flow in order to explain the differences in behavior for wet and

dry tests supports the inference that thermal pressurization occurs in the gouge at high slip rates.

The temperature-dependence of friction in the constitutive model, characterized by the parameter C in equations (3.3), (3.5) and (3.9), is very large in magnitude for both the temperature-strengthening and temperature-weakening regimes. The magnitudes are 50-100 times greater than those determined at low rates of slip for wet quartz gouge using slide-hold-slide, velocity stepping, and temperature stepping experiments [*Chester and Higgs*, 1992; *Chester*, 1994, 1995]. As indicated in (3.3), temperature dependence is a function of the activation energy, Q_A and Q_B, and the velocity dependence of friction, A-B. Although velocity dependence was not determined for the gouge, results from other recent experimental studies of friction [e.g., *Di Toro et al*., 2004; *Lockner and Reches*, 2009] on silicates at intermediate slip-rates (0.001 to 0.1 m/s) indicate large-magnitude rate-weakening behavior. This velocity range extends up to the minimum velocities tested herein where temperature-strengthening is observed. Both *Di Toro et al*. [2004] and *Lockner and Reches* [2009] report velocity-weakening with A-$B \approx$ -0.1. Assuming this value is appropriate for the temperature-strengthening regime where C = -2000 K gives an activation energy $Q = Q_A = Q_B$ on the order of 165 kJ/mol·K, which is not an unreasonable value. Interestingly, *Lockner and Reches* [2009] not only observe a regime of velocity weakening between 0.001 and 0.04 m/s, but find marked strengthening between 0.04 and 0.3 m/s coincident with a temperature increase associated with frictional heating. The strengthening above 0.04 m/s is quite similar to the temperature-strengthening in the low-T regime identified here. It is possible that the behavior

documented by *Lockner and Reches* [2009] reflects a single mechanism for which the velocity dependence dominates behavior below 0.04 m/s where frictional heating is minimal, and temperature strengthening dominates at higher velocity where heating rates and temperature increases are substantial. In fact, the entire spectrum of steady-state frictional behavior documented by *Di Toro et al.* [2004], *Lockner and Reches* [2009], and in the low-T regime here, could be described approximately with a single rate- and temperature-dependent friction-constitutive relation of the form of (3.3) using $A\text{-}B$ = -0.1, $Q = Q_A = Q_B$ = 165 kJ/mol·K, μ^* = 1.0, T^* = 353 K, and V^* = 2 m/s. In fact, we find that using this velocity and temperature dependent relation for the low-T regime in the FEM model can not only describe all the experiment results herein, but also obviates the need for assuming (3.10) or some other lower bound to friction.

3.5.2. Relating microstructure, friction mechanisms, and constitutive behavior

Kitajima et al., [2010] documented the microstructure evolution of the gouge sheared in constant-velocity experiments by mapping the microstructure of layers in sequential displacement tests. Four deformation units are observed; slightly sheared starting material (Unit 1) and a strongly sheared and foliated gouge (Unit 2) are produced when frictional heating is less significant. A random fabric gouge with rounded prophyroclasts (Unit 3) and an extremely-fine, microfoliated layer (Unit 4) develop when significant frictional heating occurs. The development of each unit was quantified as a function of local velocity and local displacement to show that Unit 3 and Unit 4 are formed at higher slip rates and larger displacements [*Kitajima et al.*, 2010].

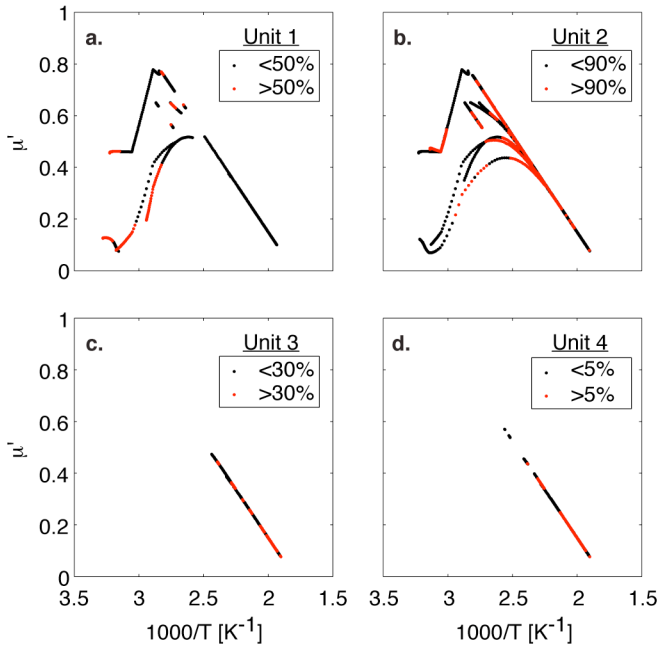

Figure 3.9. Diagrams showing the relationship between the formation of the four gouge units, friction coefficient, and temperature. The volume fraction of (a) Unit 1, (b) Unit 2, (c) Unit 3, and (d) Unit 4 are shown by color on plots of local friction coefficient versus local temperature. Red and black colors represent more and less development of each unit, respectively. The volume fraction of each unit was measured by point-counting radial-cut petrographic sections [*Kitajima et al.,* 2010]. The data include all constant velocity experiments on wet samples analyzed in *Kitajima et al.* [2010]. Friction coefficient and temperature are the model-calculated values at the midplane of the gouge layer. Unit 3 and Unit 4 are formed only in temperature-weakening, high-temperature regime.

The results of the FEM model can be used to infer the relationship between local friction coefficient, local temperature, and friction mechanism as recorded by the microstructure of each unit. Unit 1 develops in the temperature strengthening regime at low temperature (Figure 3.9a), and Unit 2 is present in transition from temperature strengthening to temperature weakening over a wide range of temperature and friction coefficient (Figure 3.9b). On the other hand, both Unit 3 and Unit 4 are present only in temperature weakening regime at high temperature (Figures 3.9c and 3.9d).

Unit 2 expands at the expense of Unit 1 both outward and inward with displacement *Kitajima et al.* [2010]. To some extent the outward expansion of Unit 2 and the preservation of Unit 1 at the periphery of the gouge layer reflects the corner effect of the gouge-rock-jacket interface inherent in the rotary shear experiment configurations [*Beeler et al.*, 1996], and thus should not be considered when trying to understand microstructure development. On the other hand, the inward expansion of Unit 2 with displacement (or time) is found to coincide with the inward migration of the thermal front shown by the FEM modeling, and with conversion of Unit 1 to Unit 2 as frictional strength increases with temperature and shear strain.

Unit 3 and Unit 4 develop only at temperature higher than 120 °C, and both units correlate with low coefficients of friction resulting from temperature weakening. Interestingly, the FEM models indicate excess pore fluid pressure is not generated in the areas of the gouge layer where Unit 3 and Unit 4 are forming because all the free water has transformed to vapor. However, the FEM model does not treat pressurization of water vapor associated with the transition from liquid water because it is assumed that

the vapor can be easily pass through the gouge layer past the Teflon sleeve. In contrast, *Boutareaud et al.* [2008, 2010] assume vapor does not easily escape and that the vaporization increases pore pressure causing the gouge to dilate and fluidize. They interpret that clay-clast aggregates (CCA) are formed as a consequence of vapor fluidization that allows fine clay particles to aggregate and adhere to core particles of the CCA. It is unclear whether vaporization can cause thermal pressurization due to lack of information on hydraulic diffusivity of water vapor during shear [see also *Mizoguchi et al*., 2009]. However, we find that Unit 3 containing CCA is observed more frequently in room-dry samples than in wet samples sheared at otherwise identical conditions. A similar finding is reported for high-speed, constant velocity experiments on clay-bearing fault gouge from the Nankai Trough (personal communication, K. Ujiie, 2010). If CCA are a product of thermal pressurization of water vapor, then CCA should be more prevalent in experiments with wet gouge. Accordingly, the vaporization and thermal pressurization of vapor appears very limited both spatially and temporally, and has little significance to bulk mechanical response.

A previous study of friction experiments on illite-rich gouge sheared at low slip rates of 0.048 and 4.8 μm/s and temperature of 200-600 °C documented two different deformation structures associated with different frictional behavior [*Moore et al.*, 1989]. A pervasively deformed structure including clay-foliation, kink bands, and stretched opaque grains is formed in samples which are sheared at relatively lower temperature and mostly show stable slip, which implies rate strengthening. The other structure is characterized by localized shear bands within undeformed regions of clay aggregates,

and is formed in samples that are sheared at relatively higher temperature and show stick-slip behavior slip, which implies rate weakening. Although the absolute temperature ranges and slip velocities are different from the high-speed tests herein, the similarities in terms of relating frictional behavior, structural features, and temperature conditions between the low slip-rate and high slip-rate tests support the hypothesis that pervasive deformation occurs when velocity- or temperature-strengthening is dominating bulk behavior and that localized slip occurs when velocity- or temperature-weakening is dominating bulk behavior.

Kitajima et al. [2010] concluded that the dynamic weakening (in the high-T regime) appears to require both the establishment of the localized slip surface recorded by Unit 4, and a slip velocity sufficient to elevate temperature along the surface through frictional heating. These are the conditions that generally favor a dynamic weakening by the flash heating mechanism [*Rice*, 2006; *Beeler et al.*, 2008; *Noda*, 2008]. Although we have described the weakening in the high-T regime based only on the macroscopic temperature. Flash heating is a weakening mechanism that causes a decrease in shear stress at an asperity contact as a consequence of increasing the local temperature at the contact [*Rice*, 1999, 2006, *Beeler et al.*, 2008]. For flash heating, the steady-state frictional strength is given by

$$\mu = \left(\mu_0 - \mu_w\right)\frac{V_w}{V} + \mu_w \qquad (V > V_w)\,, \tag{3.13}$$

where μ_0 is low speed friction coefficient, μ_w is weakened friction coefficient at high temperature, and V_w is critical slip velocity above which the contact weakens during contact lifetime. V_w is obtained by

$$V_w = \frac{\pi \alpha_{th}}{D_a}\left(\frac{\rho c (T_w - T)}{\tau_c}\right)^2, \tag{3.14}$$

where D_a, T_w, τ_c and α_{th} are slip distance during the lifetime of an asperity, a weakening temperature, local shear stress, and thermal diffusivity ($= K/(\rho c)$), respectively. Steady-state coefficient of friction determined from the FEM model decreases with representative velocity in a manner that appears consistent with the flash heating model (Figure 3.10). The critical slip velocity V_w is estimated as 0.19 m/s, which is consistent with the value calculated for an experiment at room temperature, T=20°C from (3.14) with α_{th}= 0.5 mm^2/s, ρc= 2.7MPa/°C , D_a= 5μm , T_w= 900°C , and τ_c= 3.0GPa [*Rice*, 2006]. Description of flash heating as formulated in (3.13) and (3.14) involves specifying a number of material and structural parameters in addition to the state variables of T and V. However, experiment results and theoretical analysis suggest that localization of slip and particle refinement naturally arises in gouge layers at high slip rates [e.g., *Noda et al.*, 2009; *Sleep*, 2010]. Presumably, after additional work, an understanding of the microscopic processes of slip can be integrated with a macroscopic viewpoint as employed here to describe the constitutive behavior at high slip rates using a compact rate- and state-variable law that incorporates an appropriate evolution function to describe changes in structural state.

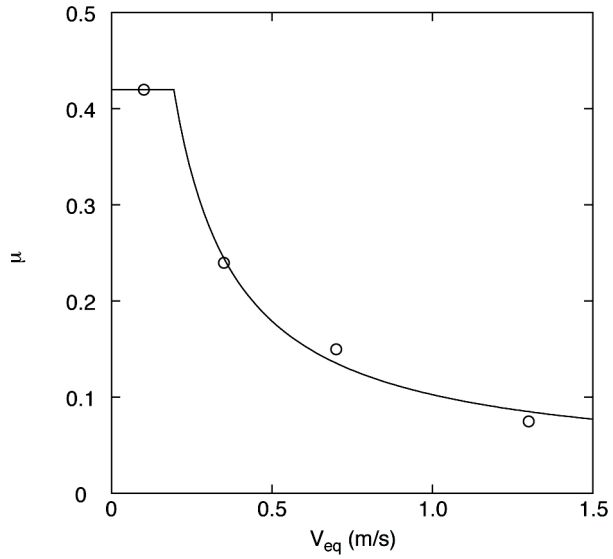

Figure 3.10. Plot showing steady-state friction coefficient as a function of representative velocity. Open circles are model-calculated values of friction at steady-state for the four constant velocity tests on wet gouge layers. The fitting curve is based on the flash heating model using material and structural parameters specified in the text.

The critical slip distance for describing evolution of friction at slow slip rates is interpreted as a distance required to renew the population of true contacts [*Dieterich*, 1978] and has a range of 1-100 μm depending on surface roughness, particle size, slip rate, normal stress, and thickness of gouge [e.g., *Dieterich*, 1981; *Marone and Kilgore*, 1993; *Mair and Marone*, 1999]. From the FEM analysis of the experiment results reported here, the critical slip distance for dynamic weakening illustrated in plots of local friction coefficient versus local displacement, is approximately 10 m or less. Because the micromechanisms for dynamic weakening are likely different than the weakening in quasi-static slip, the critical distance for dynamic weakening should be understood as a distance required to reach a steady-state condition of temperature along a localized slip zone, rather than just a change in true contact population.

In the context of the rate and state friction, velocity weakening is a necessary condition for nucleation of instability, but dynamic rupture could be maintained with velocity strengthening friction if frictional heating causes weakening through thermal processes such as pore fluid pressurization or flash heating [e.g., *Noda et al., 2009*]. There has been extensive laboratory work on friction constitutive behavior at low to intermediate slip rates. Although there is great variability in the sign of velocity dependence with rock types and conditions of deformation, a general finding is that velocity-weakening occurs over a limited range of temperature and velocity with transitions to velocity strengthening at very low rates and elevated temperatures or at high slip rates [e.g., *Blanpied et al.*, 1995; *Chester*, 1995]. In some cases the transitions

in velocity dependence can be associated with changes in the microscopic mechanisms of frictional slip.

An important concern is the transition in friction behavior from intermediate rates to the high rates where dynamic weakening processes dominate. As discussed by *Shimamoto and Hirose* [2005] and *Sone and Shimamoto* [2009], strengthening process at this transition can serve as a mechanical barrier to the development of large earthquakes. Unfortunately, there is very little experimental data for fault friction in the transition regime on materials at conditions of elevated temperature and fluid pressure. Some strengthening has been inferred from the extrapolation of velocity strengthening observed in friction experiments at low slip rates [e.g., *Shimamoto*, 1986], and now has observed in many high-speed experiments, including those herein [*Tsutsumi and Shimamoto*, 1997; *Shimamoto and Hirose*, 2005; *Sone and Shimamoto*, 2009; *Lockner and Reches*, 2009]. Most studies assume the strengthening reflects velocity- or slip-dependent strengthening [*Sone and Shimamoto*, 2009]. In contrast, we argue that strengthening could reflect frictional heating and the temperature dependence of friction within velocity-weakening regime. *Noda* [2008] also argue for the importance of considering temperature-dependence of friction in the intermediate slip-rate regime. Clearly there is a need to acquire additional observations of rate and temperature dependence of friction in the intermediate slip-rate regime in addition to understanding various dynamic weakening processes that dominate at coseismic slip rates.

3.6. Conclusions

1) Temperature-dependent friction constitutive relations, in which friction coefficient is proportional to 1/T, successfully describe friction of gouge in rotary shear at coseismic slip rates between 0.1 and 1.3 m/s. Friction coefficient increases with temperature (temperature-strengthening) at low temperature conditions (less than approximately 70 ˚C) and decreases with temperature (temperature-weakening) at higher temperature conditions. Assuming an Arrhenius relationship between slip rate and temperature, the temperature-strengthening behavior documented in low-temperature, high-speed tests is consistent with other recent findings of dramatic rate-weakening at low temperature and intermediate slip rates (0.001 to 0.1 m/s).

2) Thermal-, mechanical-, and fluid-flow-coupled FEM models based on a temperature-dependent friction constitutive relation, and that treat thermal pressurization of pore water, successfully reproduce the frictional response in all shear experiments at different conditions of slip rate, acceleration rate, and water content. The greatest uncertainty in the model derives from the lack of independent information on the evolution of gouge permeability at high shear rates,

3) The friction coefficient, normal stress, pore pressure, and temperature within the gouge layers vary with position (radius) and time, and largely depend on the frictional heating rate. Thermal pressurization of pore fluid develops during the early stages of experiments at locations where heating rate is large, and at the transition from the low-temperature, strengthening regime to the high-temperature, dynamic-weakening regime.

4) Microstructure of the sheared gouge layers record a general evolution from distributed shearing flow to fluidized flow associated with the formation of an extremely localized slip zone as slip-rate and temperature is increased. The critical displacement for dynamic weakening results in approximately 10 m or less, and can be understood as the distance required to form a localized slip zone and achieve a steady-state temperature condition. The observed relationship between steady state friction and slip rate is consistent with predictions from micromechanical models of flash heating.

5) Further investigations on the frictional behavior at intermediate and high slip velocities are required to fully establish rate-, state-, and temperature-dependent friction constitutive relations for seismic slip rates.

4. MECHANICAL AND HYDRAULIC PROPERTIES OF SUBDUCTED SEDIMENTS, NANKAI TROUGH ACCRETIONARY PRISM: EFFECT OF STRESS PATH

4.1. Introduction

Recurrent devastating thrust-type earthquakes and tsunamis occur in subduction zones, where mechanical and chemical processes operate, including sedimentation, deformation, metamorphism, fluid-flow, dissolution, cementation, and solute transport. One of the key outstanding questions for these regions is what controls tsunami- and seismo-genesis. The updip limit is especially important for tsunami generation and corresponds to a critical temperature of 100-150 °C [e.g., *Hyndman and Wang*, 1993; *Hyndman et al.*, 1995]. The transformation of smectite to illite at that temperature could change the frictional behavior from velocity strengthening to velocity weakening and explain the up-dip seismogenic limit [*Vrolijk*, 1990]. However, this simple hypothesis is not supported by friction experiments on illite and other clay-bearing materials [*Saffer and Marone*, 2003, *Brown et al.*, 2003]. The aseismic-seismic transition is likely not controlled by a single process, but depends on many factors including consolidation characteristics of sediments, cementation processes, dehydration reactions accompanied by solid-fluid phase transitions such as smectite-illite and opal A-quartz, pore pressure generation, fracture permeability, and thermal gradient [e.g., *Byrne et al.*, 1988; *Marone and Scholz*, 1988; *Moore and Vrolijk*, 1992; *Moore and Saffer*, 2001].

The stress conditions in accretionary subduction zones are complicated; yet they are essential to describe both brittle and ductile deformation in sediments [e.g., *Moore*, 1986]. Stress states change spatially and temporally during burial, underthrusting, underplating, and exhumation, and different deformation mechanisms are apparently operative. Since fluid pressurization and flow plays one of the more important roles in deformation of sediemnts, it is necessary to address the effect of deformation on hydraulic properties. *Zhu and Wang* [1997] reported that permeability evolution of porous rocks depends on the deformation mechanism; slight decrease in permeability is observed with increasing porosity in brittle faulting regime, while significant reduction in permeability with decreasing porosity in cataclastic flow regime. Most laboratory studies have measured the permeability evolution during the conventional triaxial deformation tests at the constant Pc and only few studies discuss the effect of stress states or stress history. *Crawford and Yale* [2002] measured permeability of siliciclastic and carbonate rocks along different stress paths and found that permeability evolution largely depends on rock types and deformation micromechanics, and that critical state theory can account for permeability evolution of siliciclastic rocks but not for that of carbonate rocks. *Zhu et al.* [2002] introduced hybrid compression tests on porous sandstones to understand the shear-induced permeability anisotropy, and found that permeability anisotropy develops with the onset of shear-enhanced compaction and initiation of cataclastic flow, but it diminishes at a cumulative strain of ~10%. For the sediments, the consolidation state at the onset of shear is a crucial factor on the permeability evolution as well as on deformation style [e.g., *Karig*, 1990; *Bolton et al.*,

1998]. Apparently, to better describe the evolution of hydraulic and mechanical properties with deformation is crucial for the modeling of the coupled deformation and fluid flow processes in accretionary subduction zones.

The purpose of this paper is to present the evolution of strength and hydraulic properties along different stress paths, which simulate the range of stress conditions in accretionary subduction systems. First, we describe five experiments along different stress paths on the three different samples from the Nankai accretionary subduction zone collected during the IODP NanTroSEIZE Stage 1 Expeditions. Second, from the experimental results, we construct yield surfaces based on the critical state theory to estimate in-situ stress states and mechanical properties including undrained shear strength, unconfined compressive strength, and frictional angle. Third, we discuss the effect of deformation on hydraulic properties in terms of stress state and history.

4.2. Critical State Soil Mechanics Theory

The oil mechanics critical state concept is very useful to understand the stress states and stress history for deformation of marine sediments and porous sedimentary rocks. The critical state is defined as the state where plastic deformation can occur without producing any change in strength and volume [*Roscoe et al.*, 1958]. Critical state is described from the three-dimensional relationship of effective mean stress, p', differential stress, q, and specific volume (volumetric strain); however, two-dimensional p'-q space often is used to describe the stress states in nature and experiments (Figure 4.1a). Herein, we use an axial-symmetric stress and strain model, and define p' and q by

$$p' = \frac{\sigma_1 + 2\sigma_3}{3} - P_p \tag{4.1}$$

$$q = \sigma_1 - \sigma_3 \tag{4.2}$$

where σ_1 and σ_3 are the maximum and minumum principal compressive stresses, respectively, and compressive stress and shortening strain are taken as positive. This model is often assumed for sediment in nature, and accurately describes the stress states in our triaxial experiments. The critical state is represented as a straight line in p'-q space, and the yield surface is described by the slope of the critical state line, M, and a reference effective mean pressure, p_0'. The yield surface is expressed by either a logarithmic function of p' (Original Cam-Clay) or by an elliptic shape (Modified Cam-Clay) [e.g., *Wood*, 1990].

$$q = Mp' \qquad \text{(Critical state)} \tag{4.3}$$

$$q + Mp' \ln\left(\frac{p'}{p_o'}\right) = 0 \qquad \text{(Original Cam-Clay yield surface)} \tag{4.4}$$

$$\frac{q^2}{p'^2} + M^2\left(1 - \frac{p_o'}{p'}\right) = 0 \qquad \text{(Modified Cam-Clay yield surface)} \tag{4.5}$$

In the Cam-Clay or the Modified Cam-Clay models, the yield surface is the same as the plastic potential, which is orthogonal to the plastic strain vector (Figure 4.1a). The plastic strain vector consists of two components, a plastic volumetric strain, ε_p^p and a plastic shear strain, ε_q^p. Volumetric strain ε_p and shear strain ε_q are expressed by

$$\varepsilon_p = \varepsilon_a + 2\varepsilon_r \tag{4.6}$$

$$\varepsilon_q = \frac{2}{3}(\varepsilon_a - \varepsilon_r) \tag{4.7}$$

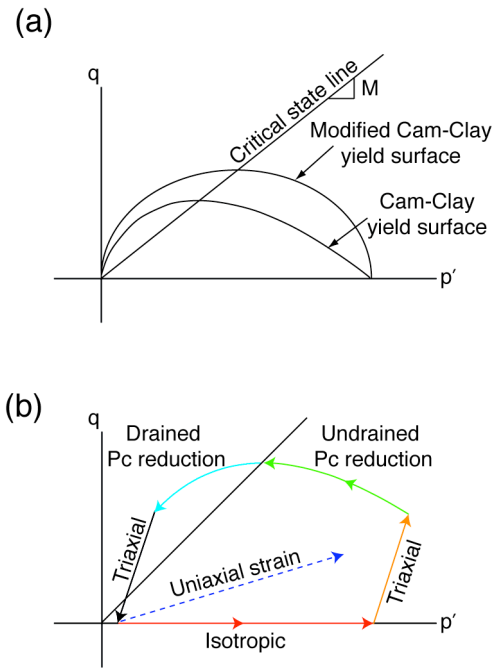

Figure 4.1. Schematic diagram of critical state soil mechanics and stress paths in p'-q diagram. (a) Critical state line and two yield surfaces of the original Cam-Clay model and the modified Cam-Clay model. The slope of critical state line is M. (b) Six different stress paths are achieved in the experiments, isotropic loading (and unloading), triaxial loading at constant Pc, uniaxial strain loading, undrained Pc reduction, drained Pc reduction, and triaxial unloading at constant Pc.

where ε_a and ε_r are axial strain and radial strain. From Hooks law, the elastic volumetric strain ε_p^e and elastic shear strain ε_q^e are linearly related to effective mean stress and differential stress;

$$\begin{bmatrix} \delta\varepsilon_p^e \\ \delta\varepsilon_q^e \end{bmatrix} = \begin{bmatrix} 1/K' & 0 \\ 0 & 1/3G' \end{bmatrix} \begin{bmatrix} \delta p' \\ \delta q \end{bmatrix} \tag{4.8}$$

where K' and G' are bulk modulus and shear modulus in terms of effective stress.

Sediments and sedimentary rocks have potential to record the maximum effective stress state in the past loading history. It is called preconsolidation stress, σ_{v0}', and can be estimated in consolidation tests. The ratio of preconsolidation stress to the present in-situ effective vertical stress is called overconsolidation ratio, $OCR = \sigma_{v0}'/\sigma_v'$. If OCR =1, sediments are normal consolidated. If OCR >1, sediments are overconsolidated. If OCR <1, sediments are underconsolidation. We need to be careful to use the term 'underconsolidation', which is originated in geology and not used in engineering [*Jones*, 1994]. Underconsolidation state can be achieved only when pore pressure has been greater than hydrostatic pore pressure and the normal consolidation state has never been reached in history, and thus inhibits less consolidation. On the other hand, if excess pore pressure develops when sediments are normal consolidated, then the sediments are just overconsolidated due to reduction in effective stress. Thus, the development of excess pore pressure can render sediments underconsolidated or overconsolidated, but their mechanical behavior is totally different; the former is weak and ductile and the latter is brittle [e.g., *Jones*, 1994].

4.3. Geological Settings and Experimental Samples

The Nankai Trough is located southwest of Japan, where the Philippine Sea plate is subducting beneath the Eurasian plate at a rate of 4-6 cm/year (Figure 4.2a) [*Seno et al.*, 1993; *Miyazaki and Heki*, 2001]. The Integrated Ocean Drilling Program's (IODP) Nankai Trough Seismogenic Zone Experiment (NanTroSEIZE) focuses on direct sampling, in-situ measurement, and long-term monitoring at the region off the Kii Peninsula through multiple stages each comprised of multiple drilling expeditions, in order to understand the mechanics of seismogenesis and rupture propagation along plate boundary faults. During Stage 1 Expeditions 314, 315, and 316, logging data and core samples were successfully obtained from the eight sites (Figure 4.2b) [*Tobin et al.*, 2009a]. The three different samples presented in this paper were collected from the three major regions of NanTroSEIZE transect, the Kumano forearc basin, the shallow tip of the megasplay fault, and the frontal thrust region (Table 4.1). The sample 315-C0002B-63R-1 is Late Miocene, old accretionary prism siltstone taken from 1034 m core depth sea floor (CSF) in forearc basin region [*Expedition 315 Scientists*, 2009]. The age is estimated between 5.59 and 5.90 Ma, and the most likely depositional environment before accretion is trench wedge although this interpretation is difficult due to poor core recovery and strong tectonic overprint [*Expedition 315 Scientists*, 2009]. The sample 316-C0004D-48R-1 is early Pleistocene(~1.67 Ma), slope sediment taken from 360 m CSF at the footwall of megasplay fault [*Expedition 316 Scientists*, 2009a]. The burial

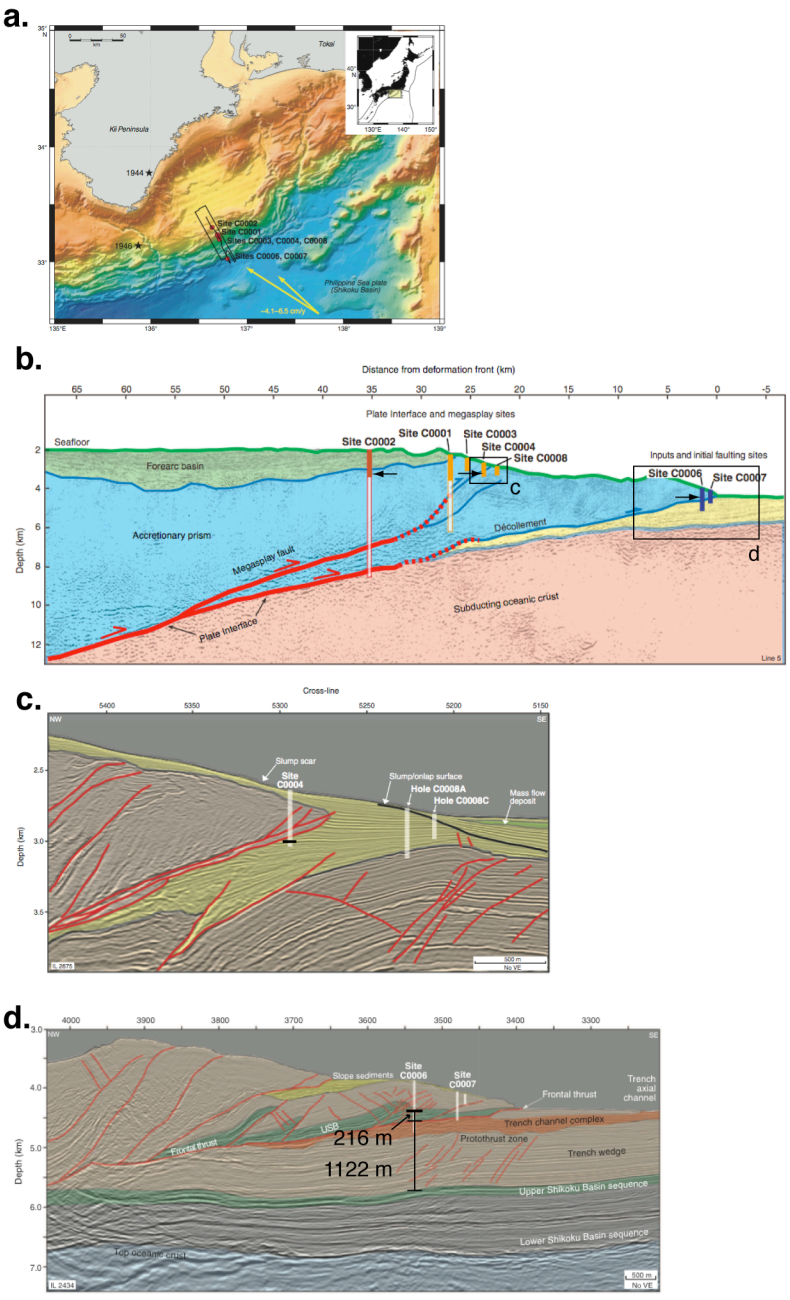

Figure 4.2. Geological setting of the Nankai Trough subduction zone. (a) A map view and (b) a cross-section view of the transect of IODP NantroSEIZE projects off Kii Peninsula. Sites C0002, C0004, and C0006 are located in forearc basin, megasplay, and frontal thrust regions, respectively. The black box areas are enlarged in (c) and (d). (c) and (d) Detailed cross section of the megasplay and frontal thrust regions.

Table 4.1. Summary of experimental samples. CSF is core depth below sea floor, and LSF is LWD(logging-while-drilling) depth below sea floor.

Experimental samples/	CSF (mbsf)	Sample diameter (mm)	Sample length (mm)	Estimated porosity (%)	In situ effective overburden pressure σ_v' (MPa)	Hydrostatic pore pressure (MPa)	LSF (mbsf)	Breakout width θ_b (°)
315-2B-63R-1	1034	19.2	24.6	35	8.8	29.8	996	86
316-4D-48R-1	360	19.3	18.7	43	2.7	30.0	352	60
316-6F-8R-1-a	457	19.2	27.1	40	4.4	43.5	462	39
316-6F-8R-1-b	457	19.0	32.3	40	4.4	43.5	462	39
316-6F-8R-1-c	457	19.2	11.3	40	4.4	43.5	462	39

depth of the sample 316-C0004D-48R-1 before underthrusting is inferred as at least ~52 m, which is the present thickness of overriding slope sediment above the sample underthrusted below the megasplay (Figure 4.2c), however, it is the minimum estimation based on the assumption that all slope sediments deposited have been underthrusted below the megasplay and also that no further compaction is made after underthrsting. The sample 316-C0006F-8R-1 is Pliocene-Pleistocene Upper Shikoku Basin (USB) siltstone taken from 457 m CSF at the hanging wall of the main frontal thrust [*Expedition 316 Scientists*, 2009b]. The seismic reflection data and observations of core samples imply that the USB sediment and the overriding slope sediment were deposited off the deformation front, underthrusted and underplated below the previous frontal thrust, and overthrusted along the present frontal thrust. The burial depth of the sample 316-C0006F-8R-1 is estimated as ~430 m from the total thickness of overriding USB sediment and slope sediment, since the most top unit of slope sediment is deposited during the uplift due to movement of the frontal thrust [*Expedition 316 Scientists*, 2009b ; *Screaton et al.*, 2009]. The total displacement of the present frontal thrust is estimated as long as 6 km [*Moore et al.*, 2009], but such large amount of displacement is distributed among multiple faults in the frontal thrust regions, as they are observed at both Site C0006 and Site C0007, which is located ~700 m seaward from Site C0006 [*Screaton et al.*, 2009].

4.4. Experimental Method

Experimental samples were trimmed from the whole-round core samples (~75 mm diameter) to a diameter of 20 mm and a length of 20-40 mm; in all cases the cylindrical axis is parallel to the axis of whole-round sample (Table 4.1). All experiments were conducted using a modified variable strain-rate triaxial deformation apparatus (Figure 4.3a), MVSR [*Heard*, 1963; *Chester*, 1989]. The gear-driven axial load is applied at a constant axial displacement rate of 5×10^{-6} mm/s, which is equivalent to the strain rate of $\sim10^{-7}$ s^{-1}. This is the slowest rate that can be used in this apparatus.

All experiments were conducted at room temperature conditions. A screw-driven, piston cylinder pressure generator and pressure transducer is placed in the pore pressure system, and used to (1) keep pore pressure constant and (2) measure pore volume change, and (3) conduct pulse-decay permeability measurements. A 1-mm-thick Berea sandstone wafer was placed at the upper end of each sample, at the pore fluid access port, in order to facilitate uniform pore fluid access and prevent the sample from squeezing out to the pore pressure port. The experimental sample and the Berea sandstone wafer were isolated from the confining pressure medium of silicon oil using polyolefin and silver jackets; the sample was saturated with distilled water for at least 12 hours before pressurization.

Both confining pressure and pore pressure were measured by pressure transducers with accuracy of 0.07 MPa and 0.02 MPa. Axial differential force and axial displacement

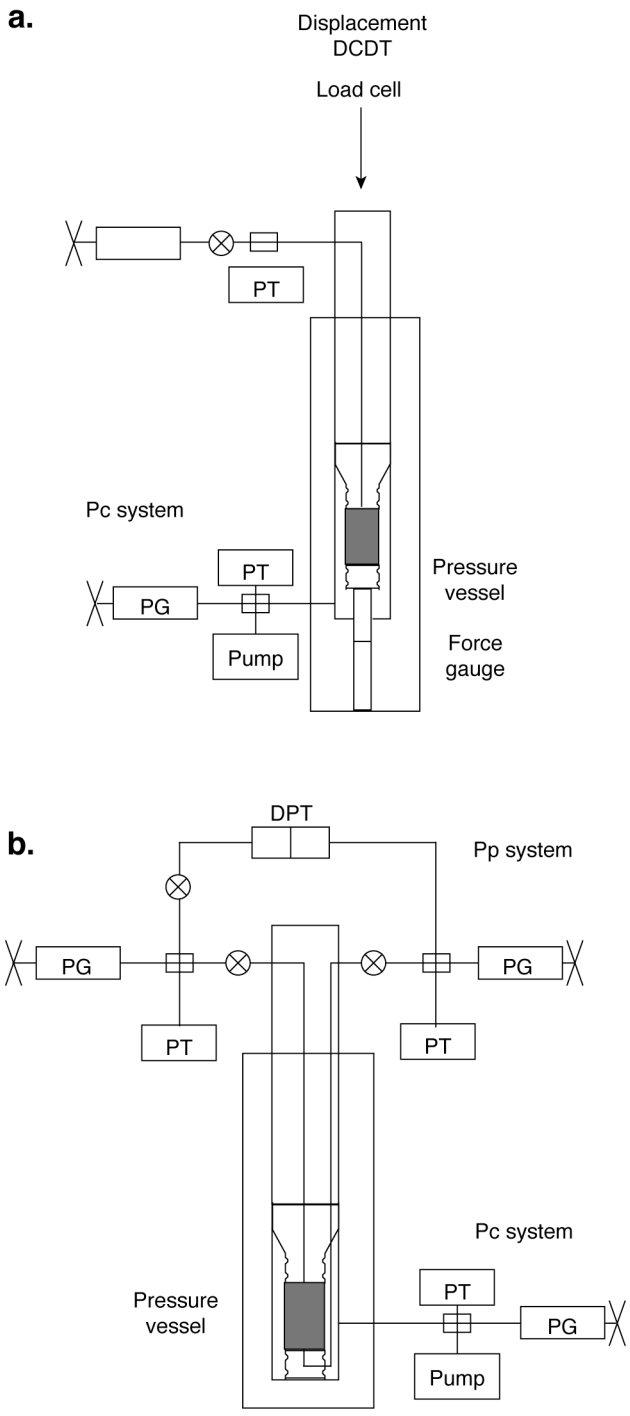

Figure 4.3. Schematic diagram of experimental systems of (a) MVSR (b) PPR. PT and PG represent pressure transducer and pressure generator, respectively.

were measured by a force gauge inside the pressure vessel (accurate to 0.2 MPa) and a displacement transducer (accurate to 8×10^{-4} mm) at the top of the loading system, respectively. The volume of pore fluid displaced from the sample was measured at the pressure generator from displacement of the piston measured with a displacement transducer (accurate to 1.5×10^{-4} cc in terms of volume). Room temperature also recorded because the pressure and displacement measurements are temperature-sensitive and the experiments lasted several weeks. The data were recorded by computer at intervals of 1 to 600 s depending on the type of experiment being conducted.

Different stress paths of (1) isotropic loading, (2) uniaxial strain loading (K_0 consolidation), (3) triaxial loading at constant Pc, (4) undrained Pc reduction (cf. modified undrained test [*Tembe et al.*, 2006]), (5) drained Pc reduction, and (6) triaxial unloading at constant Pc were achieved in the same apparatus (Figure 4.1b). An experiment usually included a series of load paths of (1), (3), (4), (5), and (6) or a series of load paths of (2), (4), (5), and (6). During isotropic loading ($\sigma_1 = \sigma_2 = \sigma_3$ = const.), confining pressure was incremented stepwise with keeping pore pressure a constant 10MPa. When confining pressure is increased, pore volume is decreased and excess pore pressure is developed within the sample. By draining excess pore pressure, consolidation proceeds. After a few hours to several days when pore pressure approaches equilibrium, permeability and axial shortening were measured, and then confining pressure was increased to achieve another step of consolidation. Axial shortening of the sample was determined during isotropic loading by displacing the upper piston to the hit point, i.e. the point at which differential

loading initiates, for each consolidation step. Following the isotropic loading, conventional triaxial compression loading at constant confining pressure ($\sigma_1 > \sigma_2 = \sigma_3 =$ const.) was conducted. Confining pressure and pore pressure were kept constant and the axial load was applied at the constant displacement rate.

In uniaxial strain consolidation, the axial load was applied at constant displacement rate. No radial strain condition is achieved by measuring both axial and volumetric strains in a manner different than the typical approach of constraining axial strain or by directly measuring the radial strain [e.g., *Morgan and Ask*, 2004]. Because radial strain, ε_r must be zero in a uniaxial strain condition, volumetric strain equals the axial strain, $\varepsilon_p = \varepsilon_a$ from the Equation (4.6). Accordingly, confining pressure was manually controlled during axial shortening to maintain volumetric strain equal to the axial strain (and volumetric strain rate equal to the axial strain rate). Note that the stress path for uniaxial strain loading is an outcome of the experiment where the strain condition is constrained, while isotropic loading and triaxial loading constrain the stress paths. The stress path is expressed by the slope of q/p' or K, which is the ratio of σ_3/σ_1.

$$\frac{q}{p'} = \frac{3-3K}{1+2K} \tag{4.9}$$

$$K = \frac{3-(q/p')}{3+2(q/p')} \tag{4.10}$$

Isotropic loading has q/p' of 0 and K of 1, and triaxial loading has q/p' of 3 and K of 0. K_0 is a slope of K during uniaxial strain loading.

Undrained and drained Pc reduction was conducted following uniaxial strain loading or triaxial loading. In this load path the axial loading was kept at constant shortening rate, confining pressure was manually reduced. The reduction rate of confining pressure was manually controlled so that pore pressure remains constant (indicating no change in volumetric strain, i.e., undrained). At some point, pore pressure cannot be maintained by reducing confining pressure because because the sample begins to dilate. When it reaches this point, the pore fluid is allowed to drain into the sample to keep pore pressure constant (drained) and confining pressure is slowly decreased.

To make permeability measurements, the sample was allowed to equilibrate, after the axial shortening rate was set to zero, until the rate of pore pressure increase indicated a strain rate of less than 10^{-7} s^{-1}, i.e. slow enough to drain excess pore pressure from the experimental samples and the transient pulse-decay method would be accurate. The transient pulse decay method involves an abrupt increase in pore pressure at one end of the sample and then monitoring the subsequent evolution in pore pressure at either one end or both ends of the sample during equilibration [e.g., *Brace et al.*, 1968; *Hsieh et al.*, 1981]. This method is more practical than steady-state flow methods especially for low permeability samples such as shale [e.g., *Kwon et al.*, 2004]. *Heish et al.* [1981] and *Neuzil et al.* [1981] present analytical solutions for the transient pulse-decay method, and a graphical method for analyzing experimental data, to obtain the hydraulic properties of the sample, i.e., hydraulic conductivity and specific storage. The analytical

solution for dimensionless hydraulic head (pore pressure), as a function of time after the step change, in the upstream and downstream reservoirs are given by

$$\frac{p_u}{P}=\frac{h_u}{H}=\frac{1}{1+\gamma+\beta}+2\sum_{m=1}^{\infty}\frac{\exp\left(-\alpha\phi_m^2\right)\left(\beta+\gamma^2\phi_m^2/\beta\right)}{\left[\gamma^2\phi_m^4/\beta^2+\left(\gamma^2\beta+\gamma^2+\gamma+\beta\right)\phi_m^2/\beta+\left(\beta^2+\gamma\beta+\beta\right)\right]} \tag{4.11}$$

$$\frac{p_d}{P}=\frac{h_d}{H}=\frac{1}{1+\gamma+\beta}+2\sum_{m=1}^{\infty}\frac{\exp\left(-\alpha\phi_m^2\right)\left(\beta-\gamma\phi_m^2/\beta\right)}{\left[\gamma^2\phi_m^4/\beta^2+\left(\gamma^2\beta+\gamma^2+\gamma+\beta\right)\phi_m^2/\beta+\left(\beta^2+\gamma\beta+\beta\right)\cos\phi_m\right]} \tag{4.12}$$

where $\alpha=\frac{Kt}{l_2S_s}$, $\beta=\frac{S_sAl}{S_u}$, $\gamma=\frac{S_d}{S_u}$, and ϕ_m are the roots of $\tan\phi=\frac{(1+\gamma)\phi}{\gamma\phi^2/\beta-\beta}$.

The parameters, p_u and p_d are the pore pressure in the upstream and the downstream reservoirs, h_u and h_d are the hydraulic head in the upstream and the downstream reservoirs, and P and H are the initial difference in pore pressure and hydraulic head at time t=0. Parameters A, l, K and Ss are the cross-sectional area, the length, the hydraulic conductivity, and the specific storage of the sample, and S_u and S_d are compressive storage of the upstream and the downstream reservoirs, respectively.

One-end pulse-decay method was used in the MVSR apparatus, in which the pore pressure system was connected only to the upper end of the experimental sample and the downstream face of the sample is an impermeable boundary (Figure 4.3a). For this

case γ=0, and the analytical solution for dimensionless hydraulic head (pore pressure) in the upstream reservoirs is given by

$$\frac{p_u}{P} = \frac{h_u}{H} = \frac{1}{1+\beta} + 2\sum_{m=1}^{\infty} \frac{\exp\left(-\alpha\phi_m^2\right)}{\phi_m^2/\beta + \beta + 1}. \tag{4.13}$$

Pore pressure was quickly increased by ~1MPa and monitored until reaching equilibrium, since analytical solutions with different hydraulic conductivities and different storage capacities show almost the same behavior as equilibrium is achieved in a single-end case [*Heish et al.*, 1981]. The normalized pore pressure data was matched with the analytical solutions to compute hydraulic conductivity and specific storage of sample [*Neuzil et al.*, 1981]. The compressibility of upstream reservoir, C_u was measured in advance using metal sample with zero permeability to determine a value of 9.11×10^{-9} m^3/MPa. The compressive storage of the upstream reservoir, S_u, was computed as 8.92×10^{-11} m^2 from the relationship, $S_u = \rho_w g C_u$, where ρ_w and g are density and of pore fluid and gravity.

We also conducted two-end pulse decay permeability measurements on a sample during isotropic loading up to 50 MPa using a different apparatus (PPS) in which no differential axial loading was available but both ends of the sample were connected to the pore pressure system (Figure 4.3b). In this apparatus, double-ended pulse-decay is conducted by increasing the pore pressure of the upstream reservoir by ~1MPa at t=0 and monitoring the pore pressure of both the upstream and the downstream reservoirs. The compressibilities of upstream and downstream reservoirs, C_u and C_d, were

determined by dedicated calibration tests as 7.96×10^{-9} m^3/MPa and 8.51×10^{-9} m^3/MPa, respectively, and the compressive storages, S_u and S_d were determined as 7.79×10^{-11} m^2 and 8.33×10^{-11} m^2, respectively.

4.5. Results

4.5.1. Pulse decay permeability measurements

For comparison, permeability measurements using one-end and two-end pulse decay methods were made on specimens taken from the same whole-round core sample, 316-C0006F-8R-1, at the same condition of p' = 8MPa during isotropic loading (Figure 4.4). For one-end pulse decay, the normalized pore pressure data is well matched to an analytical solution where β= 0.8, and t = 1900 at $\alpha\beta^2 = 1$. From the relationships of $\alpha = Kt/l_2S_s$ and $\beta = S_sAl/S_u$, we computed S_s=7.97×10^{-6} m^{-1} and K=6.70×10^{-12} m/s. Intrinsic permeability k is calculated as 6.86×10^{-19} m^2 from the relationship $k = K\rho_w g/\mu$, where ρ_w and μ are density and dynamic viscosity of pore fluid, respectively. For two-end pulse decay, the experimental data matches an analytical solution of β=0.3 and t=4400 at $\alpha\beta^2$=1. Specific storage, hydraulic conductivity, and intrinsic permeability were computed as S_s=7.48×10^{-6} m^{-1}, K=2.31×10^{-12} m^2, and k=2.36×10^{-19} m^2, respectively. Permeability from two-end pulse decay measurement is three times lower than that from one-end pulse decay measurement, whereas specific storage values are

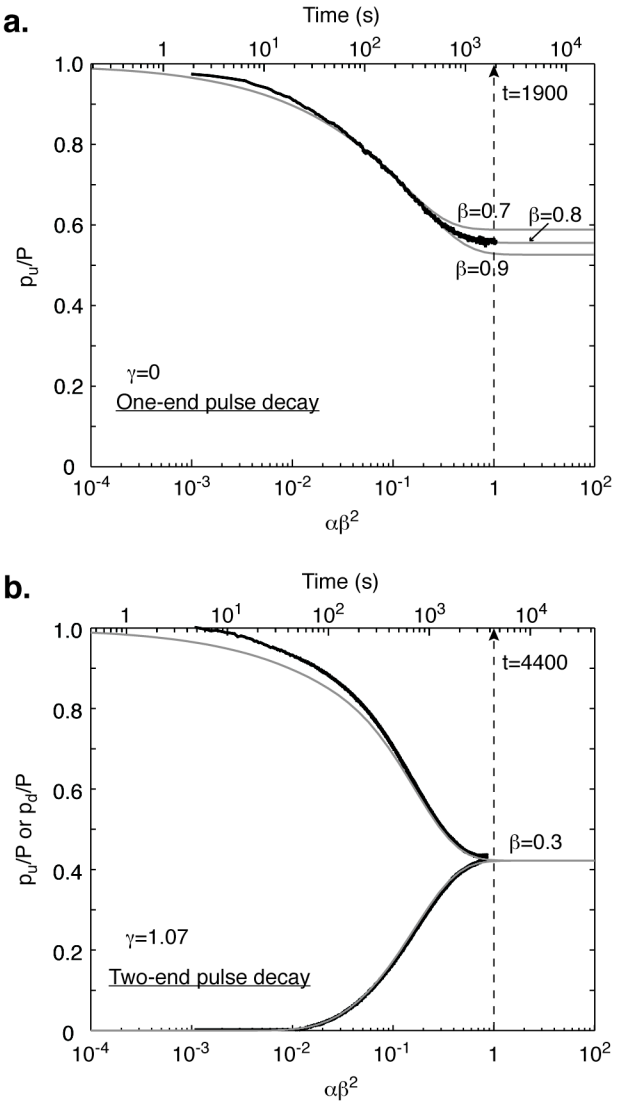

Figure 4.4. Examples of transient pressure change during pulse decay measurements at the effective pressure of 8 MPa during isotropic loading. (a) One-end pulse decay in MVSR. (b) Two-ends pulse decay in PPR.

almost the same. This difference is seen in measurements at all pressure conditions. It is worth noting that hydraulic properties are also dependent on sample geometry, i.e., the length and the cross-sectional area. In the triaxial deformation apparatus (MVSR), we can estimate the axial and radial strains from the measured axial displacement and pore volume change. On the other hand, it is impossible to estimate the axial and radial strains in the other apparatus (PPS) because it does not have an axial loading frame. When calculating the hydraulic properties from pulse decay conducted in PPS (316-C0006F-8R-1-c), we assume that the deformation behavior and thus the ratio of ε_r to ε_a of this experiment are same as those of the experiment, 316-C0006F-8R-1-b which was isotropically loaded on MVSR.

Specific storage of the sample can be written as a function of water compressibility and coefficient of compressibility of the sample,

$$S_s = \rho_w g[\beta n + \alpha(1-n)] \tag{4.14}$$

where β is water compressibility and α is coefficient of compressibility. Specific storage ranges from 3×10^{-6} to 3×10^{-5} m^{-1}. With n=0.4, α is calculated as 1.06×10^{-9} Pa^{-1}. To ensure the pore pressure is equilibrated during deformation experiments, *Lee* [1981] suggests that the strain rate used for CRS (constant rate of strain) test should satisfy the relationship,

$$\varepsilon_a' l^2 / C_v < 0.1 \tag{4.15}$$

where ε_a' is axial strain rate and C_v is coefficient of consolidation. Since $C_v = k\mu/\alpha\rho_w{}^2 g^2$, the maximum strain rate that should be used is,

$\varepsilon_a' < 0.1k\mu/l^2\alpha\rho_w{}^2g^2 = 4.23\times10^{-5}$. The axial strain rate of 10^{-7} s^{-1} used in this paper satisfies this condition.

4.5.2. Evolution of strength and permeability along different stress paths

The stress path for each experiment is summarized in Table 4.2, and the stress-strain behavior, stress evolutions in p'-q space, permeability as a function of effective mean stress, and volumetric strain vs log σ_l for each experiment are shown in Figures 4.5, 4.6 and 4.7. For uniaxial strain loading, three stages of strength evolution can be distinguished by changes in the stress strain response. Differential stress increases significantly with axial strain up to ~2% shortening during Stage I, and stays almost constant during Stage II. Two samples of 316-C0004D-48R-1 and 316-C0006F-8R-1-a show further strengthening with strain in Stage III. K_0 is 0.3-0.4 for stage I, approximately 1 for stage II, and 0.55 for stage III. We interpret Stages I, II, and III as an elastic response, yielding with cement breakage [e.g., *Karig*, 1993; *Mogan and Ask*, 2004], and normal consolidation, respectively. For triaxial loading, the sample of 316-C0006F-8R-1 continuously strengthens with a slight change in the slope of stress-strain curve at axial strain of 6% (Figure 4.7d). Differential stress increases with a steeper slope in the stress-strain curves during undrained Pc reduction, and decreases during drained P_c reduction (Figures 4.5a, 4.6a, 4.7a, and 4.7e). These can be also seen in the p'-q diagram. i.e., q increases during undrained Pc reduction and decreases during drained Pc reduction with

Table 4.2. Summary of experimental results. σ_v': in-situ effective vertical stress, σ_{v0}': effective vertical preconsolidation pressure, *OCR*: overconsolidation ratio, (σ_{v0}'/ σ_v'), p_y': yield effective mean stress, q_v: yield differential stress, p_0': effective mean preconsolidation pressure, *M*: slope of critical state line, $S_{u(NC)}$: undrained shear strength for normal consolidated sample, $S_{u(NC)}$: undrained shear strength for overconsolidated sample, ϕ: Internalfriction angle, *c*: Cohesive strength, and C_0: unconfined compressive strength.

Experimental samples/	Load paths	σ_v' (MPa)	σ_{v0}' (MPa)	*OCR*	p_y' (MPa)	q_y (MPa)	p_0' (MPa)	*M*	$S_{u(NC)}$ (MPa)	S_u (MPa)	ϕ (°)	*c* (MPa)	C_0 (MPa)
315-2B-63R-1	K0 + Pc reduction	8.8	12.3	1.40	10.8	2.25	14.0	0.8	4.12	3.86	22	0.99	2.94
316-4D-48R-1	K0 + Pc reduction	2.7	6.32	2.34	5.55	1.16	7.0	1.0	2.54	2.14	20	0.73	2.09
316-6F-8R-1-a	K0 + Pc reduction	4.4	11.5	2.61	10.1	2.1	12.7	0.9	4.29	3.53	15	0.93	2.42
316-6F-8R-1-b	Isotropic + triaxial + Pc reduction	4.4	11.9	2.70	11.9	0	11.9	0.9	3.93	3.21	18	0.83	2.28
316-6F-8R-1-c	Isotropic (50MPa)[1]	4.4	12.1	2.80	12.1	0	12.1	-	-	-	-	-	-

[1]conducted on PPS.

Figure 4.5. Experimental results on the sample 315-C0002B-63R-1. (a) Differential stress as a function of axial strain. (b) p-q diagram. (c) Permeability as a function of effective mean stress. (d) Volumetric strain as a function of logarithmic σ_1.

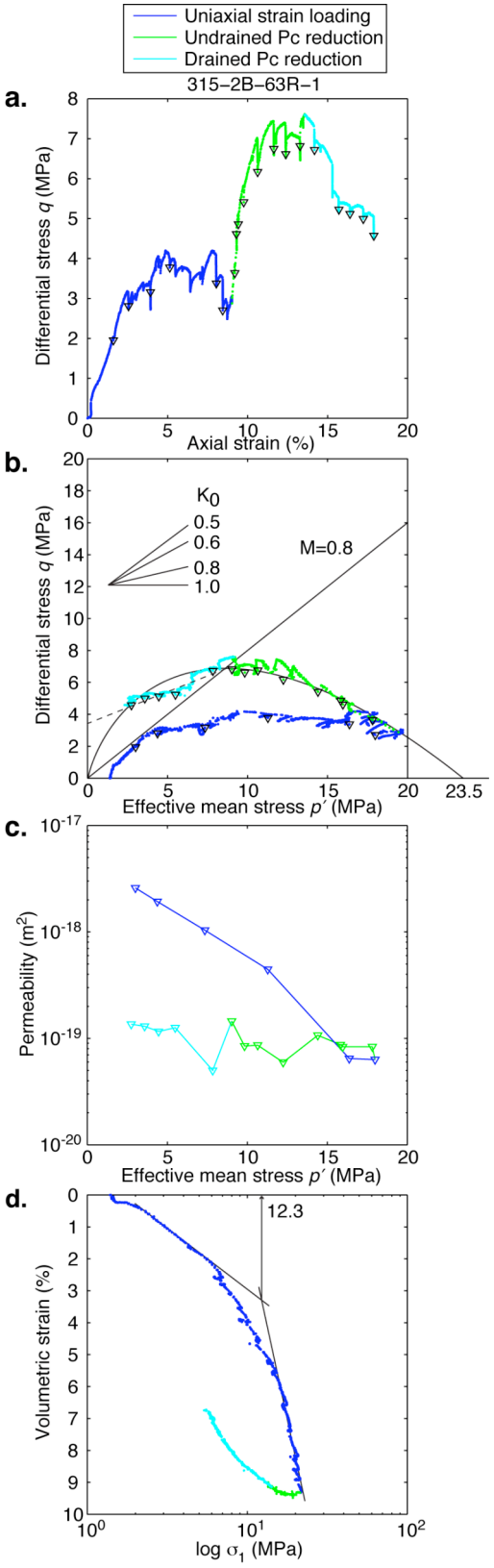
Uniaxial strain loading
Undrained Pc reduction
Drained Pc reduction
315–2B–63R–1
a.
Differential stress q (MPa)
Axial strain (%)
b.
Differential stress q (MPa)
K0
0.5
0.6
0.8
1.0
M=0.8
Effective mean stress p′ (MPa)
c.
Permeability (m2)
Effective mean stress p′ (MPa)
d.
12.3
Volumetric strain (%)
log σ1 (MPa)

Figure 4.6. Experimental results on the sample 316-C0004D-48R-1. (a) Differential stress as a function of axial strain. (b) p-q diagram. (c) Permeability as a function of effective mean stress. (d) Volumetric strain as a function of logarithmic σ_1.

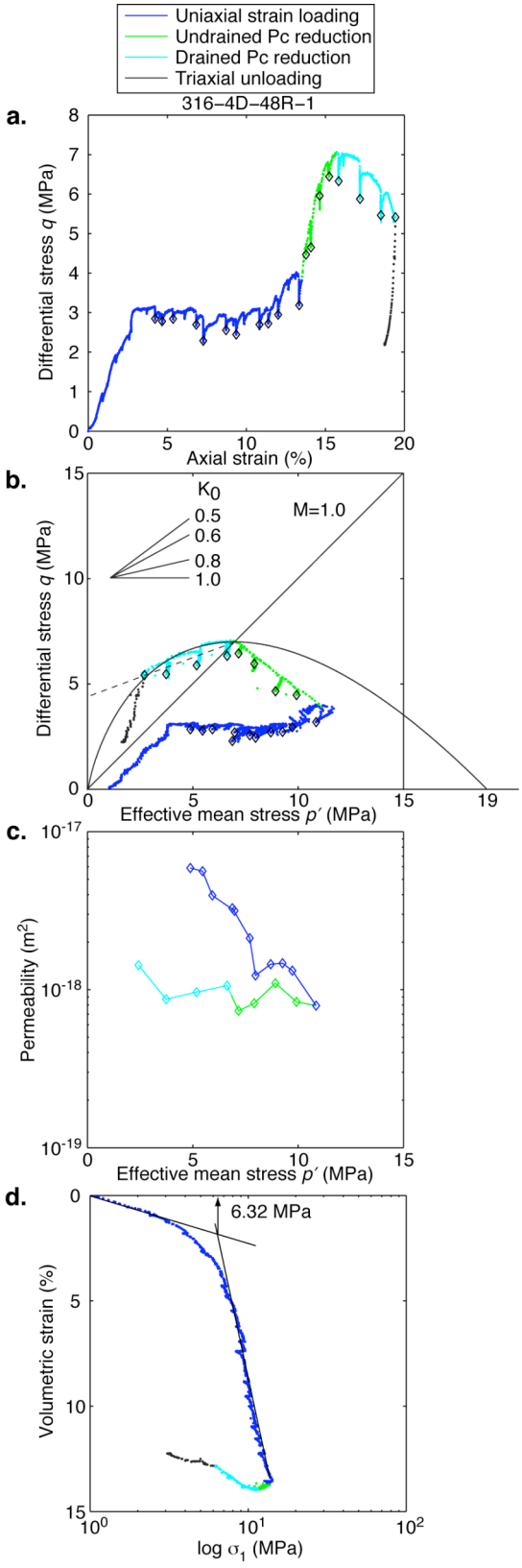
Uniaxial strain loading
Undrained Pc reduction
Drained Pc reduction
Triaxial unloading
316–4D–48R–1
a.
Differential stress q (MPa)
Axial strain (%)
b.
K0
0.5
0.6
0.8
1.0
M=1.0
Differential stress q (MPa)
Effective mean stress p′ (MPa)
c.
Permeability (m2)
Effective mean stress p′ (MPa)
d.
6.32 MPa
Volumetric strain (%)
log σ1 (MPa)

Figure 4.7. Experimental results on the samples 316-C0006F-8R-1-a and 316-C0006F-8R-1-b. (a) and (e) Differential stress as a function of axial strain. (b) and (f) p-q diagram. (c) and (g) Permeability as a function of effective mean stress. (d) and (h) Volumetric strain as a function of logarithmic σ_1.

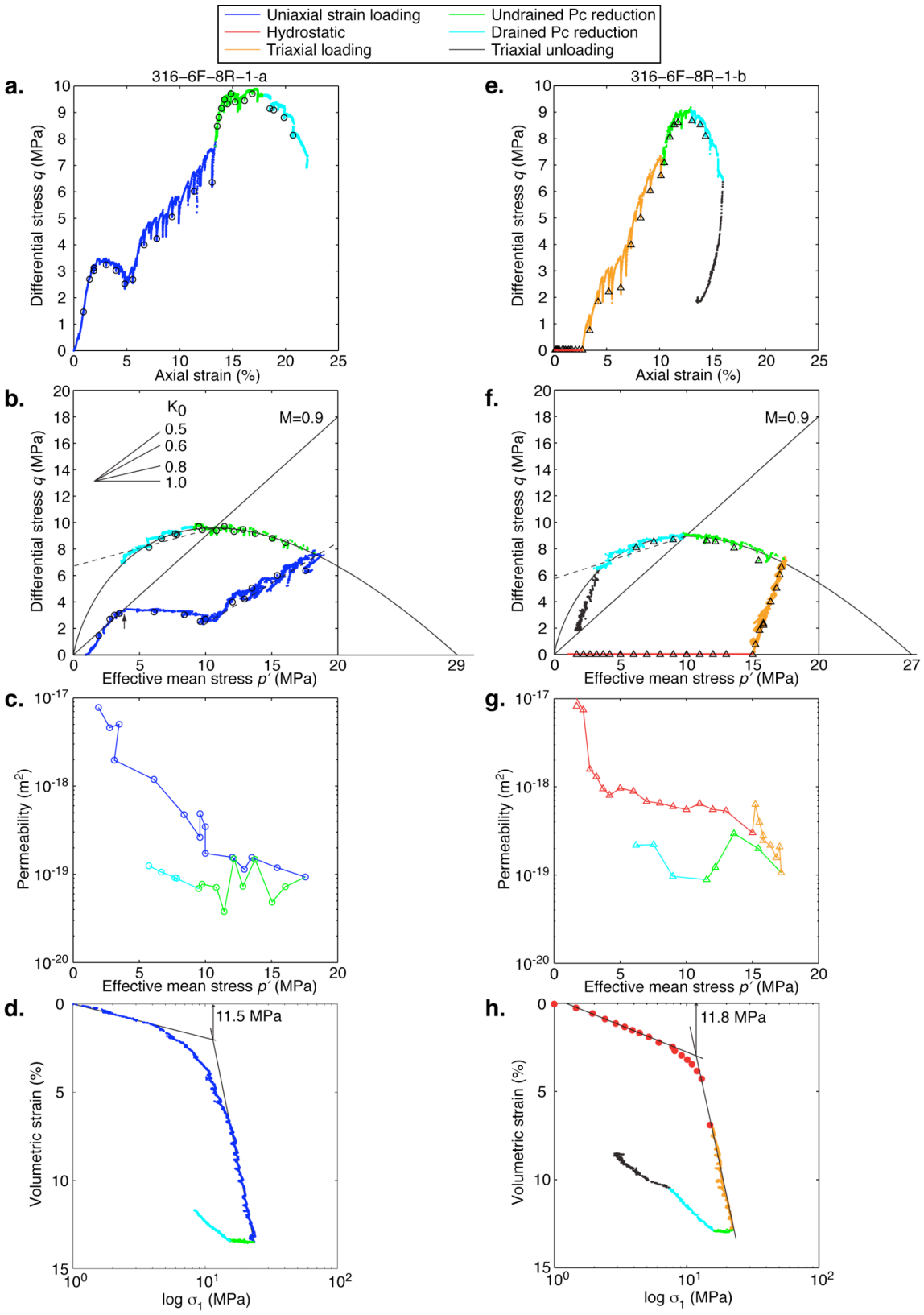
Uniaxial strain loading
Hydrostatic
Triaxial loading
Undrained Pc reduction
Drained Pc reduction
Triaxial unloading
a.
316–6F–8R–1-a
Differential stress q (MPa)
Axial strain (%)
e.
316–6F–8R–1-b
b.
K0
0.5
0.6
0.8
1.0
M=0.9
Effective mean stress p′ (MPa)
f.
c.
Permeability (m2)
g.
d.
11.5 MPa
Volumetric strain (%)
log σ1 (MPa)
h.
11.8 MPa

decreasing p' (Figures 4.5b, 4.6b, 4.7b, and 4.7f). Strength (q) reaches a maximum at the transition from undrained to drained conditions, which could demark the critical state.

The overall evolution of permeability is reduction with effective mean stress during loading and partial recovery during Pc reduction, especially during drained Pc reduction (Figures 4.5c, 4.6c, 4.7c, and 4.7g). Permeability ranges from 10^{-17} to 10^{-19} m^2 at effective mean stress of 1-20 MPa and further decreases to ~10^{-20} m^2 with pressurization to 50 MPa (316-C0006F-8R-1-c). A closer look at the two experiments, 316-C0006F-8R-1-a and 316-C0006F-8R-1-b, reveals that permeability evolution depends on the stress paths (Figures 4.7c and 4.7g). During uniaxial strain loading, permeability continuously decreases with a log-linear relationship. During isotropic loading, permeability quickly decreases at the effective pressures less than 5 MPa, and stays almost constant thereafter. The fastest reduction in permeability is observed during triaxial loading. Although permeability evolution depends on stress path, permeability ends up the same at the final point of loading where the stress states are almost the same (Figures 4.7c and 4.7g).

The preconsolidation pressure σ_{v0}' is determined from uniaxial strain loading by the intersection point of the two lines tangent to the elastic portion (Stage I) and the normal consolidation portion (Stage III) in a logarithmic plot of volumetric strain versus σ_1 (Figures 4.5d, 4.6d, 4.7d, and 4.7h) [*Holtz and Kovacs*, 1981]. It turns out that all samples have larger preconsolidation pressure than the in-situ overburden pressure σ_v',

which is calculated from the shipboard measurement of bulk density assuming that pore pressure is hydrostatic [*Expedition 315 Scientists*, 2009; *Expedition 316 Scientists*, 2009a, 2009b]. Thus, all samples are overconsolidated and *OCR* ranges 1.4-2.8 (Table 4.2).

4.6. Discussion

4.6.1. Yield surface and consolidation states

Both plastic volumetric strain and plastic shear strain are calculated by subtracting elastic strain from total strain. As given by equation (4.8), bulk modulus K' and shear modulus G' are determined from the elastic part of the relationship between effective mean stress and volumetric strain, and that between differential stress and shear strain, respectively. Bulk modulus, K' can be determined from the ratio of volumetric strain to natural logarithm of effective mean stress, κ, by the equation,

$$\kappa = \frac{\delta\varepsilon_p}{\delta(\ln p')} = \frac{p'\delta\varepsilon_p}{\delta p'} = \frac{p'}{K'}. \tag{4.16}$$

We assume that the deformation during Stage I of uniaxial strain loading, triaxial unloading, and hydrostatic unloading is perfectly elastic (Figures 4.8a and 4.8b). Once elastic parameters are obtained (e.g., G' = 340MPa and κ = 0.03 for 316-C0006F-8R-1), the plastic vector for each stress state can be plotted (Figure 4.8c). Plastic potential is normal to the plastic vector and the direction of plastic potential mostly follows the stress paths during both undrained and drained Pc reduction. Taking into account the assumption of the Cam-Clay model that the yield surface is same as the plastic potential

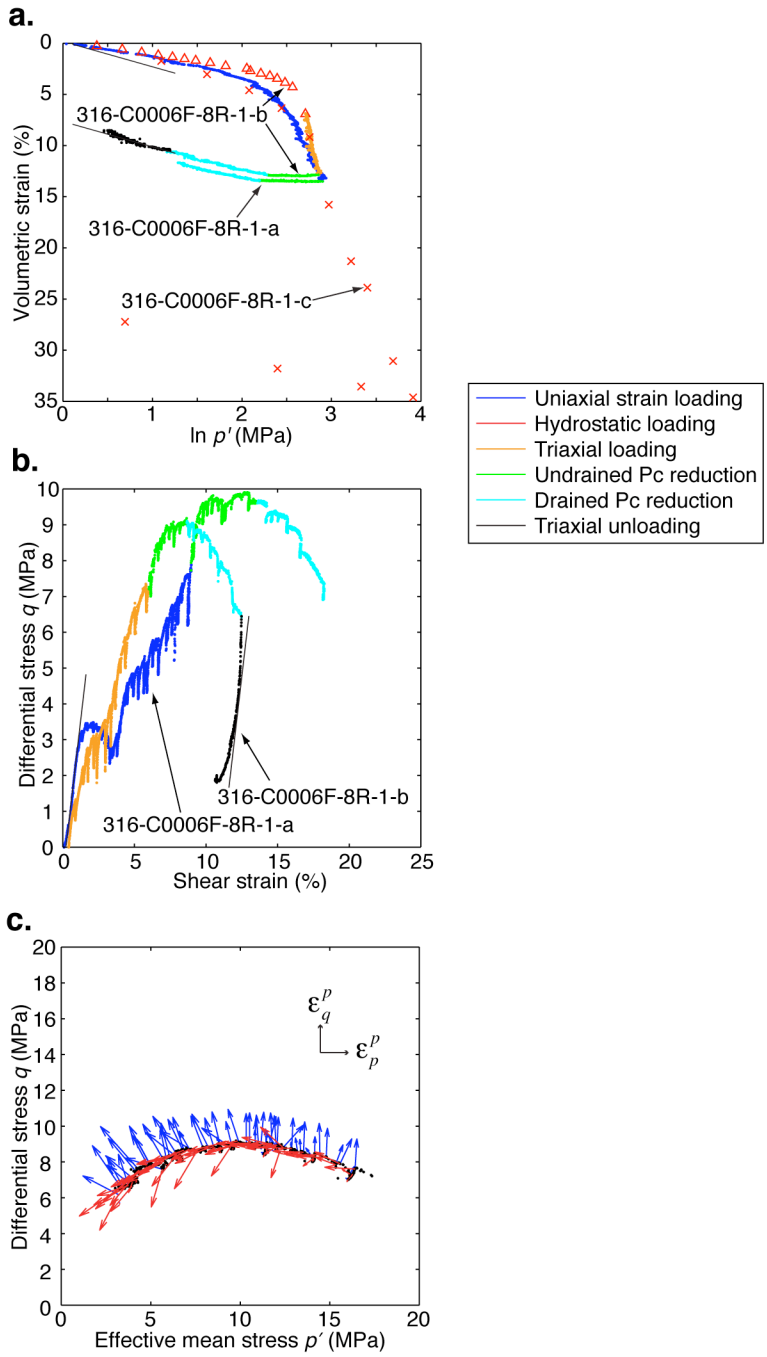

Figure 4.8. The experimental results of the samples 316-C0006F-8R-1-a, 316-C0006F-8R-1-b, and 316-C0006F-8R-1-c used for Cam-Clay model. (a) Volumetric strain as a function of effective mean stress. (b) Differential stress as a function of shear strain. (c) Plastic strain vectors (blue arrows) and the predicted plastic potential (yield surface) direction (red arrows) during undrained and drained Pc reduction tests on the sample 316-C0006F-8R-1-b. Black dots represent the stress states.

[*Wood*, 1990], and that the yield surfaces of each sample are well described by the original Cam-Clay of equation (4.4) with M of 0.8-1.2 (Table 4.2), the stress path during a Pc reduction test likely defines the yield surface (Figures 4.5b, 4.6b, 4.7b, and 4.7f).

All samples are overconsolidated, and *OCR* ranges 1.4-2.8 (Table 4.2). Overconsolidation can be explained by the cementation of the sediments, a maximum depth of burial greater than the current depth, or by a in-situ stress-strain history inconsistent with the uniaxial strain loading used in which $\sigma_v' = \sigma_l'$. To evaluate the effect of cementation on consolidation state and preconsolidation stress is not easy and would require future study. Thus, we evaluate the other possibilities here.

A greater depth of burial in the past than in the present can be explained by two cases; (1) the sediment overburden above the sample in the past are removed in the present or (2) the sample have moved from the depth during thrusting deformation. Considering the geological setting, the samples 316-C0004D-48R-1 and 316-C0006F-8R-1 can be case (1) and case (2), respectively. The sample C0002B-63R-1 is from the older accretionary prism sediment, and thus the deformation history is not clear. Also, since this old sample has the smallest *OCR* among the three samples presented herein, overconsolidation could be explained solely by the effect of cementation.

The sample 316-C0004D-48R-1 is underthrust slope sediment, and overlain by accreted sediments and the overlying younger slope sediments across the megasplay fault. There is ~ 1 m.y. (1.5-2.5 Ma) unconformity between the accreted sediments and the overlying slope sediments [*Expedition 316 Scientists*, 2009a]. If we assume that bulk density of the removed sediment is same as the averaged bulk density of slope sediment

of ~1.66 and pore pressure is hydrostatic, then the thickness of the slope sediment that would have had to been above the present sea floor removed to produce a σ_v' equal to the preconsolidation stress is estimated as 580 m. For such a large thickness of sediment to have accumulated (and then removed) during ~1 m.y. period would require an average sedimentation rate greater than ~580 m/m.y., which is much faster than the sedimentation rate of approximately 50 m/m.y. recorded at Site C0008 during the same time period, and the sedimentation rate at Site C0008 is very high because of the proximity to the megasplay (Figure 4.2c). Thus, even if some sediment is missing, other possibilities should also be considered to explain the overconsolidation.

The sample 316-C0006F-8R-1 is from the top of the Upper Shikoku Basin sediment overthrust along the frontal thrust. The deepest depth at which the overthrusted sediments have been buried could be the depth before the start of overthrusting. This depth can be considered as equivalent to that of the proto-thrust forming the next, future frontal thrust. Since the development of accretionary prism is self-similar [e.g., *Davis et al.*, 1983] and the initiation evolution of the proto-thrust is observed right below the Site C0006 in the seismic data [*Moore et al.*, 2009], we assume that the sample 316-C0006F-8R-1 had been buried, before underthrusting initiated, to a depth equivalent to the depth of the present proto-thrust. The thickness of Upper Shikoku Basin in the hanging wall and trench wedge sediment in the footwall is estimated as approximately 220m and 1120m from the seismic reflection data, respectively (Figure 4.2d) [*Moore et al.*, 2009]. We assume that pore pressure is hydrostatic at any depth and that the trench wedge sediment and the Upper Shikoku Basin sediment in the footwall have the averaged bulk

densities of the trench sediment (Unit II) and Upper Shikoku Basin sediment (Unit III) in the hanging wall of the frontal thrust, from which the cored samples were recovered during Expedition 316 [*Expedition 316 Scientists*, 2009b]. The in-situ effective overburden pressure for the top of the Upper Shikoku Basin in the proto-thrust zone is estimated as 13.2 MPa, which is slightly higher pressure than the preconsolidation pressure of 12.3 MPa estimated from the experiments. It might be considered an overestimate due to the assumption of hydrostatic pore pressure for underthrusted sediment at the proto-thrust. The previous studies have suggested that overpressure would be developed and sediment would be underconsolidated due to the fast loading of sediments and their low permeability [e.g., *Screaton et al.*, 2002; *Saffer* 2003]. It is crucial to estimate the pore pressure and the consolidation states for the underthrust sediments at this transect in order to understand the deformation mechanism and history of the frontal thrust.

The preconsolidation pressure determined in uniaxial strain tests represents the maximum vertical stress experienced by the sediment in the past, and is most appropriately applied to the natural case of flat-lying sediments loaded by overburden where lateral strains are expected to be small [e.g., *Terzaghi et al.*, 1996]. In an accretionary subduction zone, horizontal stress magnitude can vary with position and time, and will constitute the maximum principal compressive stress in regions of accretion and thusting [e.g., *Karig*, 1990; *Jones* 1994; *Morgan et al.*, 2007]. Accordingly, we consider the effect of the horizontal stress in evaluating the consolidation state of sediments. To do this, we estimate an effective mean preconsolidation stress (same as a

reference effective mean stress in Cam-Clay model), p_0', to define virgin yield envelopes. The effective mean preconsolidation stress is determined from the logarithmic plot of volumetric strain versus p' (Figure 4.9a). As the vertical preconsolidation stress is estimated as the value at the intersection of two lines tangent to the elastic portion and the normal consolidation portion, the effective mean stress at yield, p_y' is determined. In isotropic loading, $p_y'=p_0'$, while in non-isotropic loading where $q \neq 0$, p_0' is determined from Equations (4.1), (4.2), and (4.4) with σ_{v0}' and M that were determined for each sample in the precious sections. Once p_0' is determined, the virgin yield surface can be constructed (Figures 4.9b-4.9d). The values of p_0' estimated in non-isotropic loading tests, 316-C0006F-8R-1-a and 316-C0006F-8R-1-b are comparable to p_0' of isotropic loading test, 316-C0006F-8R-1-c (Figure 4.9d and Table 4.2). We also present p_0' and yield envelopes at the end of elastic portion and the onset of normal consolidation (Figures 4.9b-4.9d). We call them as a pre-yield envelope and a post-yield envelope, respectively. Interestingly, the transitions from Stage I (elastic deformation) to Stage II (cement breakage) in uniaxial strain loading are on the pre-yield envelope except for the sample 316-C0004D-48R-1, in which the transition lies on the vergin yield surface. The onset of Stage III (normal consolidation) seems to lie on the post-yield surface, although Stage III is not clear in the sample 315-C0002B-63R-1. In addition, the sample 316-C0006F-8R-1 shows faster increase in differential stress just before Stage III, and it might be related to experimentally-formed compaction bands, which are not observed in other deformed samples.

Figure 4.9. Effective mean preconsolidation pressure and yield envelopes. (a) Volumetric strain as a function of effective mean stress of the samples 315-C0002B-63R-1, 316-C0004D-48R-1, and 316-C0006F-8R-1-a. (b), (c), (d) Yield envelopes for the samples 315-C0002B-63R-1, 316-C0004D-48R-1, and 316-C0006F-8R-1-a, respectively. Bold envelopes are the virgin yield envelopes, dashed envelopes are the pre-yield envelopes, and dashed-dot envelopes are the post-yield envelopes. The squares indicate the stress states at yield points, which are chosen in the logarithmic plot of volumetric strain vs p'.

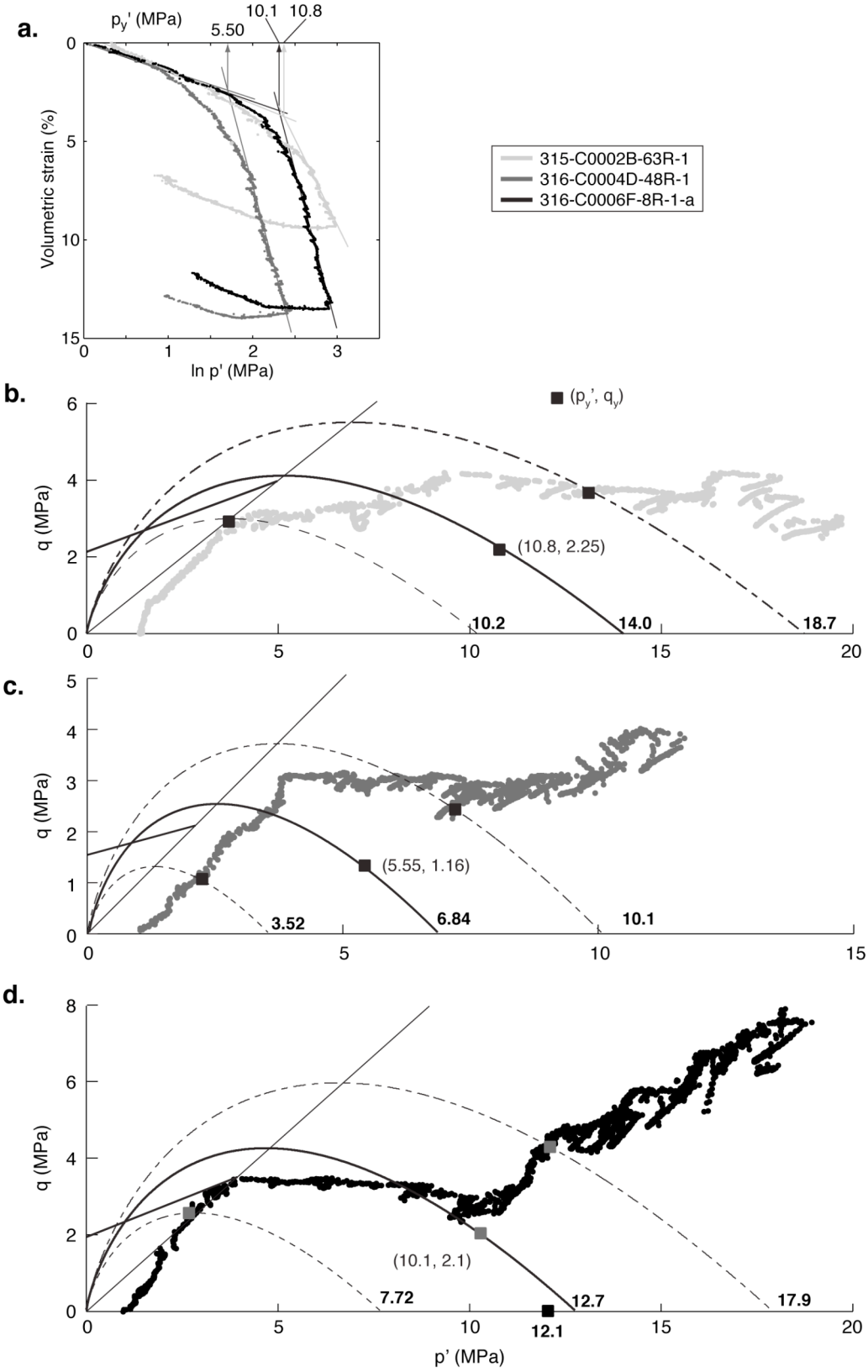
a.
p_y' (MPa)
5.50
10.1
10.8
Volumetric strain (%)
ln p' (MPa)
315-C0002B-63R-1
316-C0004D-48R-1
316-C0006F-8R-1-a
b.
(p_y', q_y)
(10.8, 2.25)
10.2
14.0
18.7
q (MPa)
c.
(5.55, 1.16)
3.52
6.84
10.1
d.
(10.1, 2.1)
7.72
12.7
12.1
17.9
p' (MPa)

4.6.2. Estimation of in-situ horizontal stress

Undrained shear strength can be estimated from the yield surface. The SHANSEP model (stress history and normalized soil engineering properties) are designed to estimate the undrained shear strength for overconsolidated sediments [*Ladd and Foott*, 1974]. Undrained shear strength for overconsolidated sediment can be calculated from the normalized relationship of

$$\frac{S_u}{\sigma'_v} = \left(\frac{S_u}{\sigma'_v}\right)_{NC} \cdot OCR^m \tag{4.17}$$

where S_u is the undrained shear strength and m is a material constant, which typically ranges between 0.7 and 0.9. NC stands for normal consolidation. We assume that $(S_u)_{NC}$ is the differential stress at the critical state and $(\sigma'_v)_{NC} = \sigma'_{v0}$. With m = 0.8, undrained shear strength is estimated as S_u =3.86 MPa for 315-C0002B-63R-1, S_u = 2.14 MPa for 316-C0004D-48R-1, and S_u = 3.53 MPa for 316-C0006F-8R-1. Unfortunately, it is not possible to compare these results to the shipboard measurements of undrained shear stress by vane shear and penetrometer, both of which can be only used for soft samples.

Although the drained Pc reduction is well matched to the Cam-Clay yield surface, it could follow the friction-based failure criteria such as the Coulomb failure criteria.

$$\tau = c + \sigma \tan\phi \tag{4.18}$$

where τ is shear stress, σ is normal stress, c is cohesive strength, and ϕ is internal friction

angle. Equation (4.18) can be rewritten in terms of effective mean stress and differential stress,

$$q = \frac{6c\cos\phi}{3-\sin\phi} + p' \frac{6\sin\phi}{3-\sin\phi}. \tag{4.19}$$

The best-fit of (4.19) to the stress path during undrained Pc reduction (Figures 4.5b, 4.6b, 4.7b, and 4.7f), gives the internal friction angle. From this angle and undrained shear strength, the best-fit Coulomb failure line can be derived, and thus cohesive strength can be calculated (Figures 4.9c-4.9e and Table 4.2). Jaeger and Cook [1979] show the relationship between the maximum and the minimum principal stresses is given by

$$\sigma_1 = 2c[(1+\mu^2)^{1/2}+\mu] + [(1+\mu^2)^{1/2}+\mu]^2\sigma_3 = C_0 + [(1+\mu^2)^{1/2}+\mu]^2\sigma_3 \tag{4.20}$$

where unconfined compressive strength C_0 is described as a function of cohesive strength c and coefficient of internal friction, μ $(=\tan\phi)$, in a relation of $C_0 = 2c[(1+\mu^2)^{1/2}+\mu]$. Given that the stress in crust is limited by the frictional strength described by Equation (4.20) and follow Anderson's faulting theory, the range of possible stress states of each sample is estimated for normal faulting, strike slip faulting, and reverse faulting environment and presented as stress polygons (Figures 4.10a, 4.10c, 4.10e, and 4.10g) [*Zoback et al.*, 2003].

Horizontal stress magnitude was estimated from breakout width and the empirical rock strength parameters of unconfined compressive strength and internal friction coefficient during Expedition 314 [*Expedition 314 Scientists*, 2009], based on the

Figure 4.10. Estimation of in-situ stress conditions from stress polygons and yield envelopes. (a) Schematic diagram of stress polygons. All stresses are total stress, not effective stress. The region with labels of NF, SS, and TF represent the stress conditions for normal faulting, strike-slip faulting, and thrust faulting, respectively. (b) Schematic diagram of possible stress states in p'-q diagram. (c), (e), (g) Stress polygons and the relationship between the maximum and minimum horizontal stress (bold lines) estimated from the breakout data. (d), (f), (h) Yield envelopes and predicted in-situ stress states. Possible stress states are the region bounded by yield surface and the two lines of (1) and (4). (c) and (d), (e) and (f), and (g) and (h) show the results of the samples 315-C0002B-63R-1, 316-C0004D-48R-1, and 316-C0006F-8R-1-a, respectively.

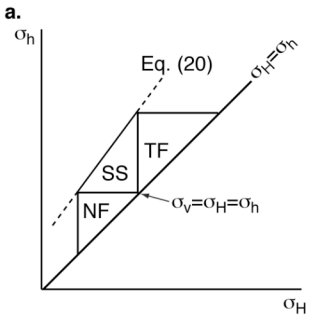

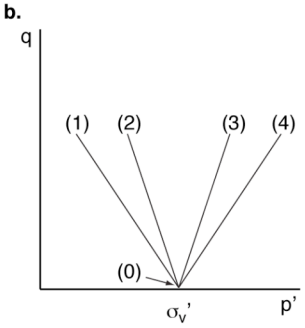

Isotropic	(0) $\sigma_h' = \sigma_H' = \sigma_v'$	$p'=\sigma_v'$, $q=0$
	(1) $\sigma_h' = \sigma_H' < \sigma_v'$	$q= -1.5p'+1.5\sigma_v'$
Normal	$\sigma_h' < \sigma_H' < \sigma_v'$	
	(2) $\sigma_h' < \sigma_H' = \sigma_v'$	$q= -3p'+3\sigma_v'$
Strike-slip	$\sigma_h' < \sigma_v' < \sigma_H'$	
	(3) $\sigma_h' = \sigma_v' < \sigma_H'$	$q= 3p'-3\sigma_v'$
Thrust	$\sigma_v' < \sigma_h' < \sigma_H'$	
	(4) $\sigma_v' < \sigma_h' = \sigma_H'$	$q= 1.5p'-1.5\sigma_v'$

315-C0002B-63R-1

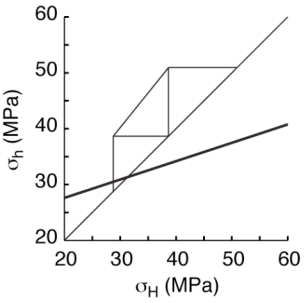

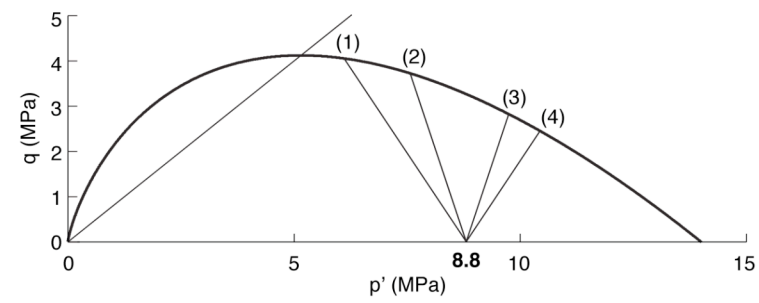

316-C0004D-48R-1

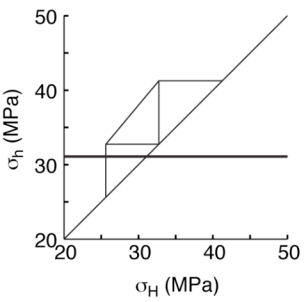

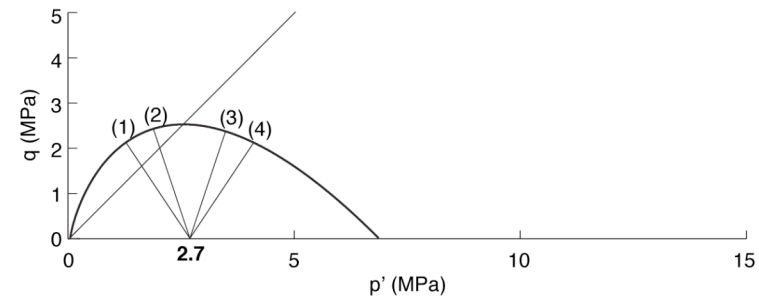

316-C0006F-8R-1-a

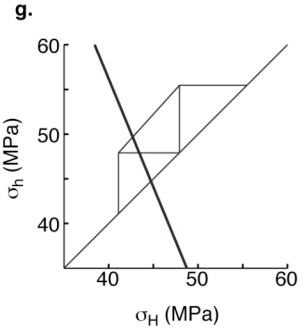

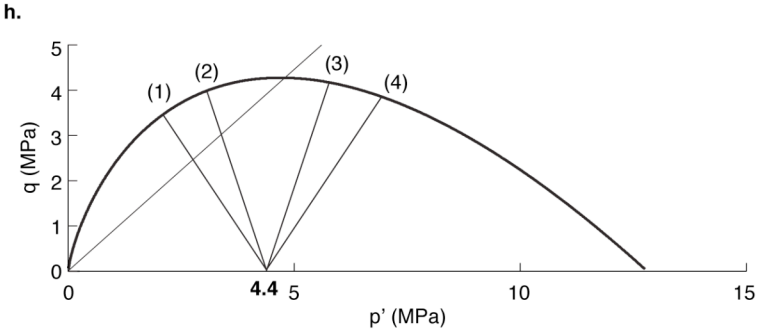

relationship,

$$\sigma_H = \frac{(C_0 + 2P_p + \Delta P) - \sigma_h(1 + 2\cos 2\theta_b)}{1 - 2\cos 2\theta_b} \tag{4.21}$$

where σ_H and σ_h are the maximum and minimum horizontal stresses, P_p is pore pressure, ΔP is the difference between the wellbore pressure and the pore pressure, i.e., excess pore pressure, and θ_b is the breakout width. Using the estimated unconfined compressive strength C_0, the possible relationship between the maximum and minimum horizontal stress magnitude is estimated as a line (Figures 4.10c, 4.10e, 4.10g, and Table 4.2). We assume that pore pressure is hydrostatic, and ΔP is 0. All samples show that the horizontal stress is in the normal fault regime, except the sample 316-C0006F-8R-1 is also in the strike-slip fault regime (Figures 4.10c, 4.10e, 4.10g).

Since the consolidation state can be represented by the yield surface in p'-q space (Figure 4.9b-4.9d), possible in-situ stress conditions can be also understood in p'-q space. The present in-situ stress subjected to the samples should be within or on the yield surface. The in-situ effective vertical stress is estimated from the shipboard measurement bulk density of the overburden sections assuming hydrostatic pore pressure, but the horizontal stress magnitude is unknown. During the Expedition 314, the estimation of in-situ horizontal stress has been attempted from the logging breakout data, but mechanical properties of sediments such as UCS and frictional angle are constrained by the empirical equations for the similar sediment samples not by the laboratory measurement of the strength on the real samples [*Tobin et al.*, 2009b]. We consider four representative

relationships between effective vertical stress σ_v', maximum horizontal stress σ_H', and minimum horizontal stress σ_h'; (1) $\sigma_h' = \sigma_H' < \sigma_v'$, (2) $\sigma_h' = \sigma_H' < \sigma_v'$, (3) $\sigma_h' = \sigma_v' < \sigma_H'$, (4) $\sigma_v' < \sigma_h' \ \sigma_H'$. Although effective stresses are used here, but these are also applicable to total stress. From the Equations (4.1) and (4.2) with the effective overburden pressure σ_v', the linear relationships between p' and q are obtained for each case (Figure 10b) and all four lines are intersected at $p'=\sigma_v'$. This point represents the isotropic stress condition, $\sigma_h' = \sigma_H' = \sigma_v'$. More general stress states of (5) $\sigma_h' < \sigma_H' < \sigma_v'$, (6) $\sigma_h' < \sigma_v' < \sigma_H'$, (7) $\sigma_v' = \sigma_h' < \sigma_H'$ lie between the lines of (1) and (2), (2) and (3), and (3) and (4) (Figure 4.10b). Each stress state is required for normal faulting, strike-slip faulting, and thrust faulting, respectively [*Anderson*, 1951]. Given that pore pressure is hydrostatic, the possible stress conditions are in the regions bounded by yield surface and the lines (1) and (4). When excess pore pressure is developed, the boundaries of lines (1) and (4) shift to the left by the amount of excess pore pressure shifts left with keeping the same yield surface.

If the stress state lies on the yield surface, the sample is normal consolidated. Normal consolidation can be achieved by not only the stress conditions in the past but also the present stress condition. In other word, greater burial depths in the past are not necessary to understand the consolidation state if large horizontal stress exists. In addition, to describe possible in-situ stress in p'-q space with critical state concept can give us insight on the deformation modes (brittle or ductile). Possible stress states of the sample 315-C0002B-63R-1 are all existed in cataclastic flow regime (Figure 4.10d), while those

of the samples 316-C0004D-48R-1 and 316-C0006F-8R-1 sit in both brittle faulting regime and cataclastic flow regime (Figures 4.10f and 4.10h). The stress conditions required for thrust faulting ((3) and (4)) are in the cataclasitc regime, while the stress conditions for normal faulting are in the brittle regime. It is consistent with general observations of deformation structures in core samples of both deformation bands and shear fractures in the frontal regions (Sites C0006 and C0007) [*Expedition 316 Scientists*, 2009b, 2009c]. The deformation bands mostly show reverse slip associated with horizontal layer-parallel contraction and the shear fractures show normal faulting. Furthermore, the formation of deformation bands followed by younger normal faults can be explained by the transition of stress states from the cataclastic flow regimes to the brittle faulting regime possibly due to stress rotation.

4.6.3. Relationships between hydraulic properties and stress states

The results of permeability of three experiments on the sample 316-6F-8R-1 are shown in Figure 4.11a. Although volumetric strain similarly decreases with the effective mean stress (Figure 4.8b), permeability evolution depends on the stress paths. Permeability decreases with log-linear relationship throughout the three stages of uniaxial strain loading. During the isotropic loading, permeability quickly decreases when the mean effective stress is less than approximately 5 MPa and stays almost constant at the mean effective stress up to 20 MPa and starts decreasing again down to 10^{-20} m^2 at effective mean stress of 50 MPa. Although there is some difference between

Figure 4.11. Evolution of permeability and porosity of the samples 316-C0006F-8R-1-a, 316-C0006F-8R-1-b, and 316-C0006F-8R-1-c. (a) Permeability as a function of effective mean stress. (b) Permeability - porosity relationship. (c) and (d) Contours of permeability and porosity in p-q space.

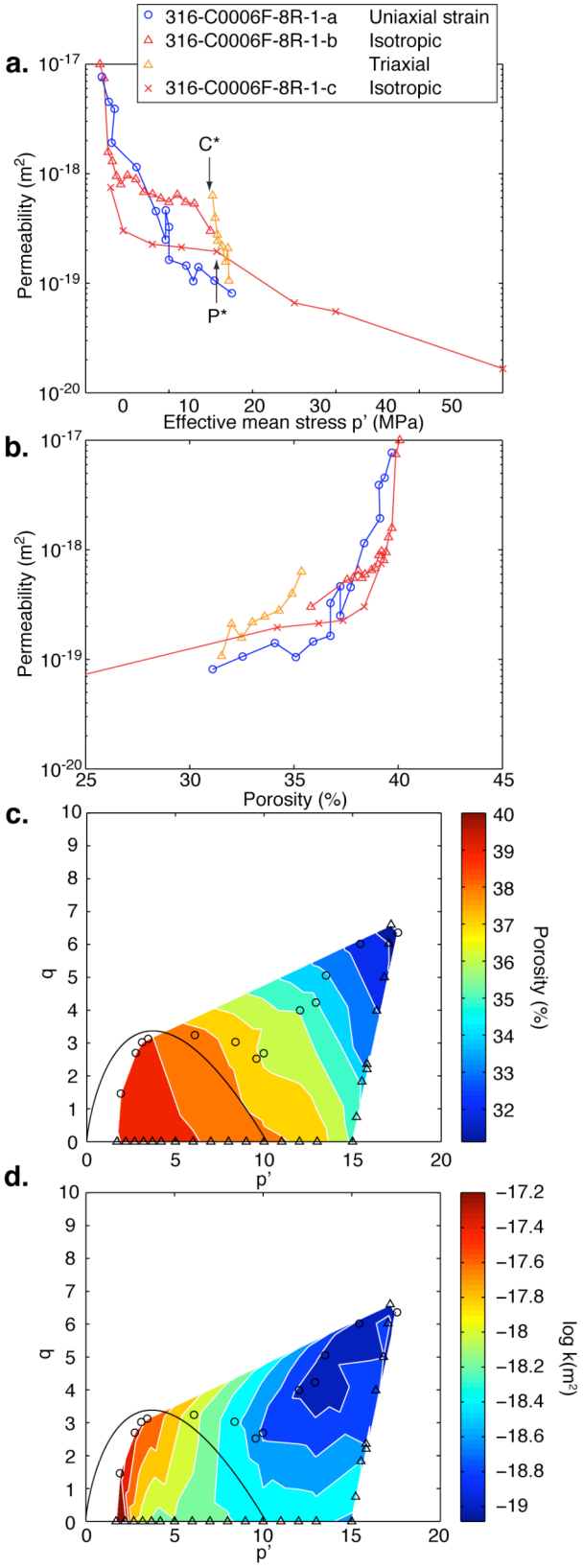
a.
316-C0006F-8R-1-a Uniaxial strain
316-C0006F-8R-1-b Isotropic
Triaxial
316-C0006F-8R-1-c Isotropic
C*
P*
Permeability (m²)
Effective mean stress p' (MPa)
b.
Permeability (m²)
Porosity (%)
c.
q
p'
Porosity (%)
d.
q
p'
log k(m²)

one-end and two-end pulse decay measurements, permeability evolution with the mean effective stress is very similar. The greatest reduction in permeability is observed in triaxial loading. The observations imply that cementation can be broken easier when differential stress is applied. In other word, larger effective mean stress is required to break cementation in isotropic stress conditions.

There are two trends in porosity-permeability relationship (Figure 4.11b). First, permeability quickly decreases with small changes in porosity and then porosity decreases with slow change in permeability. It is less obvious, but the effect of stress path can be seen as different slope. It is unknown if permeability-porosity relationship converge with greater strain such that the permeability-porosity relation for all load paths follow the isotropic case at higher stresses, as has been suggested from previous studies on porous sandstones that show the porosity-permeability relationship is independent of differential stress [*Zhu and Wong*, 1997] and permeability anisotropy diminishes at strain of ~ 10% [*Zhu et al.*, 2002].

On the basis of the experiment results, permeability and porosity are contoured in p'-q space (Figures 4.11c and 4.11d). Porosity evolution depends on both effective mean stress and differential stress and is sub-parallel to the predicted Cam-Clay yield surface. On the other hand, permeability evolution seems more complicated. When the stress states are within the yield surface, permeability largely depends on the effective mean stress, but isotropic condition can keep permeability higher. After the sample yields, permeability evolution depends more on the differential stress than on the effective mean stress. The permeability evolution in relation to both effective mean stress and

differential stress does not correspond with that of siliciclastic and carbonate rocks [*Crawford and Yale*, 2002], but in all cases the yield surface well describes the transition of permeability evolution.

Zhu et al. [2007] specified the three stages for stress-induced permeability reduction in porous rocks. In the elastic regime or Stage I, permeability and porosity reduction are solely controlled by the effective mean stress. In Stage II, differential stress primarily controls permeability and porosity evolution, i.e., permeability drastically decreases with increasing differential stress. In Stage III, permeability and porosity reduction becomes gradual again due to the development of pervasive cataclastic flow. Note that these three stages do not necessarily correspond to the three stages of strength evolution for uniaxial strain loading described above. Our experimental results show similarities and differences with the findings of *Zhu et al.* [2007]. Stage II is identified as the shear-enhanced permeability reduction in uniaxial strain loading and triaxial loading, although permeability reduction in uniaxial strain loading is more gradual than that in triaxial loading. Also, the transition between Stage I and Stage II is obvious when isotropic loading is initially applied, but not so clear in uniaxial strain loading (Figures 4.7c, 4.7g, and 4.11a). This has not been observed in the previous studies [*Zhu et al.*, 2002; *Crawford and Yale*, 2002], in which all triaxial deformation tests follow isotropic loading. More experimental works are necessary to fully understand the permeability evolution in terms of stress states and stress paths.

4.7. Conclusions

1) Using different stress paths facilitates understanding the mechanical and hydraulic behavior of sediments recovered from the Nankai Trough subduction zone. Experimental results indicate that all samples tested in this study are overconsolidated. Possible reasons for overconsolidation is (1) cementation, which is observed in uniaxial strain loading, (2) the maximum burial depth greater than the current depth, and (3) large horizontal stress. Overconsolidation can induce brittle faulting as well as development of excess pore pressure. Consolidation states must be characterized to understand the deformation mechanism in accretionary prism subduction zones.

2) The stress paths during Pc reduction for the NanTroSEIZE samples can be considered as yield surfaces, which are best described by Cam-Clay model. Constructing the virgin yield surface of the samples based on the experiment results can better describe the consolidation status and possible in-situ stress magnitudes which are complicated in accretionary prisms. The in-situ stress magnitudes, and mechanical properties such as undrained shear strength, unconfined compressive strength, and frictional angle can be estimated from the yield surface combined with the Coulomb failure criteria, stress polygons, and the borehole breakout data.

3) During consolidation, porosity decreases with both effective mean stress and differential stress as yield surface expands. Permeability evolution depends on only effective mean stress within the virgin yield surface, while it depends more on differential

stress than on effective mean stress after the sample yield. Differential stress can decrease permeability faster, which is consistent with shear-enhanced permeability reduction. Greatest change in permeability with both effective pressure and changing porosity is seen in triaxial loading.

5. SUMMARY

Rotary-shear experiments are suitable for understanding frictional behavior at coseismic slip rates because large displacements (tens of meters) can be readily achieved. Significant analysis of mechanical data is required to interpret the results, because slip velocity and displacement vary with radius. We implemented thermal-, mechanical-, and fluid-flow-coupled FEM models and microstructure observations to better describe the evolution of coefficient of friction, temperature, and stress within the sample. Dynamic weakening occurs at slip rates greater than 0.3 m/s and is associated with significant frictional heating and two characteristic microstructures of a localized slip zone and a fluidized layer. Friction of gouge at coseismic slip rates is successfully described by a combination of temperature-dependent friction constitutive relations, in which friction coefficient is proportional to 1/T, and thermal pressurization of pore water. Further investigations of frictional behavior at intermediate and high slip velocities are required to fully establish rate-, state-, and temperature-dependent friction constitutive relations for seismic slip rates. More detailed microstructure analysis is also needed to understand the microprocesses during coseismic slip.

The evolution of porosity and permeability of sediments recovered from the Nankai Trough subduction zone is dependent on effective mean stress and differential stress. Porosity evolution is independent of stress path, and porosity decreases as the yield surface expands. Permeability evolution depends on the stress state, stress path, and the consolidation state. Experimental yielding of sediment during undrained Pc reduction test is well described by Cam-Clay model of soil mechanics. The in-situ stress

conditions and strength of sediment are better estimated from the predicted yield envelopes combined with stress polygons and borehole breakout data. All samples tested are overconsolidated, and there are three possible reasons for overconsolidation, 1) sediments are cemented, 2) sediments have been subjected to larger overburden stress than the present in-situ overburden stress, or 3) large horizontal stress conditions within accretionary prism can overconsolidate sediments. More experiments on sediments from the input sites which are located off the deformation front and microstructure study on both natural and experimentally-deformed samples are necessary to understand the cause of overconsolidation.

REFERENCES

Anderson, E.M. (1951), *The Dynamics of Faulting and Dyke Formation with Applications in Britain*, Oliver and Boyd, Edinburgh, Scotland, United Kingdom.

Beeler, N. M., T. E. Tullis, M. L. Blanpied, and J. D. Weeks (1996), Frictional behavior of large displacement experimental faults, *J. Geophys. Res.*, *101*, 8697 – 8715.

Beeler, N. M., T. E. Tullis, and D. L. Goldsby (2008), Constitutive relationships and physical basis of fault strength due to flash heating, *J. Geophys. Res.*, *113*, B01401, doi:10.1029/2007JB004988.

Blanpied, M. L., D. A. Lockner, and J. D. Byerlee (1995), Frictional slip of granite at hydrothermal conditions, *J. Geophys. Res.*, *100*, 13,045 – 13,064, doi:10.1029/95JB00862.

Bolton, A. J., A. J. Maltman, and M. B. Clennell (1998), The importance of overpressure timing and permeability evolution in fine-grained sediments undergoing shear, *J. Struc. Geol.*, *20*(8), 1013 – 1022.

Boullier, A.-M., E.-C. Yeh, S. Boutareaud, S.-R. Song, and C.-H. Tsai (2009), Microscale anatomy of the 1999 Chi-Chi earthquake fault zone, *Geochem. Geophys. Geosyst.*, *10*, Q03016, doi:10.1029/2008GC002252.

Boutareaud, S., D.-G. Calugaru, R. Han, O. Fabbri, K. Mizoguchi, A. Tsutusmi, and T. Shimamoto (2008), Clay-clast aggregates: A new textural evidence for seismic fault sliding?, *Geophys. Res. Lett.*, *35*, L05302, doi:10.1029/2007GL032554.

Boutareaud, S., A.-M. Boullier, M.. Andréani, D.-G. Calugaru, P. Beck, S.-R. Song, and T. Shimamoto (2010), Clay-clast aggregates: New textural evidence for seismic faulting, *J. Geophys. Res.*, *115*, B02408, doi:10.1029/2008JB006254.

Brace, W. F., J. B. Walsh, and W. T. Frangos (1968), Permeability of granite under high pressure, *J. Geophys. Res.*, *73*, 2225-2236.

Brantut, N., A. Schubnel, J.-N. Rouzaud, F. Brunet, and T. Shimamoto (2008), High-velocity frictional properties of a clay-bearing fault gouge and implications for earthquake mechanics, *J. Geophys. Res.*, *113*, B10401, doi:10.1029/2007JB005551.

Brodsky, E. E., and H. Kanamori (2001), Elastohydrodynamic lubrication of faults, *J. Geophys. Res.*, *106*, 16357 – 16374.

Brown, K. M., A. Kopf, M. B. Underwood, and J. L. Weinberger (2003), Compositional and fluid pressure controls on the state of stress on the Nankai subduction thrust: A weak plate boundary, *Earth Planet. Sci. Lett.*, *214*, 589 – 603.

Brune, J. N., S. Brown, and P. A. Johnson (1993), Rupture mechanism and interface separation in foam rubber models of earthquakes: A possible solution to the heat flow paradox and the paradox of large overthrusts, *Tectonophysics*, *218*, 59 – 67.

Bryant, W. R., W. Hottman, and P. Traband (1975), Permeability of unconsolidated and consolidated marine sediments, Gulf of Mexico, *Marine Geotechnology.*, *1*, 1 – 14.

Byrne, D. E., D. M. Davis, and L. R. Sykes (1988), Loci and maximum size of thrust earthquakes and the mechanics of the shallow region of subduction zones, *Tectonics*, *7*, 833 – 857.

Chester, F. M. (1988), The brittle-ductile transition in a deformation-mechanism map for halite, *Tectonophysics*, *154*, 125 – 136.

Chester, F. M. (1989), Dynamic recrystallization in semi-brittle faults, *J. Struc. Geol.*, *11*(7), 847 – 858.

Chester, F. M. (1994), Effects of temperature on friction: Constitutive equations and experiments with quartz gouge, *J. Geophys. Res.*, *99*(B4), 7247 – 7261.

Chester, F. M. (1995), A rheologic model for wet crust applied to strike-slip faults, *J. Geophys. Res.*, *100*(B7), 13,033 – 13,044.

Chester, F. M., and J. S. Chester (1998), Ultracataclasite structure and friction processes of the Punchbowl fault, San Andreas system, California, *Tectonophysics*, *295*, 199 – 221.

Chester, F. M., and N. G. Higgs (1992), Multimechanism friction constitutive model for ultrafine quartz gouge at hypocentral conditions, *J. Geophys. Res.*, *97*(B2), 1859 – 1870.

Chester, F. M., and J. M. Logan (1987), Composite planar fabric of gouge from the Punchbowl fault, California, *J. Struct. Geol.*, *9*, 621 – 634.

Chester, J. S., F. M. Chester, and A. K. Kronenberg (2005), Fracture surface energy of the Punchbowl fault, San Andreas system, *Nature*, *437*, 133 – 136, doi:10.1038/Nature03942.

Crawford, B. R., and D.P. Yale (2002), Constitutive modeling of deformation and permeability: Relationships between critical state and micromechanics, *SPE/ISRM Rock Mechanics Conference*, 78189, 1 – 10, doi10.2118/78189-MS.

Crawford, B. R., D. R. Faulkner, and E. H. Rutter (2008), Strength, porosity, and permeability development during hydrostatic and shear loading of synthetic quartz-clay fault gouge, *J. Geophys. Res.*, *113*, B03207, doi:10.1029/2006JB004634.

Davis, D., J. Suppe, and F.A. Dahlen (1983), Mechanics of fold-and-thrust belts and accretionary wedges, *J. Geophys. Res.*, *88*, B2, 1153 – 1172.

Dieterich, J. H. (1978), Time-dependent friction and the mechanics of stick-slip, *Pure Appl. Geophys.*, *116*, 790 – 806, doi:10.1007/BF00876539.

Dieterich, J. (1979), Modeling of rock friction: 1. Experimental results and constitutive equations, *J. Geophys. Res.*, *84*(B5), 2161 – 2168.

Dieterich, J. H. (1981), Constitutive properties of faults with simulated gouge, in *Mechanical Behavior of Crustal Rocks*, *Geophys. Monogr. Ser.*, vol. 24, edited by N. L. Carter et al., pp. 103 – 120, AGU, Washington, D. C.

Dieterich, J. H. (1992), Earthquake nucleation on faults with rate-dependent and state-dependent strength, *Tectonophysics*, *211*, 115 – 134.

Di Toro, G., D. L. Goldsby, and T. E. Tullis (2004), Friction falls towards zero in quartz rock as slip velocity approaches seismic rates, *Nature*, *427*, 436 – 439, doi:10.1038/Nature02249.

Di Toro, G., T. Hirose, S. Nielsen, G. Pennacchioni, and T. Shimamoto (2006), Natural and experimental evidence of melt lubrication of faults during earthquakes, *Science*, *311*, 647 – 649, doi:10.1126/Science.1121012.

Expedition 314 Scientists (2009), Expedition 314 method, in *Proc. IODP 314/315/316*, edited by M. Kinoshita, H. Tobin, J. Ashi, G. Kimura, S. Lallemant, E. J. Screaton, D. Curewitz, H. Masago, K. T. Moe, and Expedition 314/315/316 Scientists, Integrated Ocean Drilling Program Management International, Washington DC, doi:10.2204/iodp.proc.314315316.112.2009.

Expedition 315 Scientists (2009), Expedition 315 Site C0002, in *Proc. IODP 314/315/316*, edited by M. Kinoshita, H. Tobin, J. Ashi, G. Kimura, S. Lallemant, E. J. Screaton, D. Curewitz, H. Masago, K. T. Moe, and Expedition 314/315/316 Scientists, Integrated Ocean Drilling Program Management International, Washington DC, doi:10.2204/iodp.proc.314315316.124.2009.

Expedition 316 Scientists (2009a), Expedition 316 Site C0004, in *Proc. IODP 314/315/316*, edited by M. Kinoshita, H. Tobin, J. Ashi, G. Kimura, S. Lallemant, E. J. Screaton, D. Curewitz, H. Masago, K. T. Moe, and Expedition 314/315/316 Scientists, Integrated Ocean Drilling Program Management International, Washington DC, doi:10.2204/iodp.proc.314315316.133.2009.

Expedition 316 Scientists (2009b), Expedition 316 Site C0006, in *Proc. IODP 314/315/316*, edited by M. Kinoshita, H. Tobin, J. Ashi, G. Kimura, S. Lallemant, E.J. Screaton, D. Curewitz, H. Masago, K.T. Moe, and Expedition 314/315/316 Scientists,

Integrated Ocean Drilling Program Management International, Washington DC, doi:10.2204/iodp.proc.314315316.134.2009.

Expedition 316 Scientists (2009c), Expedition 316 Site C0007, in *Proc. IODP 314/315/316*, edited by M. Kinoshita, H. Tobin, J. Ashi, G. Kimura, S. Lallemant, E.J. Screaton, D. Curewitz, H. Masago, K.T. Moe, and Expedition 314/315/316 Scientists, Integrated Ocean Drilling Program Management International, Washington DC, doi:10.2204/iodp.proc.314315316.135.2009.

Faulkner, D. R., T. M. Mitchell, T. Hirose, and T. Shimamoto (2009), Stuck in the mud? Earthquake propagation through clay-rich fault zones, *EOS Trans. AGU*, 90(52), Fall Meet. Suppl., Abstract T21D-1860.

Gamage , K. and E. Screaton (2006), Characterization of excess pore pressures at the toe of the Nankai accretionary complex, Ocean Drilling Program sites 1173, 1174, and 808: Results of one-dimensional modeling, *J. Geophys. Res.*, *111*, B04103, doi:10.1029/2004JB003572.

Gangi, A. F. (1978), Variation of whole and fractured porous rock permeability with confining pressure, *Int. J. Rock Mech. Min. Sci.*, *15*, 249 – 257.

Goldsby, D. L., and T. E. Tullis (2002), Low frictional strength of quartz rocks at subseismic slip rates, *Geophys. Res. Lett.*, *29*(17), 1844, doi:10.1029/2002GL015240.

Han, R., T. Shimamoto, T. Hirose, J. -H. Ree, and J. Ando (2007), Ultralow friction of carbonate faults caused by thermal decomposition, *Science*, *316,* 878 – 881, doi:10.1126/Science.1139763.

Heard, H. C. (1963), Effect of large changes in strain rate in the experimental deformation of Yule Marble: *Journal of Geology*, *71*, 162 – 195.

Hirose, T., and T. Shimamoto (2005), Growth of a molten zone as a mechanism of slip weakening of simulated faults in gabbro during frictional melting, *J. Geophys. Res.*, *110*, B05202, doi:10.1029/2004JB003207.

Holtz, R. D., W. D. Kovacs (1981), *An Introduction to Geotechnical Engineering*, Prentice-Hall, Englewood Cliffs, NJ.

Hsieh, P. A., J. V. Tracy, C. E. Neuzil, J. D. Bredehoeft, and S. E. Siilliman (1981), A transient laboratory method for determining the hydraulic properties of 'Tight rocks' – I. Theroy, Int. *J. Rock Mech. Min. Sci. & Geomech. Abstr.*, *18*, 245 – 252.

Hubbert, M. K., and W. W. Rubey (1959), Role of fluid pressure in mechanics of overthrust faulting: 1. Mechanics of fluid-filled porous solids, and its application to overthrust faulting, *GSA Bull.*, *70*, 115 – 166.

Hyndman, R. D., and K. Wang (1993), Thermal constraints on the zone of major thrust earthquake failure: The Cascadia subduction zone, *J. Geophys. Res.*, *98*, 2039 – 2060.

Hyndman, R. D., K. Wang, and M. Yamano (1995), Thermal constraints on the seismogenic portion of the southwestern Japan subduction thrust, *J. Geophys. Res.*, *100*, 15373 – 15392.

Ikari, M. J., D. M. Saffer, and C. Marone (2009), Frictional and hydrologic properties of clay-rich fault gouge, *J. Geophys. Res.*, *114*, B05409, doi:10.1029/2008JB006089.

Jager, J. C., and N. G. W. Cook (1979), *Fundamentals of Rock Mechanics*, 3rd ed.,

Chapman and Hall, London.

Jones, M. (1994) Mechanical principles of sediment deformation, in *The Geological Deformation of Sediments*, edited by A. Maltman, pp. 37 – 71, Chapman & Hall, London.

Kanamori, H., and T. Heaton (2000), Microscopic and macroscopic physics of earthquakes, in *Geocomplexity and the Physics of Earthquakes*, *Geophys. Monogr.*, vol. 20, edited by J. Rundle et al., pp. 127 – 141, AGU, Washington, D. C.

Karig, D. E. (1990), Experimental and observational constraints on the mechanical behaviour in the toes of accretionary prisms, in *Deformation Mechanisms, Rheology and Tectonics*, *Geol. Soc. Spec. Publ. London*, 54, edited by R. J. Knipe and E. J. Rutter, pp. 383 – 393.

Karig, D. E. (1993), Reconsolidation tests and sonic velocity measurements of clay-rich sediments from the Nankai trough, in *Proc. ODP, Sci. Results*, 131, edited by I. Hill *et al.*, pp. 247 – 260, College Station, TX.

Kitajima, H., J. S. Chester, F. M. Chester, and T. Shimamoto (2006), Dynamic weakening at seismic slip rates demonstrated for fault-rocks from SAFOD core and Punchbowl fault, *EOS Trans. AGU*, *87*(52), Fall Meet. Suppl., Abstract S41D-04.

Kitajima, H., J. S. Chester, F. M. Chester, and T. Shimamoto (2007), Implications for dynamic weakening of faulting from friction experiments of fault-rocks from SAFOD core and Punchbowl fault at seismic slip rates, Earthscope National Meeting.

Kitajima, H., J. S. Chester, F. M. Chester, and T. Shimamoto (2010), High-speed friction of disaggregated ultracataclasite in rotary shear: Characterization of frictional heating, mechanical behavior, and microstructure evolution, *J. Geophys. Res.*, *115*, B08408, doi:10.1029/2009JB007038.

Koster van Groos, A. F., and S. Guggenheim (1986), Dehydration of K-exchanged montmorillonite at elevated temperatures and pressures, *Clays and Clay Minerals*, *34*, 281 – 286.

Kwon, O., A. K. Kronenberg, A. F. Gangi, B. Johnson, and B. E. Herbert (2004), Permeability of illite-bearing shale: 1. Anisotropy and effects of clay content and loading, *J. Geophys. Res.*, *109*, B10205, doi:10.1029/2004JB003052.

Lachenbruch, A. H. (1980), Frictional heating, fluid pressure, and the resistance to fault motion, *J. Geophys. Res.*, *85*, 6097 – 6122.

Ladd, C. C., and R. Foott (1974), New design prodecure for stability of soft clays, *Journal of Geotechnical Engineering Division*, ASCE, *100*, 763 – 786.

Lapusta, N., and J. R. Rice (2003), Nucleation and early seismic propagation of small and large events in a crustal earthquake model, *J. Geophys. Res.*, *108*(B4), 2205, doi:10.1029/2001JB000793.

Lee K. (1981), Consolidation with constant rate of deformation, *Géotechnique*, *31*, 215 – 229.

Lide, D. R. (Eds.) (2006), *CRC Handbook of Chemistry and Physics*, 87th ed., CRC press, Boca Raton.

Lockner, D. A., and Z. Reches (2009), Dynamic strength variation of laboratory faults at slip velocities up to 1m/s, *EOS Trans. AGU*, *90*(52), Fall Meet. Suppl., Abstract T41A-1987.

Logan, J. M., and K. A. Rauenzahn (1987), Frictional dependence of gouge mixtures of quartz and montmorillonite on velocity, composition and fabric, *Tectonophysics*, *144*, 87 – 108.

Logan, J. M., M. Friedman, N. G. Higgs, C. Dengo, and T. Shimamoto (1979), Experimental studies of simulated gouge and their application to studies of natural fault gouge, in *Analysis of Actual Faull Zones in Bedrock*, edited by R. C. Speed and R. V. Sharp, U.S. geol. Surv., Open-file Report 79-1239, pp. 276 – 304.

Logan, J. M., N. G. Higgs, and M. Friedman (1981), Laboratory studies on natural fault gouge from the U.S. Geological Survey Dry Lake Valley No. 1 Well, San Andreas fault zone, in *Mechanical Behavior of Crustal Rocks: The Handin Volume*, *Geophys. Monogr. Ser.*, vol. 24, edited by N. L. Carter et al., pp. 121 – 134, AGU, Washington, D. C.

Mair, K., and C. Marone (1999), Friction of simulated fault gouge for a wide range of velocities and normal stresses, *J. Geophys. Res.*, *104*(B12), 28899 – 28914.

Marone, C. (1998), Laboratory-derived friction laws and their application to seismic faulting, *Annu. Rev. Earth Planet. Sci.*, *26*, 643 – 696.

Marone C., and B. Kilgore (1993), Scaling of the critical distance for seismic faulting with shear strain in fault zones, *Nature*, *362*, 618 – 621.

Marone C., and C. H. Scholz (1988), The depth of seismic faulting and the upper transition from stable to unstable slip regimes, *Geophys. Res. Lett.*, *15*, 621 – 624.

Mase, C. W., and L. Smith (1987), Effects of frictional heating on the thermal, hydrologic, and mechanical response of a fault, *J. Geophys. Res.*, *92*, 6249 – 6272.

McLaren, K. G., and D. Tabor (1963), Visco-elastic properties and the friction of solids: Friction of polymers: Influence of speed and temperature, *Nature*, *197*, 856 – 858.

Miyazaki, S. and K. Heki (2001), Crustal velocity field of southwest Japan: Subduction and arc-arc collision. *J. Geophys. Res.*, *106*, 4305 – 4326.

Mizoguchi, K., T. Hirose, T. Shimamoto, and E. Fukuyama (2007), Reconstruction of seismic faulting by high-velocity friction experiments: An example of the 1995 Kobe earthquake, *Geophys. Res. Lett.*, *34*, L01308, doi:10.1029/2006GL027931.

Mizoguchi, K., T. Hirose, T. Shimamoto, and E. Fukuyama (2009), High-velocity frictional behavior and microstructure evolution of fault gouge obtained from Nojima fault, southwest Japan, *Tectonophysics*, *471*, 285 – 296, doi:10.1016/J.Tecto.2009.02.033.

Monzawa, N., and K. Otsuki (2003), Comminution and fluidization of granular fault materials: Implications for fault slip behavior, *Tectonophysics*, *367*, 127 – 143.

Moore, D. E., R. Summers, and J. D. Byerlee (1989), Sliding behavior and deformation textures of heated illite gouge, *J. Struct. Geol.*, *11*, 329 – 342.

Moore, G. F., Park, J.-O., Bangs, N. L., Gulick, S. P., Tobin, H. J., Nakamura, Y., Sato, S., Tsuji, T., Yoro, T., Tanaka, H., Uraki, S., Kido, Y., Sanada, Y., Kuramoto, S., and Taira, A. (2009), Structural and seismic stratigraphic framework of the NanTroSEIZE

Stage 1 transect, in *Proc. IODP 314/315/316*, edited by M. Kinoshita, H. Tobin, J. Ashi, G. Kimura, S. Lallemant, E. J. Screaton, D. Curewitz, H. Masago, K. T. Moe, and Expedition 314/315/316 Scientists, Integrated Ocean Drilling Program Management International, Washington DC, doi:10.2204/iodp.proc.314315316.102.2009.

Moore, J. C. (Ed.) (1986), *Structual Fabric in Deep Sea Drilling Project Cores from Forearcs*, The Geological Society of America Memoir 166, The Geological Society of America, Inc., Boulder, CO.

Moore, J. C., and D. Saffer (2001), Updip limit of the seismogenic zone beneath the accretionary prism of southwest Japan: An effect of diagenetic to low-grade metamorphic processes and increasing effective stress, *Geology*, *29*, 2, 183 – 186.

Moore, J. C., and P. Vrolijk (1992), Fluids in acretionary prisms, *Rev. Geophys.*, *30* (2), 113 – 135.

Morgan, J. K., and M. V. S. Ask (2004), Consolidation state and strength of underthrust sediments and evolution of the décollement at the Nankai accretionary margin: Results of uniaxial reconsolidation experiments, *J. Geophys. Res.*, *109*, B03102, doi:10.1029/2002JB002335.

Morgan, J. K., E. B. Sunderland, M. V. S. Ask (2007), Deformation and mechanical strength of sediments at the Nankai subduction zone: Implications for prism evolution and decollement initiation and propagation, in *The Seismogenic Zone of Subduction Thrust Faults*, edited by Dixon, T.H, and J.C. Moore, MARGINS

Theoretical and Experimental Earth Science Series, Columbia University Press, pp. 210 – 256, Columbia University Press, New York.

Morrow, C. A., D. E. Moore, and D. A. Lockner (2000), The effect of mineral bond strength and adsorbed water on fault gouge frictional strength, *Geophys. Res. Lett*, *27*, 815 – 818.

Neuzil, C. (1994), How permeable are clays and shales?, *Water Resour. Res.*, *30*(2), 145 – 150.

Neuzil, C. E., C. Cooley, S. E. Silliman, J. D. Bredehoeft, P.A. Hsieh (1981), A transient laboratory method for determining the hydraulic properties of 'Tight rocks' – II. Application, *Int. J. Rock Mech. Min. Sci. & Geomech. Abstr.*, *18*, 253 – 258.

Noda, H. (2008), Frictional constitutive law at intermediate slip rates accounting for flash heating and thermally activated slip process, *J. Geophys. Res.*, *113*, B09302, doi:10.1029/2007JB005406.

Noda, H., E. M. Dunham, and J. R. Rice (2009), Earthquake ruptures with thermal weakening and the operation of major faults at low overall stress levels, *J. Geophys. Res.*, *114*, B07302, doi:10.1029/2008JB006143.

Otsuki, K., N. Monzawa, and T. Nagase (2003), Fluidization and melting of fault gouge during seismic slip: Identification in the Nojima fault zone and implications for focal earthquake mechanisms, *J. Geophys. Res.*, *108*(B4), 2192, doi:10.1029/2001JB001711.

Rice, J. R. (1992), Fault stress states, pore pressure distributions, and the weakness of the San Andreas Fault, in *Fault Mechanics and Transport Properties in Rocks*, edited by B. Evans and T.-F. Wong, pp. 475 – 503, Academic, San Diego.

Rice, J. R. (1993), Spatio-temporal complexity of slip on a fault, *J. Geophys. Res.*, *98*(B6), 9885 – 9907.

Rice, J. R. (1999), Flash heating at asperity contacts and rate-dependent friction, *EOS Trans. AGU*, *80*, Fall Meet. Suppl., F681.

Rice, J. R. (2006), Heating and weakening of faults during earthquake slip, *J. Geophys. Res.*, *111*, B05311, doi:10.1029/2005JB004006.

Rice, J. R. and M. Cocco (2006), Seismic fault rheology and earthquake dynamics, in *Tectonic Faults: Agents of Change on a Dynamic Earth*, edited by M. R. Handy et al., pp. 99 – 137, The MIT Press, Cambridge.

Roscoe, K. H., A. N. Schofield, and M. A. Wroth (1958), On the yielding of soils, *Géotechnique*, *8*, 22 – 53.

Rutter, E. H., R. H. Maddock, S. H. Hall, and S. H. White (1986), Comparative microstructures of natural and experimentally produced clay-bearing fault gouges, *Pure Appl. Geophys.*, *124*, 3 – 30.

Saffer, D. M. (2003), Pore pressure development and progressive dewatering in underthrust sediments at the Costa Rican subduction margin: Comparison with northern Barbados and Nankai, *J. Geophys. Res.*, *108*(B5), 2261, doi:10,1029/2002JB001787.

Saffer, D., and B. Bekins (1998), Episodic fluid flow in the Nankai accretionary complex: Timescale, geochemistry, flow rates, and fluid budget, *J. Geophys. Res.*, *103*(B12), 30351 – 30370.

Saffer, D. M., and C. Marone (2003), Comparison of smectite- and illite-rich gouge frictional properties: Application to the updip limit of the seismogenic zone along subduction megathrusts, *Earth Planet. Sci. Lett.*, *215*, 219 – 235.

Sawai, M., T. Shimamoto, and T. Togo (2009), Nojima fault zone revisited: High-velocity friction experiments and BET surface-area measurements of fault rocks, *EOS Trans. AGU*, *90*(52), Fall Meet. Suppl., Abstract T12B-06.

Screaton, E. J., D. M. Saffer, P. Henry, S. Hunze, and Leg 190 Shipboeard Scientific Party (2002), Porosity loss within underthrust sediments of the Nankai accretionary complex: Implications for overpressures, *Geology*, *30*, 19 – 22.

Screaton, E. J., G. Kimura, D. Curewitz, and the Expedition 316 Scientists (2009), Expedition 316 Summary, in *Proc. IODP 314/315/316*, edited by M. Kinoshita, H. Tobin, J. Ashi, G. Kimura, S. Lallemant, E. J. Screaton, D. Curewitz, H. Masago, K. T. Moe, and Expedition 314/315/316 Scientists, Integrated Ocean Drilling Program Management International, Washington DC, doi:10.2204/iodp.proc.314315316.131.2009.

Seno, T., S. Stein, A. E. Gripp (1993), A model for the motion of the Philippine Sea plate consistent with NUVEL-1 and geological data, *J. Geophys. Res.*, *98*, 17941 – 17948.

Shimamoto, T. (1986), Transition between frictional slip and ductile flow for halite shear zones at room temperature, *Science*, *231*, 711 – 714.

Shimamoto, T., and T. Hirose (2005), Intermediate-velocity friction barrier and its implication for earthquake generation, *EOS Trans. AGU*, *86*(52), Fall Meet. Suppl., Abstract T13E-08.

Shimamoto, T., and A. Tsutsumi (1994), A new rotaty-shear high-speed frictional testing machine: Its basic design and scope of research, (in Japanese with English abstract), *Struct. Geol.*, *39*, 65 – 78.

Schön, J. H. (1996), *Physical Properties of Rocks: Fundamentals and Principles of Petrophysics*, Handbook of Geophysical Exploration 18, Pergamon, New York.

Sibson, R. H. (1973), Interactions between temperature and fluid pressure during earthquake faulting- A mechanism for partial or total stress relief, *Nature*, *243*, 66–68.

Sleep, N. H. (2010), Application of rate and state friction formalism and flash melting to thin permanent slip zones of major faults, *Geochem*. *Geophys*. *Geosyst*., *11*, Q05007, doi:10.1029/2009GC002997.

Sone, H., and T. Shimamoto (2009), Frictional resistance of faults during accelerating and decelerating earthquake slip, *Nature Geoscience*, *2*, 705 – 708, doi:10.1038/ngeo637.

Spray, J. G. (1993), Viscosity determinations of some frictionally generated silicate melts: Implications for fault zone rheology at high-dtrain tates, *J. Geophys. Res.*, *98*, 8053 – 8068.

Takahashi, M., K. Mizoguchi, K. Kitamura, and K. Masuda (2007), Effects of clay content on the frictional strength and fluid transport property of faults, *J. Geophys. Res.*, *112*, B08206, doi:10.1029/2006JB004678.

Tanikawa, W., M. Sakaguchi, O. Tadai, and T. Hirose (2010), Influence of fault slip rate on shear-induced permeability, *J. Geophys. Res., 115*, B07412, doi:10.1029/2009JB007013.

Tembe, S., V. Vajdova, P. Baud, W. Zhu, and T.-f. Wong (2006), A new methodology to delineate the compactive yield cap of two porous sandstones under undrained condition, *Mechanics of Materials*, *39*, 513 – 523.

Terzaghi, K., R. B. Peck, and G. Mesri (1996), *Soil Mechanics in Engineering Practice*, 3rd ed., John Wiley & Sons, Inc., NY.

Tobin H., M. Kinoshita, J. Ashi, S. Lallemant, G. Kimura, E. J. Screaton, K. T. Moe, H. Masago, D. Curewitz, and the Expedition 314/315/316 Scientists (2009a) NanTroSEIZE Stage 1 expeditions: Introduction and synthesis of key results, in *Proc. IODP 314/315/316*, edited by M. Kinoshita, H. Tobin, J. Ashi, G. Kimura, S. Lallemant, E. J. Screaton, D. Curewitz, H. Masago, K. T. Moe, and Expedition 314/315/316 Scientists, Integrated Ocean Drilling Program Management International, Washington DC, doi:10.2204/iodp.proc.314315316.101.2009.

Tobin H., M. Kinoshita, K. T. Moe, and the Expedition 314 Scientists (2009b) Expedition 314 summary, in *Proc. IODP 314/315/316*, edited by M. Kinoshita, H. Tobin, J. Ashi, G. Kimura, S. Lallemant, E. J. Screaton, D. Curewitz, H. Masago, K.

T. Moe, and Expedition 314/315/316 Scientists, Integrated Ocean Drilling Program Management International, Washington DC, doi:10.2204/iodp.proc.314315316.111.2009.

Togo, T., T. Shimamoto, S. Ma, X. Wen, T. Hirose, X. Lei (2009), High-velocity friction experiments on the Longmenshan fault gouge towards the understanding of dynamic rupture propagation of the 2008 Wenchuan Earthquake, *EOS Trans. AGU*, *90*(52), Fall Meet. Suppl., Abstract T11A-1774.

Tse, S. T., and J. R. Rice (1986), Crustal earthquake instability in relation to the depth variation of frictional slip properties, *J. Geophys. Res.*, *91*(B9), 9452–9472.

Tsutsumi, A., and T. Shimamoto (1997), High-velocity frictional properties of gabbro, *Geophys. Res. Lett.*, *24*, 699 – 702.

Turcotte, D. L. and Schubert, G. (2001), *Geodynamics*, 2nd ed., Cambridge Univ. Press, Cambridge.

Ujiie, K., A. Yamaguchi, G. Kimura, S. Toh (2007), Fluidizatian of granular material in a subduction thrust at seismogenic depths, *Earth Planet. Sci. Lett.*, *259*, 307 – 318.

Vrolijk, P. (1990), On the mechanical role of smectite in subduction zones, *Geology*, *18*, 703 – 707.

Wibberley, C. A. J. (2002), Hydraulic diffusivity of fault gouge zones and implications for thermal pressurization during seismic slip, *Earth Planets Space*, *54*, 1153 – 1171.

Wood, D. M. (1990), *Soil Behaviour and Critical State Soil Mechanics*, Cambridge University Press, Cambridge.

Zhang, M., M. Takeda, T. Esaki, M. Takahashi, and H. Endo (2001), Effect of confining pressure and anisotropy on water air permeabilities of rocks, (in Japanses with English Abstract), *Shigen-to-Sozai*, *117*, 941 – 946.

Zhu, W., and T.-F. Wong (1997), The transition from brittle faulting to cataclastic flow: Permeability evolution, *J. Geophys. Res.*, *102*, B2, 3027 – 3041.

Zhu, W., L. G. J. Montési, and T.-f. Wong (2002), Effects of stress on the anisotropic development of permeability during mechanical compaction of porous sandstones, in *Deformation Mechanisms, Rheology and Tectonics: Current Status and Future Perspectives*, *Special Publications*, 200, edited by S. de Meer et al., pp. 119 – 136, The Geological Society of London, London.

Zhu, W., L. G. J. Montési, and T.-f. Wong (2007), A probabilistic damage model of stress-induced permeability anisotropy during cataclastic flow, *J. Geophys. Res.*, *112*, B10207, doi:10.1029/2006JB004456.

Zoback, M. D., C. Barton, M. Brudy, D.Castillo, T. Finkbeiner, B. Grollimund, D. Moos, P. Peska, C. Ward, and D. Wiprut (2003), Determination of stress orientation and magnitude in deep wells, *Int. J. Rock Mech. Min. Sci. Geomech. Abstr.*, *40*, 1049 – 1076.

VITA

Name:	Hiroko Kitajima
Address:	3115 TAMU, Department of Geology & Geophysics, Texas A&M University, College Station, TX 77843-3115
Email Address:	kitaji@tamu.edu
Education:	B.S., Science, Kyoto University, Japan, 2004 Ph. D., Geology, Texas A&M University, 2010